Dissertation zur Erlangung des Doktorgrades
der Fakultät für Chemie und Pharmazie
der Ludwig-Maximilians-Universität München

Discovery of a novel nonfiring mode in sinoatrial node pacemaker cells

Konstantin Hennis

aus

München, Deutschland

2021

Erklärung

Diese Dissertation wurde im Sinne von § 7 der Promotionsordnung vom 28. November 2011 von Herrn Prof. Dr. Christian Wahl-Schott betreut.

Eidesstattliche Versicherung

Diese Dissertation wurde eigenständig und ohne unerlaubte Hilfe erarbeitet.

München, 06.12.2021 _____

Konstantin Hennis

Dissertation eingereicht am: 11.10.2021

1. Gutachter: Prof. Dr. med. Christian Wahl-Schott

2. Gutachter: Prof. Dr. rer. nat. Martin Biel

Mündliche Prüfung am: 02.12.2021

Table of Contents

1. Introduction

1.1 Hyperpolarization-activated cyclic nucleotide-gated (HCN) channels

Hyperpolarization-activated cyclic nucleotide-gated (HCN) channels are transmembrane proteins that are expressed mainly in the cardiovascular system and central nervous system (Biel et al., 2009). They represent a specific class of ion channels within the superfamily of pore-loop cation channels and are the molecular correlate of the mixed Na^+/K^+ current I_f, which is also termed I_h/I_q or simply referred to as "pacemaker current". The latter term derives from the important roles of HCN channels in controlling neuronal excitability and cardiac rhythmicity. The channels possess several unique properties which are based on special structural characteristics and thereby set these proteins apart from other voltage-gated ion channels (Figure 1).

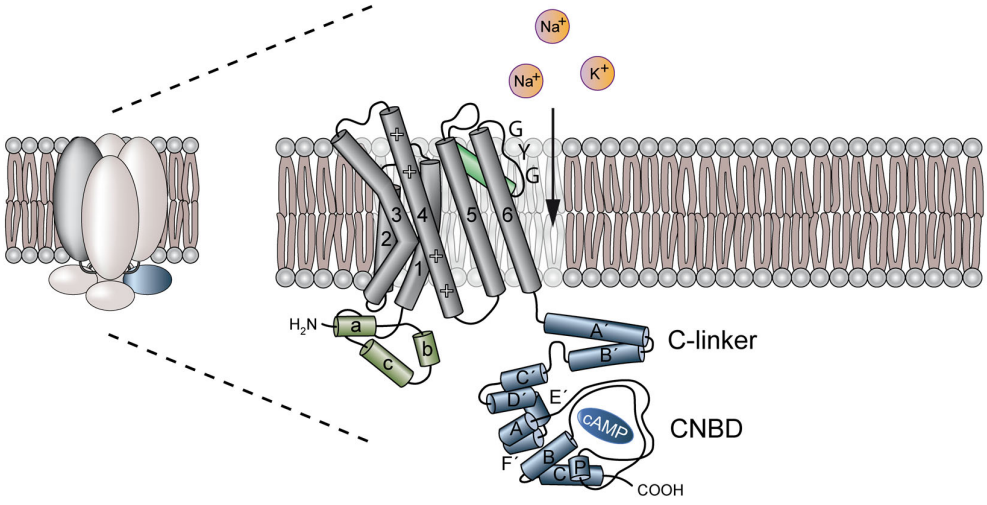

Figure 1. HCN channel structure. Model of an HCN channel protein embedded in a cell membrane. Each subunit is composed of six alpha-helical transmembrane segments (grey, numbered 1-6) and the intracellular N- and C-termini. The S1-S4 helices form the voltage-sensitive domain of the channel characterized by positively charged arginine and lysine residues at every third position of the S4 helix. The S5-S6 segments and the pore helix (green) make up the channel pore which contains the selectivity filter (GYG) in the pore loop between S5 and S6. The C-terminus (blue) contains the C-linker that consists of six alpha helices (A'-F') and connects the transmembrane segments to the cyclic nucleotide-

binding domain (CNBD). The CNBD is composed of three alpha helices (A-C) and a beta roll between helix A and B. Figure is adapted from (Hennis et al., 2021a).

The tetrameric HCN channel complex consists of four subunits, each composed of six alpha-helical transmembrane segments (S1-S6) and the intracellular N- and C-termini (Figure 1) (Biel et al., 2002). The S1-S4 segments form the voltage-sensitive domain of the channel, which is characterized by positively charged arginine and lysine residues at every third position of the S4 helix. The S5-S6 segments and the pore helix constitute the pore region of the channel, which contains the selectivity filter (GYG) within the ion-conducting pore loop between S5 and S6. The C-terminus comprises the C-linker and a cyclic nucleotide-binding domain (CNBD) (Zagotta et al., 2003). Moreover, it contains phosphorylation sites and binding domains for additional modulators including TRIP8b, an auxiliary subunit that is expressed in the brain and modulates HCN channel activity (Han et al., 2020). The most remarkable characteristic of HCN channels lies in activation by membrane hyperpolarization, which is in stark contrast to the depolarization-dependent activation of other voltage-gated ion channels. As a consequence, HCN channels are open and mediate a depolarizing inward current at membrane potentials negative to the channel's reversal potential, which is about -40 to -20 mV under physiological ion concentrations (Biel et al., 2009). This corresponds to, e.g., the range of diastolic membrane potentials in pacemaker cells of the cardiac conduction system. Another key feature is the modulation of HCN channel activity by cyclic nucleotides such as cyclic adenosine monophosphate (cAMP). It has been shown that the intracellular C-terminal CNBD exerts an inhibiting effect on the transmembrane region. Binding of cyclic nucleotides to the CNBD leads to a conformational change that is propagated through the C-linker and ultimately relieves inhibition of the transmembrane region, thereby facilitating channel opening (Wainger et al., 2001; Porro et al., 2019; Dai et al., 2021; Saponaro et al., 2021). In this way, changes in the intracellular cAMP concentration significantly regulate HCN channel activity within the physiological range of membrane potentials (DiFrancesco and Tortora, 1991). Together, the dual gating by hyperpolarization and binding of cyclic nucleotides forms the basis for the unique yet still incompletely understood physiological roles of HCN channels in the heart and brain.

In humans and mice, the HCN channel subfamily comprises four members termed HCN1-HCN4 (Ludwig et al., 1998; Mangoni and Nargeot, 2008; Biel et al., 2009). Profound differences between the four isoforms are found in their biophysical

properties including cAMP modulation and gating kinetics. HCN2 and HCN4 channels are highly sensitive to cAMP, while HCN1 activity is only weakly influenced, and HCN3, although containing an intact CNBD, is not affected by cAMP (Biel et al., 2002; Hennis et al., 2021a). With regard to the activation kinetics, HCN1 can be classified as the fastest channel followed by HCN2 and HCN3. HCN4 displays by far the slowest gating kinetics among the four subtypes (Biel et al., 2002).

1.2 Cardiac conduction system and sinoatrial node pacemaking

As mentioned above, HCN channels are expressed in the heart, where they appear to have the greatest impact in the cardiac conduction system (CCS, Figure 2A). The CCS consists of the sinoatrial node (SAN), atrioventricular node (AVN), bundle of His, bundle branches and Purkinje fibers. Spontaneously active pacemaker cells within the leading pacemaker region of the SAN generate the electrical activity that initiates each heartbeat. The electrical impulse is then conducted from the SAN to surrounding atrial cardiomyocytes, is rapidly propagated throughout the atria and towards the AVN, which is the only electrically conductive connection to the ventricles. After a conduction delay caused by the AVN, the impulse reaches the His-Purkinje system, from where it ultimately excites all ventricular cardiomyocytes. Although the other pacemaker centers in the CCS are in principle also capable of generating spontaneous activity, their intrinsic action potential frequencies are slower than that of the SAN and gradually decrease along the CCS, which makes the SAN the primary pacemaker to control heart rate (HR) under physiological conditions (Boyett, 2009; Hennis et al., 2021a).

The main characteristic feature of SAN pacemaker cells that enables spontaneous firing of action potentials is the slow diastolic depolarization (SDD, Figure 2B). This phase of the pacemaker cycle is initiated after action potential termination, when the membrane potential is most negative (maximum diastolic potential, MDP). During SDD, the pacemaker cells do not remain at a stable resting membrane potential, but instead slowly depolarize the membrane until a threshold potential is reached at which the upstroke of the next action potential is initiated. The rate of membrane depolarization during SDD critically controls the firing frequency of pacemaker cells and consequently determines the heart rate (Hennis et al., 2021b).

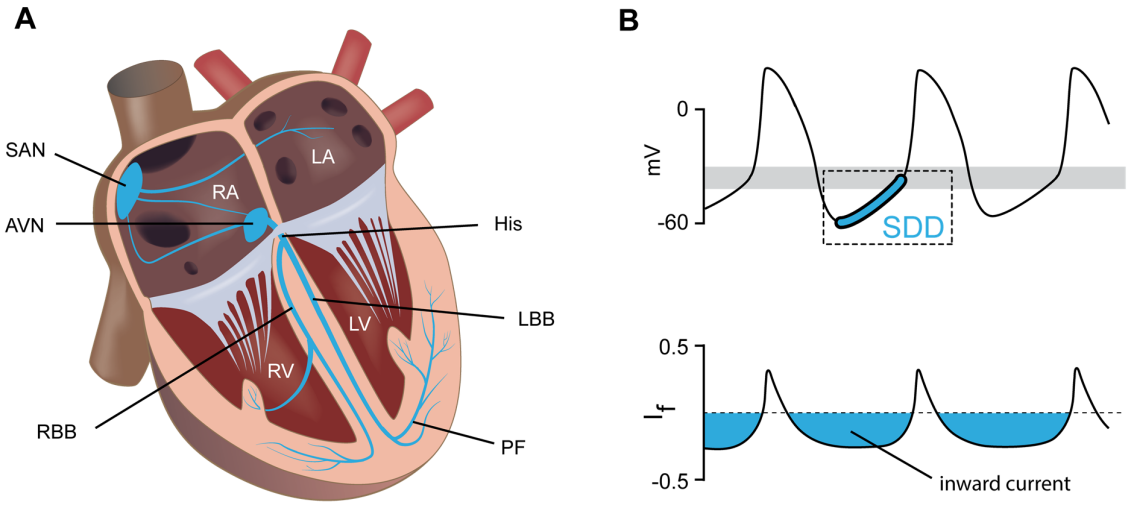

Figure 2. Cardiac conduction system and sinoatrial node automaticity. (A) Schematic illustration of the heart anatomy highlighting the components of the cardiac conduction system (CCS, blue). Abbreviations: SAN, sinoatrial node; AVN, atrioventricular node; His, bundle of His; RBB, right bundle branch; LBB, left bundle branch; PF, Purkinje fibers; RA, right atrium; LA, left atrium; RV, right ventricle; LV, left ventricle. **(B)** Upper panel, spontaneously generated action potentials of a SAN pacemaker cell. The slow diastolic depolarization (SDD, blue) is the main characteristic feature of SAN cells and is responsible for their cellular automaticity. Lower panel, time course of HCN channel-mediated I_f current in a SAN pacemaker cell (units in pA/pF). The channels are open throughout the pacemaker cycle and conduct a depolarizing inward current (blue) at hyperpolarized membrane potentials spanning the range of SDD. Figure is adapted from (Hennis et al., 2021a).

There are two main cellular mechanisms named *membrane clock* and *calcium clock* which are responsible and necessary for the generation of SDD (Lakatta et al., 2010). The term *membrane clock* summarizes all surface membrane currents resulting from the activity of ion channels and transporters that are localized in the cell membrane and contribute to depolarization during SDD. This ensemble includes ionic currents mediated by HCN channels, voltage-gated T-type ($Ca_V3.1$) and L-type Ca^{2+} channels ($Ca_V1.3$, $Ca_V1.2$) as well as voltage-gated Na^+ channels ($Na_V1.5$) (Hennis et al., 2021b). At the MDP, HCN channels are constitutively open and mediate the depolarizing inward current I_f, thereby initiating the early phase of SDD (Mangoni and Nargeot, 2008; Biel et al., 2009). This current depolarizes the membrane towards the threshold potential for activation of $Ca_V3.1$ and $Ca_V1.3$ channels. Subsequently, inward Ca^{2+} currents, together with I_f, lead to further membrane depolarization and cause additional opening of $Ca_V1.2$ channels. Finally, the inward Ca^{2+} current $I_{Ca,L}$ is mainly

responsible for generating the action potential upstroke and for coupling excitation to contraction via the calcium-induced calcium release mechanism (electromechanical coupling): Ryanodine receptor 2 (RyR2) is activated by Ca^{2+} ions entering the cytoplasm via $Ca_V1.2$ channels, which causes a global intracellular Ca^{2+} release from the sarcoplasmic reticulum (SR), thereby triggering myofibril contraction. To a minor extent, $I_{Na,1.5}$ is additionally involved in depolarization during late SDD and action potential upstroke. In the next step, the depolarized membrane potential causes inactivation of voltage-gated calcium and sodium currents, and initiates opening of delayed rectifier potassium channels. The outward currents $I_{K,r}$ and $I_{K,s}$ are mainly responsible for membrane repolarization and action potential termination, leading to return to the MDP (Mangoni and Nargeot, 2008; Mesirca et al., 2021).

In parallel to the membrane currents, intracellular localized Ca^{2+} releases from the SR occur periodically during the pacemaker cycle and are referred to as *calcium clock*. These local calcium releases (LCRs) result from spontaneous opening of ryanodine receptors (Vinogradova et al., 2004) and are coupled to membrane depolarization during late SDD via activation of the transmembrane sodium-calcium exchanger (NCX) (Bogdanov et al., 2001; Bogdanov et al., 2006). The SR Ca^{2+} load has a direct influence on the extent and timing of LCRs and is controlled by the activity of the sarco-/endoplasmic reticulum Ca^{2+} ATPase (SERCA) (Vinogradova et al., 2010), which in turn is regulated by phospholamban (Vinogradova et al., 2018). Taken together, a complex interplay of the *membrane clock* and *calcium clock* processes is required to form the coupled-clock system that is indispensable for the cardiac pacemaker process (Tsutsui et al., 2018).

1.3 Entrainment processes and chronotropic effect

As described above, the heartbeat is initiated by pacemaker cells within the CCS of the heart itself, and the resulting beating frequency under exclusion of external influences by humoral and neural factors is called intrinsic HR. In order to produce a stable and regular heart rhythm, the spontaneous activity of individual pacemaker cells must be synchronized to a common network rhythm in the SAN (Hennis et al., 2021a). The cellular prerequisite for this synchronization process is given by electrical coupling of pacemaker cells via gap junctions. Furthermore, there are intercellular connections to other cell types in the SAN network, i.e., macrophages (Hulsmans et al., 2017),

fibroblasts (Camelliti et al., 2004), and atrial cardiomyocytes (Verheijck et al., 2002), as well as synaptic contacts between pacemaker cells and nerve endings of the sympathetic nerve and vagus nerve (Pauza et al., 2014).

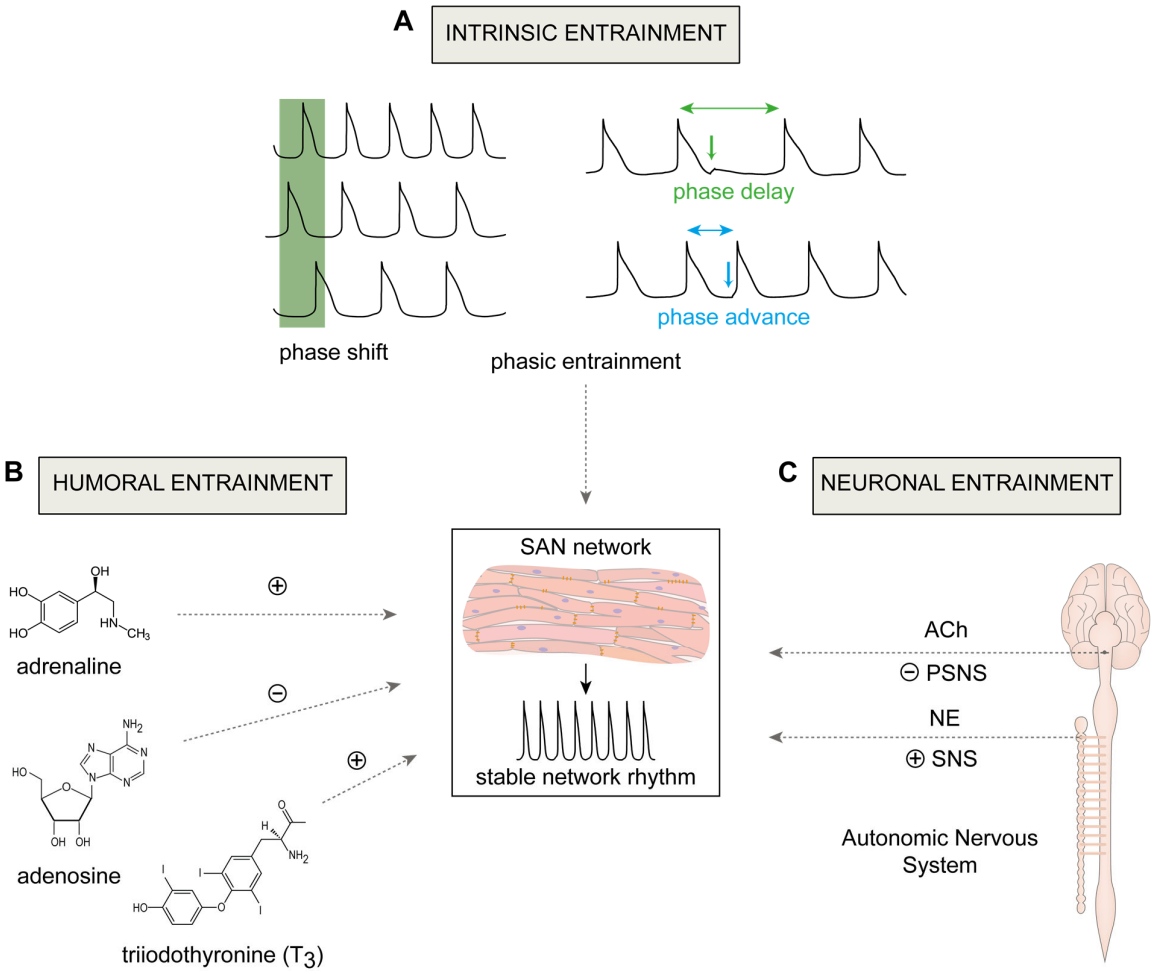

Figure 3. Entrainment processes in the sinoatrial node. (A) Intrinsic entrainment. Left panel, action potential traces of neighboring SAN pacemaker cells that occur at different time points due to slightly different firing rates (phase shift). Right panel, phasic entrainment process. Cells with faster firing rates receive premature depolarizing stimuli (indicated by green arrow) during early SDD, leading to prolongation of the cycle length (phase delay, green, upper panel). Cells with slower firing rates receive depolarizing stimulation during late SDD (blue arrow), leading to shortening of the cycle length (phase advance, blue, lower panel). Both mechanisms correct the cycle length and drive the cells back to network rhythm. **(B)** Humoral entrainment. Various locally released and circulating hormones, e.g., adrenaline, adenosine, or triiodothyronine (T3), affect the SAN network from the outside and are important modulators of heart rate due to stimulating (+) or inhibiting effects (−). **(C)** Neuronal entrainment. Both branches of the autonomic nervous system (ANS) innervate the SAN and adapt the

heart rate as a response to changes in physical or emotional activity. Activation of the parasympathetic nervous system (PSNS) leads to release of its neurotransmitter acetylcholine (ACh), thereby slowing down the SAN network rhythm and exerting destabilizing effects on the network. Activity of the sympathetic nervous system (SNS) has the opposite effects via release of the neurotransmitter norepinephrine (NE). Figure is adapted from (Hennis et al., 2021a).

Functional interactions of the pacemaker cells with each other and with the other cell types of the SAN network are important for electrical synchronization and can be classified into three main entrainment processes (Figure 3). The term intrinsic entrainment describes the synchronization process that takes place locally between the individual pacemaker cells of the SAN itself. A well-established process underlying intrinsic entrainment occurs between neighboring pacemaker cells that are generating spontaneous action potentials at slightly different firing rates (phase shift, Figure 3A, left panel) (Jalife, 1984). This process is called phasic entrainment (Figure 3A, right panel) and describes the observation that a single cell which fires faster than its surrounding cells will receive a depolarizing impulse from its neighboring cells during early SDD. As a result, the pacemaker cycle will be slightly prolonged, driving the fast-firing cell back to the network rhythm (phase delay). Conversely, a more slowly firing cell will be slightly depolarized during late SDD, which results in acceleration of the firing rate via shortening of the pacemaker cycle (phase advance). Together, this phasic entrainment process provides a negative feedback mechanism, which occurs at a beat-to-beat timescale and stabilizes the overall network rhythm of the SAN (Hennis et al., 2021a). In addition to intrinsic entrainment, there are different external influences which affect the SAN network from the outside and contribute to adjusting and changing the network rhythm. The term humoral entrainment describes the complex influence on SAN pacemaker activity by a variety of circulating hormones, e.g., catecholamines, adenosine, and thyroid hormones (Figure 3B) (MacDonald et al., 2020).

Furthermore, HR is regulated by the autonomic nervous system (ANS) via the neuronal entrainment process to adapt the cardiac output to changes in physical or emotional activity (Figure 3C). The ANS comprises the sympathetic nervous system (SNS) and the parasympathetic nervous system (PSNS). Both branches of the ANS innervate the SAN (Pauza et al., 2014) and regulate the firing rate of pacemaker cells by altering the slope of SDD−a process called chronotropic effect (Figure 4). Upon activation of the

SNS, norepinephrine is released from sympathetic nerve terminals and binds to G_s protein-coupled beta-adrenergic receptors located on the surface of SAN pacemaker cells. Subsequently, adenylyl cyclases inside the cell are activated, which leads to an increase in the cytosolic concentration of the second messenger cAMP (Behar et al., 2016). Reversely, upon PSNS activation, acetylcholine is released from vagal nerve terminals and activates G_i protein-coupled muscarinic receptors. This causes inhibition of adenylyl cyclases, resulting in decreased intracellular cAMP levels. The changes in the cAMP concentration eventually affect the rate of SDD and thereby accelerate or decelerate the heart rate, which is referred to as positive or negative chronotropic effect, respectively. Since many of the proteins involved in the *membrane clock* and *calcium clock* mechanisms are known to be direct or indirect cAMP targets, there are various potential candidates to mediate the chronotropic effect on the subcellular level, and the main contributor to HR regulation in SAN pacemaker cells has not yet been clearly identified (Hennis et al., 2021b).

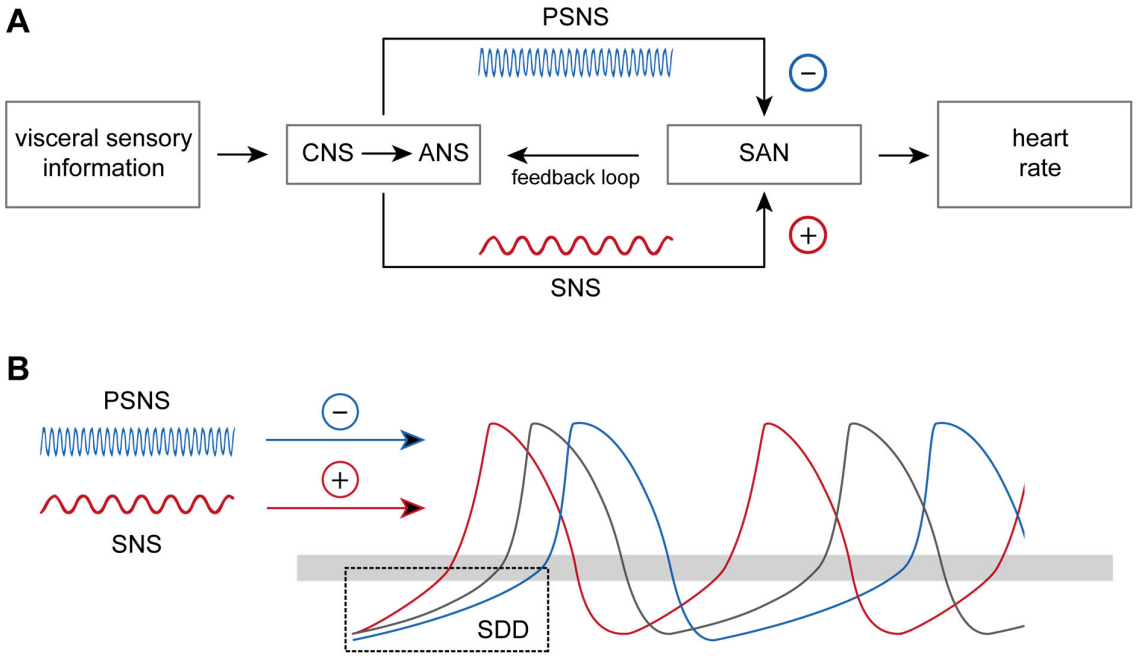

Figure 4. Heart rate is regulated by the autonomic nervous system. (A) Schematic illustration of the chronotropic effect. Visceral sensory information from the periphery reaches the central nervous system (CNS), which in turn regulates activity of the autonomic nervous system (ANS). The ANS consists of the sympathetic nervous system (SNS, red) and the parasympathetic nervous system (PSNS, blue), with both branches innervating the sinoatrial node (SAN) and adjusting the heart rate (HR). **(B)** Spontaneous

action potentials of SAN pacemaker cells (grey). Input from the PSNS (blue) reduces the slope SDD, which increases the time to reach the threshold for the next action potential. Consequently, the firing rate of pacemaker cells decreases which slows down HR (negative chronotropic effect). In contrast, activation of the SNS (red) leads to a steeper slope of SDD, which increases the firing rate of pacemaker cells and accelerates HR (positive chronotropic effect).

1.4 cAMP-dependent regulation of HCN4

Three of the HCN channel subtypes, i.e., HCN4, HCN1 and HCN2, are expressed in the SAN (Stieber et al., 2003; Marionneau et al., 2005; Herrmann et al., 2011; Fenske et al., 2013; Li et al., 2015), with HCN4 representing the main isoform. HCN4 is present throughout the entire SAN region, where it mediates approximately 75% of the I_f current (Herrmann et al., 2007; Nof et al., 2010). As outlined above, HCN4 channel activity is substantially controlled by intracellular cAMP concentrations, and is therefore directly regulated by the ANS. Moreover, the channels are open throughout the pacemaker cycle (Peters et al., 2021) and conduct a depolarizing inward current at hyperpolarized membrane potentials spanning the range of SDD (Figure 2B). Theoretically, these properties would be ideal to significantly alter the rate of SDD in response to changes in the intracellular cAMP concentration. Consequently, it has been postulated for more than 30 years that HCN4 is the main ANS target to primarily mediate the chronotropic effect in SAN pacemaker cells (Brown et al., 1979; DiFrancesco et al., 1986; DiFrancesco and Tortora, 1991; DiFrancesco, 1993). However, this classical theory was mainly derived from experiments on single pacemaker cells isolated from the rabbit SAN, and until now there is no direct experimental evidence that validates this concept *in vivo*. Rather, with the emerging possibility of creating and studying genetically modified animal models, it became more and more clear that this classical concept may not be completely correct. While some results obtained in embryonic mouse hearts support this hypothesis (Stieber et al., 2003; Harzheim et al., 2008), other studies using mutant adult mice strongly argue against an important role of cAMP-dependent regulation (CDR) of HCN4 in regulating HR (Herrmann et al., 2007; Alig et al., 2009; Baruscotti et al., 2011; Mesirca et al., 2014; Kozasa et al., 2018; Fenske et al., 2020). These controversies underline that up to now the functional significance of HCN4 CDR for the SAN pacemaker process is highly disputed, and that there is a clear scientific need to experimentally review the classical concept put forward by Dario DiFrancesco and colleagues.

1.5 HCN4FEA mouse model

For that purpose, the novel cAMP-insensitive HCN4FEA knock-in mouse model was generated in the laboratory of Professor Martin Biel (Scharr, 2011; Fenske et al., 2020). HCN4FEA animals carry three point mutations in the *Hcn4* gene, resulting in global expression of mutant HCN4 channels that contain two amino acid exchanges in the CNBD (R669E, T670A) and one in the C-linker (Y527F) (Figure 5). The R669E and T670A mutations prevent formation of three hydrogen bonds that have been shown to be crucial for the cAMP binding reaction (Figure 5C) (Zagotta et al., 2003). Furthermore, R669 normally exerts the strongest electrostatic interaction with cAMP by formation of an ionic bond with the cyclized phosphate (Zhou and Siegelbaum, 2007). In the HCN4FEA mutant channel, this salt bridge is predicted to be absent due to the R669E mutation. Together, the R669E and T670A mutations completely disrupt binding of cAMP to the CNBD, resulting in loss of cAMP-dependent regulation (CDR) of the channel.

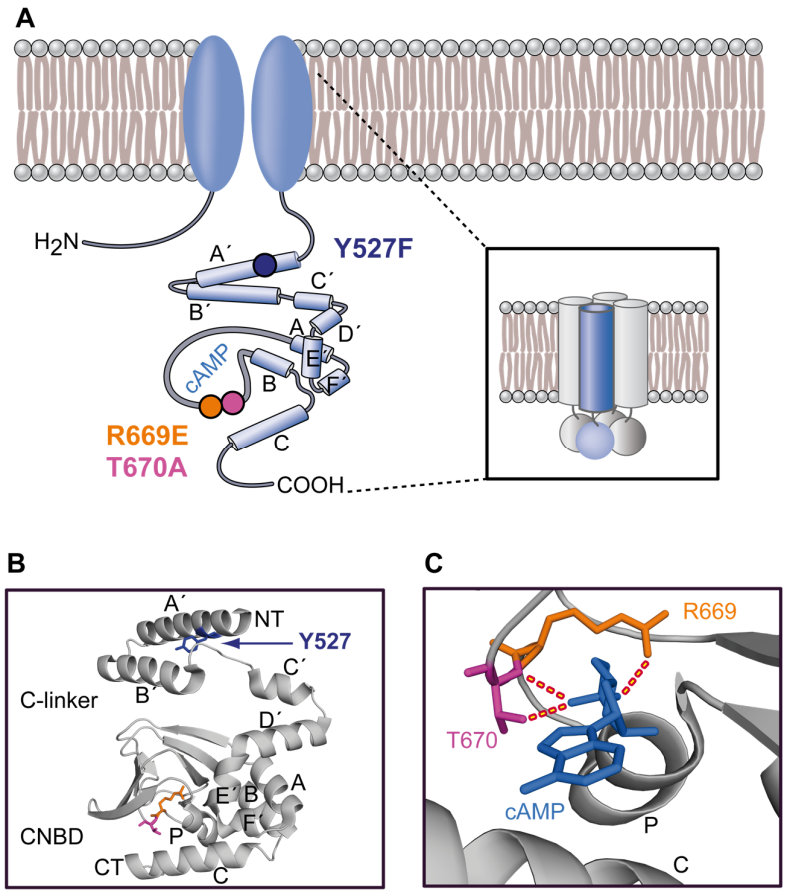

Figure 5. Structure of HCN4 and localization of amino acids targeted in cAMP-insensitive HCN4FEA channels. (A) Schematic illustration showing a single subunit and HCN4 channel tetramer (inset). The structure of the C-terminus is particularly highlighted and the amino acids mutated in HCN4FEA channels are indicated. **(B)** Molecular visualization of the HCN4 C-terminus containing the C-linker and cyclic nucleotide-binding domain (CNBD). **(C)** Molecular model of cAMP bound to the CNBD. Three hydrogen bonds (red) between cAMP and the R669 and T670 residues are depicted that are crucial for the cAMP binding reaction. Formation of these hydrogen bonds and an ionic bond between cAMP and R669 are prevented in HCN4FEA channels, resulting in disruption of cAMP binding and loss of cAMP-dependent regulation (CDR) of the channel. Figure is adapted from (Fenske et al., 2020).

However, it has previously been demonstrated that cAMP-dependent activation of HCN4 is fundamentally required for the physiological function of the channel, and that mice with globally abolished HCN4 CDR die during embryonic development (Harzheim et al., 2008). This is possibly caused by the fact that in the complete absence of cAMP, or in mutant channels that cannot be activated by cAMP, the activation thresholds of the channel are more negative than the MDP of pacemaker cells, which essentially causes a functional knock-out of HCN4 (Herrmann et al., 2007; Fenske et al., 2020). To avoid such experimental limitations, the Y527F mutation in the C-linker was introduced. This mutation simulates channel activation by basal cAMP levels, reflected by a constant shift of the activation curve towards more positive potentials and moderate acceleration of gating kinetics, altogether preventing embryonic lethality.

Electrophysiological measurements of mutant HCN4FEA channels expressed in HEK293 cells show that the half-maximal activation voltage ($V_{0.5}$) as well as activation and deactivation time constants are unaffected by cAMP and lie in between the respective values obtained for wild-type (WT) channels in the absence and presence of saturating intracellular cAMP concentrations (Figure 6 A-C). I_f measurements in native SAN pacemaker cells isolated from WT and HCN4FEA mice revealed no differences in current densities and confirmed the results from heterologously expressed HCN4FEA channels (Figure 6 D-F). This indicates normal expression and membrane trafficking of HCN4FEA channels, and demonstrates that apart from loss of CDR, the mutant channels are fully functional.

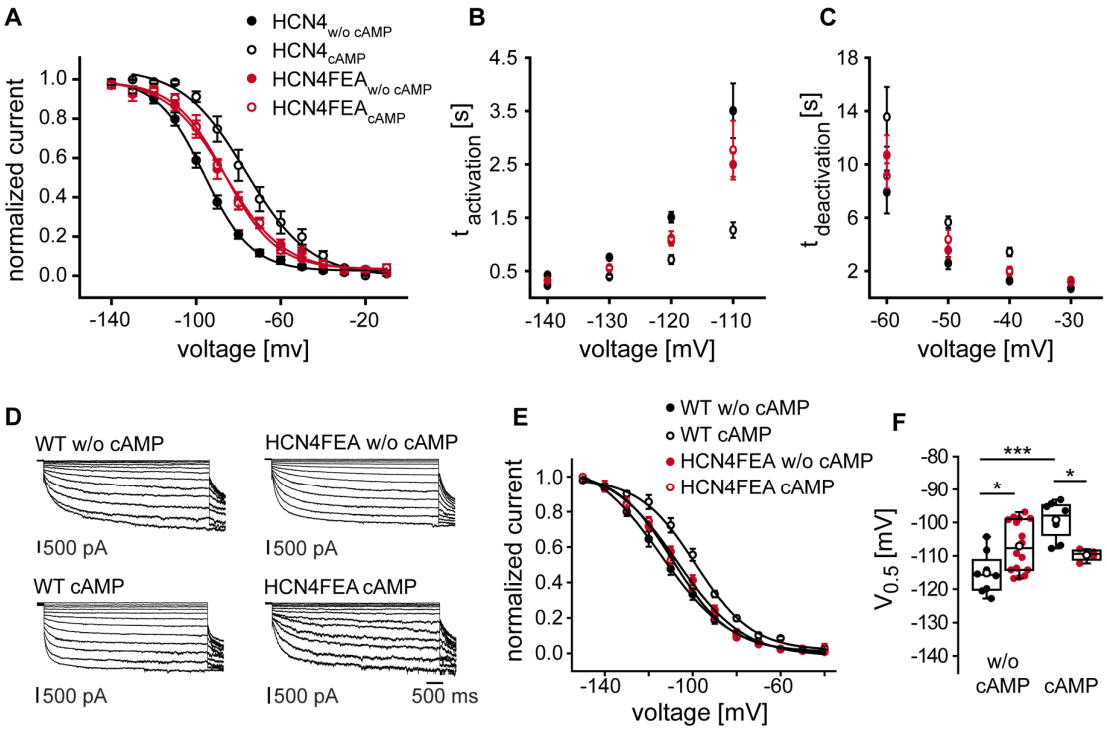

Figure 6. Characterization of HCN4FEA-mediated I_f current in HEK293 and isolated SAN cells. (A) Activation curves of wild-type HCN4 and mutant HCN4FEA channels heterologously expressed in HEK293 cells in the absence and presence of 100 µM cAMP in the intracellular solution. **(B)** Activation time constants of HCN4 and HCN4FEA-mediated currents measured at test potentials ranging from −140 mV to −110 mV. **(C)** Deactivation time constants of currents measured at test potentials ranging from −60 mV to −30 mV. **(D)** Representative I_f recordings obtained in native SAN cells isolated from WT and HCN4FEA mice. **(E)** Activation curves measured in native SAN cells. **(F)** Half-maximal activation voltage ($V_{0.5}$) determined from activation curves as shown in (E). Note that in both HEK293 and isolated SAN cells, the activation curve of wild-type HCN4 is shifted to more depolarised potentials by cAMP, whereas HCN4FEA activation curves and kinetic parameters are not affected. $V_{0.5}$ values, activation time constants and deactivation time constants from HCN4FEA mutant channels lie in between values determined from WT channels with and without cAMP. Figure is adapted from (Fenske et al., 2020).

Moreover, neither structural nor morphological abnormalities such as fibrosis or myofibrillar disarray are observed in hearts of HCN4FEA mice, and the expression levels of the different HCN channel isoforms as well as those of other major depolarizing and repolarizing ion channels are not affected by the mutations (Fenske et al., 2020). Taken together, these characteristics make the HCN4FEA mouse an ideal animal model to selectively study the physiological significance of HCN4 CDR for the cardiac pacemaker process and HR regulation by the ANS.

2. Aim of the study

The current textbook knowledge of the functional significance of cAMP-dependent regulation of I_f for the cardiac pacemaker process goes back to the early 1980s and was derived mainly from experiments on isolated rabbit SAN cells (Brown et al., 1979; DiFrancesco et al., 1986; DiFrancesco and Tortora, 1991; DiFrancesco, 1993). This classical theory assumes that the chronotropic effect, i.e., the acceleration or deceleration of heart rate following sympathetic or vagal activity, respectively, is mediated by an increase or decrease in I_f as a response to binding or dissociation of cAMP to/from the CNBD of the channel passing I_f (i.e., HCN4). However, until now there is no direct experimental evidence validating this concept *in vivo* and the exact subcellular signal transduction pathway in SAN pacemaker cells underlying the chronotropic effect remains controversially discussed (Hennis et al., 2021b).

The present study is set out to re-evaluate the role of HCN4 CDR in the SAN using the recently established HCN4FEA mouse line (Fenske et al., 2020). The main advantage of this mouse model is that three amino acid exchanges in the HCN4 C-terminus are sufficient to completely disrupt binding of cAMP to the CNBD, while at the same time embryonic lethality is prevented. In all other aspects, the resulting mutant channels are fully functional which allows direct and specific investigation of the cAMP-dependent regulation (CDR) of the channel as well as analyses of its functional effects from the single cell level to the intact living animal.

In this study, a sophisticated electrophysiological technique was employed to investigate the firing characteristics of isolated SAN pacemaker cells from WT and HCN4FEA mice. Furthermore, a confocal imaging approach was established that enables measurement of intracellular calcium transients in intact tissues, and the technique was used to uncover network effects of the HCN4FEA mutation in whole-mount SAN preparations. Finally, a right heart catheter-based electrophysiological study was carried out and significantly refined to determine the functional impact of HCN4 CDR on the cardiac conduction system *in vivo*.

3. Materials and Methods

Ethics statement. All animal experiments in this study were carried out in accordance with German laws on animal experimentation and were approved by the local authorities (Regierung von Oberbayern). Effort was taken to keep the number of animals at a minimum.

3.1 Experimental animals

The novel HCN4FEA knock-in mouse line ($Hcn4^{tm3(Y527F;R669E;T670A)Biel}$) was used for experiments in this study (Fenske et al., 2020). The mice were generated on a mixed 129SvJ−C57-Bl6/N background, and wild-type (WT) mice with the same genetic background were used as control group. HCN4FEA mice carry three point mutations in the *Hcn4* gene, leading to two amino acid exchanges in the CNBD (R669E, T670A) and one in the C-linker region (Y527F). The R669E and T670A mutations completely disrupt binding of cAMP to the CNBD, while the Y527F mutation mimics basal cAMP-dependent activation of the channel, thereby preventing embryonic lethality. This results in global expression of mutant HCN4FEA channels, characterized by loss of cAMP-dependent regulation (CDR) but otherwise unaltered functional channel properties. All animals were kept in conventional Euro-Standard type III cages under SPF conditions in a 12 h dark-light cycle with access to food and water *ad libitum*.

3.2 Genotyping of HCN4FEA mice

Genomic DNA isolation. The genotype of the experimental animals (WT or HCN4FEA) was determined by polymerase chain reaction (PCR) combined with agarose gel electrophoresis. To this end, genomic DNA was isolated from ear biopsies as follows. Tissue samples were incubated in 600 µl NaOH (50 mM) at 95°C and 450 rpm for 10 minutes in a dry block heater. Subsequently, 50 µl Tris-HCl (pH = 8.0) were added for pH neutralization and the samples were centrifuged for 6 minutes at 13 000 rpm. The supernatants were used as genomic DNA samples for PCR analysis.

Polymerase chain reaction (PCR). PCR was carried out using a ProFlex PCR System Cycler (Applied Biosystems) to amplify DNA fragments with GoTaq polymerase (Promega Corporation) in combination with the following two custom-designed primers (ordered from Eurofins Genomics Germany GmbH):

Primer 1 (HCN4FEA_for): 5'-CTC AAG GTC TCA GCT GAG G-3'

Primer 2 (HCN4FEA_rev): 5'-GTA ATG TAA GCA CAC GGT ACC-3'

The following reaction mix was prepared for PCR:

Substance	**Volume [µl]**
DNA sample	2
Primer 1 (10 µM)	2
Primer 2 (10 µM)	2
dNTPs	0.5
5x Green Buffer	5
Taq Polymerase (GoTaq)	0.125
H_2O (highly purified)	11.375

The following PCR cycle protocol was used for amplification of DNA fragments:

Step	**Temperature**	**Duration**	**Number of repeats**
Initial Denaturation	95°C	2 min	1x
Denaturation	95°C	30 s	40 cycles
Annealing	59°C	30 s	
Elongation	72°C	40 s	
Final Elongation	72°C	5 min	1x

Gel electrophoresis. For separation and detection of amplified DNA fragments, gel electrophoresis was carried out using 2% agarose gels. For this purpose, agarose (Genaxxon Bioscience) was dissolved in Tris/Borate/EDTA buffer (TBE buffer), and peqGREEN (VWR International GmbH) was added to enable visualization of DNA fragments under UV light. The solidified gels were placed in electrophoresis chambers and the pockets were filled with 13 µl amplified DNA samples. Electrophoresis was carried out by applying a voltage of 120 – 180 V. Subsequently, DNA bands were visualized using a GelDoc 2000 molecular imager (Bio-Rad Laboratories, Inc.) and fragment size was determined in comparison to a 1 kb GeneRuler Plus ladder (Thermo Fisher Scientific). WT and HCN4FEA bands were identified at 350 bp and 450 bp, respectively.

3.3 Electrophysiology of mouse SAN pacemaker cells

For all patch-clamp experiments, 8 to 10-week-old male WT and HCN4FEA mice were used for single cell isolation from the SAN. For preparation of buffers and solutions, deionized and highly purified water (Milli-Q Water Purification System, Merck Millipore) was used.

3.3.1 Poly-L-lysine-coated coverslips for patch-clamp experiments

To enable proper cell attachment for patch-clamp experiments, microscopic cover glasses (VWR International GmbH) with a 12 mm diameter were coated with poly-L-lysine (PLL). To this end, PLL-hydrobromide (Sigma-Aldrich, Merck KGaA) was dissolved in deionized and highly purified H_2O and diluted to obtain a concentration of 0.1 mg/ml. Under sterile conditions in a laminar flow cabinet (cell culture workbench), the coverslips were washed in 80% ethanol for 1 hour and were then transferred one-by-one into 24-well plates. After all residual ethanol had fully evaporated, the coverslips were covered with a single droplet of PLL solution passed through a 0.2 µm sterile filter. Subsequently, the coverslips were incubated at 37°C for one hour, followed by two washing steps with sterile PBS. Afterwards, the 24-well plates were left open to dry overnight on the sterile workbench.

3.3.2 Buffers and solutions for electrophysiology

The following solutions were prepared for isolation and patch-clamp experiments of single SAN pacemaker cells:

Tyrode III

Molarity	Substance
140 mM	NaCl
5.4 mM	KCl
1.0 mM	$MgCl_2$
1.8 mM	$CaCl_2$
5.0 mM	HEPES
5.5 mM	D-glucose

pH = 7.4 (NaOH)

Tyrode $_{low}$

Molarity	Substance
140 mM	NaCl
5.4 mM	KCl
0.5 mM	$MgCl_2$
0.2 mM	$CaCl_2$
1.2 mM	KH_2PO_4
50 mM	Taurine
5.0 mM	HEPES
5.5 mM	D-glucose

pH = 6.9 (NaOH)

Kraftbrühe (KB)

Molarity	Substance
80 mM	L-glutamic acid
25 mM	KCl
3.0 mM	$MgCl_2$
10 mM	KH_2PO_4
20 mM	Taurine
10 mM	HEPES
0.5 mM	EGTA
10 mM	D-glucose

pH = 7.4 (KOH)

Pipette solution

Molarity	Substance
90 mM	K-aspartate
10 mM	NaCl
2.0 mM	$MgCl_2$
2.0 mM	$CaCl_2$
5.0 mM	EGTA
2.0 mM	Na_2-ATP
0.1 mM	Na_2-GTP
5.0 mM	Creatine phosphate

pH = 7.2 (KOH)

To perform measurements in the perforated-patch configuration, amphotericin B (EDQM, France) was dissolved in DMSO by sonication at room temperature for 10

minutes using a Fisherbrand FB15049 Water Bath Sonicator (Thermo Fisher Scientific). Subsequently, the amphotericin B solution was added to the pipette solution to reach a final concentration of 200 µg/ml.

3.3.3 Isolation of single pacemaker cells from the mouse SAN

For isolation of single pacemaker cells from the SAN, isoflurane anesthesia was induced by transferring the mouse into an induction chamber, followed by slowly raising the concentration of isoflurane mixed with carbogen (95% O_2 + 5% CO_2) from 1% to 4%. Once deep inhalation anesthesia was achieved, the mouse was removed from the chamber and immediately sacrificed by cervical dislocation. After confirmation of death by decapitation, the beating heart was quickly excised and transferred into warm Tyrode III solution (37°C). The SAN region was isolated as described previously (Fenske et al., 2016), and 2-3 incisions were made in order to optimize the subsequent enzymatic digestion procedure by increasing the tissue surface. The excised SAN was then transferred into warm Tyrode $_{low}$ solution (37°C), and BSA (1.0 mg/ml, Merck KGaA, Germany), elastase (18.4 U/ml, KGaA, Germany), collagenase B (0.3 U/ml, Roche Diagnostics, Germany), and protease (1.8 U/ml, KGaA, Germany) were added. Enzymatic digestion was carried out in a dry block heater (Thermomixer Compact, Eppendorf AG) at 37°C and 450 rpm for 26-28 minutes, depending on the size of the tissue. The SAN was then centrifuged at 4°C and 200 g for 2 minutes, and the supernatant containing the digestion mixture was discarded. Subsequently, the same centrifugation protocol was applied in order to wash the tissue twice with Tyrode $_{low}$ and twice with Kraftbrühe (KB) medium. The SAN tissue was then stored for 3-4 hours in 350 µl KB medium at 4°C. Afterwards, the tissue was adapted to room temperature for 15 minutes, and SAN cells were mechanically separated by pipetting the tissue 4-8 times with modified pipette tips. Poly-L-lysine-coated coverslips were placed in a custom-made, vapor-saturated incubation chamber, and 50 µl of cell suspension were added to each coverslip. For proper cell attachment, sedimentation was allowed for 15 minutes. Subsequently, the coverslips were transferred one-by-one to the temperature-controlling recording chamber of the patch-clamp setup and the cells were re-adapted to a physiological extracellular Ca^{2+} concentration by applying the following Ca^{2+} reintroduction pipetting scheme:

Calcium reintroduction

Tyrode III (37°C)	+ 5 µl	wait 1-2 minutes
	+ 11 µl	wait 1-2 minutes
	+ 25 µl	wait 4 minutes
	+ 43 µl	wait 4 minutes
	+ 43 µl	wait 2 minutes

Afterwards, continuous superfusion with Tyrode III solution was initiated and temperature was tightly controlled at 32°C. Only spontaneously beating SAN cells with elongated shape were used for patch-clamp recordings.

3.3.4 Long-term action potential recordings in perforated-patch variation

Long-term action potential recordings were carried out in current clamp mode using the perforated-patch variation of the patch-clamp technique. A HEKA EPC10 USB double patch-clamp amplifier (HEKA Elektronik, Germany) in combination with Patchmaster v2x90.2 software was used for all patch-clamp experiments. Data analysis was carried out using Fitmaster v2x90.2, Clampfit 10.5.2.6, and Origin Pro 2018G software. Recording electrodes were fabricated with a DMZ-Universal Microelectrode Puller (Zeitz-Instruments Vertriebs GmbH, Germany) and filled with intracellular solution containing the pore-forming compound amphotericin B. Following gigaseal formation, electrical access to the intracellular compartment was established within 3-5 minutes, as judged by serial resistance values of < 50 MΩ. Subsequently, the amplifier was set to current clamp mode and gap-free action potential recordings of up to one hour were carried out (minimum duration 5 minutes). These recordings were retrospectively analyzed to determine the spontaneous firing pattern. Cells were categorized into the “firing and nonfiring mode” group when continuous periods of at least 10 seconds without spontaneous action potential firing were identified, during which the membrane potential remained at hyperpolarized values (average MDP ± 10 mV). Cells that did not display such periods were categorized as “firing mode only”. In case of an episodic firing pattern (firing and nonfiring mode), the difference in membrane potential between beginning and termination of nonfiring episodes was

determined (ΔVm). To quantify the occurrence of nonfiring, the percentage of cells assigned to the different activity modes was calculated. In addition, the total duration of nonfiring episodes was evaluated and reported as the percentage of time spent in the nonfiring mode. The shortest nonfiring period included in the statistics was 3.5 seconds. For pharmacological investigation, the cells were first measured under baseline conditions, followed by superfusion with Tyrode III containing isoproterenol (Merck KGaA, Germany) or carbachol (Merck KGaA, Germany). Direct superfusion of the cells was carried out at 32°C using a 6 Lines Multi Solution In-Line Heater (Multichannel Systems, Warner Instruments). To test the response to increased intracellular cAMP levels by mimicking sympathetic activity, isoproterenol (100 nM) was washed in and action potentials were recorded for 5 further minutes. In separate experiments, increasing doses of the cholinergic agonist carbachol (10 nM, 100 nM, 1000 nM) were successively applied to the cells (2.5 minutes each) in order to simulate vagal activity and to investigate the firing characteristics under decreasing intracellular cAMP levels. Only cells that resumed to rhythmic firing after washout of carbachol were included in the analysis (data not shown). To study the effect of TAT-TRIP8b$_{nano}$ (Saponaro et al., 2018) (specific amino acid sequence ordered from Caslo ApS, Denmark), the cells were incubated with the peptide (10 µM in Tyrode III) for 30 minutes at room temperature prior to patch-clamp experiments. Subsequently, action potential recordings were performed in peptide-free Tyrode III solution within a time frame of 60 minutes.

3.4 Confocal calcium imaging in whole-mount SAN preparations

Confocal calcium imaging in whole-mount SAN preparations was performed using an upright Leica TCS SP8 confocal laser scanning microscope equipped with a 20x water immersion objective. Leica LasX software was employed for data acquisition and data analysis. An optically pumped semiconductor laser (OPSL) was used to expose the tissue to an excitation wavelength of 488 nm at 8 kHz resonant scanning speed. The acquisition mode was set to “xyt” and calcium transients were recorded over time at 12 bit hardware resolution by detecting emission with a HyD hybrid detector at wavelengths above 505 nm.

3.4.1 Buffers and solutions for calcium imaging

The following solutions were prepared for confocal calcium imaging experiments:

Tyrode's solution

Molarity	Substance
128.2 mM	NaCl
4.7 mM	KCl
1.19 mM	NaH_2PO_4
1.05 mM	$MgCl_2$
1.3 mM	$CaCl_2$
20.0 mM	$NaHCO_3$
11.1 mM	Glucose

pH = 7.35 (O_2/CO_2)

Fluo-4-AM loading buffer (20 µM)

Fluo-4-AM (Biomol #ABP-20551) was dissolved in DMSO to obtain a 2 mM stock solution. In addition, a stock solution of Pluronic F-127 (Sigma-Aldrich, Merck KGaA) was prepared (13% in DMSO). The loading buffer was prepared on the day of the experiment by thoroughly mixing 10 µl Fluo-4-AM stock solution and 10 µl Pluronic F-127 stock solution (1:1) in a brown 1.5 ml Eppendorf tube, followed by adding 980 µl Tyrode's solution. Subsequently, the loading buffer was kept at 4°C in the dark until use.

Excitation-contraction-uncoupler blebbistatin:

Blebbistatin (Cayman Chemicals #13186) was dissolved in DMSO to obtain a 10 mg/ml stock solution and stored in 20 µl aliquots at -20°C in the dark. Immediately before use, 20 µl blebbistatin stock solution were diluted with 980 µl Tyrode's solution (37°C) in a 1 ml syringe to reach a final concentration of 0.2 mg/ml. The solution was kept warm in order to avoid precipitation of blebbistatin in the syringe.

3.4.2 Whole-mount tissue preparation and staining procedure

Whole-mount SAN preparations of 12-week-old female WT and HCN4FEA mice were dissected as described in the Results section (chapter 4.2.1). In brief, mice were sacrificed by cervical dislocation under deep inhalation anesthesia (see chapter 3.3.3). Beating hearts were quickly excised and transferred to a custom-made, perfusable, sylgard-coated petri dish filled with warm, oxygenated Tyrode's solution (37°C). After aortic cannulation, the hearts were retrogradely perfused with Tyrode's solution to clear the intracardiac compartments from any residual blood. Subsequently, the larger part of the ventricles was cut off and after removing the aortic cannula, the position of the tissue was fixed to the sylgard surface with a pin. Next, a single straight cut was made through the right ventricular wall, tricuspid valve and right atrial wall towards the superior vena cava. A second incision at the right atrial appendage was made to expose the endocardial surface of the right atrium. Remaining ventricular tissue and adjacent blood vessels were removed and the tissue preparation was carefully spanned as flat as possible and fixed to the sylgard surface with pins.

Afterwards, the Tyrode's solution was removed, and 1 ml Fluo-4-AM loading buffer (20 µM) was directly pipetted onto the SAN region, followed by incubation at room temperature in the dark for 45 minutes. Finally, the loading buffer was washed out and the excitation-contraction-uncoupler blebbistatin (0.2 mg/ml) was applied directly to the SAN region in order to prevent the tissue explants from beating and to minimize motion artifacts in the recordings. Subsequently, the Fluo-4-loaded whole-mount SAN preparations were transferred to the confocal microscope and temperature was tightly controlled at 27°C with a heating plate and incubation chamber. After 5-10 minutes of equilibration, confocal calcium imaging recordings were taken by covering the entire SAN region in 440 μm^2 frames. During the whole time course of the experiment, the tissue preparations were continuously superfused with warm, oxygenated Tyrode's solution (27°C).

After measurements under baseline conditions, TAT-TRIP8b$_{nano}$ (15 µM in Tyrode's solution) was added to the WT whole-mount preparations. Incubation with the peptide was allowed for 30 minutes, followed by repeated recordings in peptide-free Tyrode's solution.

3.4.3 Software settings for data acquisition

The following software settings were chosen in Leica LasX software to obtain confocal recordings of intracellular calcium transients in whole-mount SAN preparations:

Acquisition mode: xyt

Resonant scanner: ON

Speed: 8000Hz

Bidirectional X: ON

Objective: HCX APO L 20x/1.00 WATER

Zoom factor: 1.25

Pixel size: ~400 nm

Pinhole: 1.0 AU

Frame average: 1

Line average: 1

Minimize: ON

Duration: 5-10 sec

Format: 1024x1024

Hardware bit depth/resolution: 12 bit

Excitation beam splitter: DD 488/552

Laser: OPSL 488

Laser line: 488 nm, 0.5 - 3.0%

Detector: HyD1, 505 nm – 790 nm, Gain 20%

3.5 *In vivo* intracardiac electrophysiological study (EPS)

In vivo intracardiac electrophysiological study (EPS) was carried out as described previously (Hennis et al., 2021c). The acquisition system was composed of a portable EP Tracer device (EP-TRACER 38, Cardiotek GmbH The Netherlands) in combination with an octapolar CIB'ER MOUSE™ electrophysiology catheter (NuMED, Inc.; REF: CM001). In addition, a stereomicroscope (Stemi 2000, Carl Zeiss Microscopy Deutschland GmbH), isoflurane vaporizer (Völker Medizintechnik GmbH), anesthetic mask with gas scavenger (Lab Active Scavenger, GROPPLER Medizintechnik), and homeothermic blanket system with flexible probe (Harvard Apparatus, #507221F) were used. Furthermore, a custom-made puncture cannula was prepared by bending the tip of a 24G needle by approximately 90° with a needle holder or blunt forceps. Lidocaine solution for local anesthesia of the surgical area was prepared on the day of the experiment by dissolving lidocaine hydrochloride (Sigma-Aldrich, Merck KGaA) in sterile saline (0.9% sodium chloride, B. Braun Melsungen AG, #235 0720) under aseptic conditions.

3.5.1 Preparatory measures and surgery

For *in vivo* EPS, 8 to 12-week-old male WT and HCN4FEA mice were used. To prepare mice for surgery, anesthesia was induced by transferring the mouse into an induction chamber, followed by slowly raising the concentration of isoflurane mixed with carbogen (95% O_2 + 5% CO_2) from 1% to 4%. Subsequently, the mouse was placed in a supine position on the warm heating mat under the stereomicroscope and the isoflurane inhalation mask was immediately placed over the nose. Anesthesia was maintained with an isoflurane concentration between 1.5% and 2.0 %. The eyes were completely covered with eye ointment and the front paws were fixed to the heating mat with surgical tape. To expose the surgical area, the fur was removed from skin with depilatory cream. The rectal temperature probe was inserted approximately 0.5 cm deep into the rectum to monitor and control body temperature. Needle electrodes (13x0.40 mm, 0.5x27G, 1.0m (40"), Xi'an Friendship Medical Electronics Co.) were inserted subcutaneously into the limbs to record surface ECG according to Einthoven (lead I, II, and III). The fourth needle electrode served as signal grounding. Lidocaine (0.5 mg/ml in sterile saline) was injected subcutaneously across the surgical area to

ensure proper local anesthesia. Sufficient depth of anesthesia was verified by absence of toe pinch reflex before commencing surgery.

The surgical procedure was performed as described in the Results section (see chapter 4.3.1). Briefly, a straight skin incision was made from below the chin towards the transversal pectoral muscles. The right external jugular vein was exposed and isolated by bluntly dissecting surrounding muscle and fat tissue with angled forceps. Two surgical sutures were drawn underneath the vessel and a surgical knot was formed to the most proximal part of the jugular vein. The vein was tied off as close to the head as possible and a loose knot in the second suture was formed. The suture end was gently pulled towards the tail with a needle holder to stretch the jugular vein, resulting in temporary obstruction of blood flow. A custom-made, angled cannula was used to puncture the vein at the most proximal part. The electrophysiology catheter was carefully inserted into the opening underneath the cannula tip and pushed forwards, while its position was monitored by observing the electrical signals on the computer screen. Once the electrodes were located in the right atrium and ventricle, as judged by the intracardiac ECG signals, the second suture was secured to keep the catheter fixed in its position.

3.5.2 Intracardiac stimulation of the right atrium and ventricle

After verification of correct catheter placement in the right heart (see chapter 4.3.1), the stimulus amplitude and duration required for successful atrial and ventricular pacing were determined. To this end, a train of eight stimuli with 0.5 ms duration and 0.5 mA amplitude was applied via the atrial or ventricular electrodes, respectively. If one or several stimuli failed to elicit an atrial or ventricular response, the amplitude was gradually increased in 0.5 mA steps towards 1.5 mA. In case the intensity of stimulation was still insufficient, the duration was additionally increased in 0.5 ms steps towards 1.5 ms. Subsequently, programmed electrical stimulation was carried out as described in the Results section (see chapter 4.3.2) in order to determine specific cardiac electrophysiological parameters including sinus node recovery time (SNRT), sinoatrial conduction time (SACT), AV-nodal conduction properties, Wenckebach periodicity, atrial and ventricular refractory periods, and vulnerability to atrial and ventricular arrhythmia (Hennis et al., 2021c).

3.6 Quantification and statistical analysis

Data analysis and figure preparation were carried out with Origin Pro 2018G (OriginLab Corporation, USA) and Adobe Illustrator CS3 software (Adobe Systems, Inc.). Boxplots in all figures show the median line, perc 25/75, and min/max value. Open symbols represent the mean value. Statistical analysis was performed using Origin Pro 2018G software. Data are given as mean ± standard error of the mean (SEM). For all statistical tests, $p < 0.05$ was considered significant (***$p < 0.001$, **$p < 0.005$, *$p < 0.05$, ns = not statistically significant $p > 0.05$). Data were tested for normal distribution and differences between two groups were analyzed by student's unpaired two-sample t-test. In case of multiple comparisons, the p values were adjusted using Holm-Bonferroni correction. In cases where normal distribution was not confirmed, the nonparametric Mann-Whitney-U-test was used to determine differences between two groups. Experiments with two different variables were analyzed with two-way ANOVA, followed by Sidakholm post-hoc test. For EPS parameters that were determined at different coupling intervals, data were analyzed by two-way ANOVA for repeated measures, based on the general linear model (GLM).

4. Results

In the present study, a set of experimental techniques including single-cell electrophysiology, confocal calcium imaging in excised tissue preparations, and *in vivo* cardiac electrophysiology was employed to investigate the role of cAMP-dependent regulation of HCN4 channels in cardiac pacemaker function. For this purpose, the novel cAMP-insensitive HCN4FEA mouse model (Fenske et al., 2020) was used for investigation at the single-cell level, in whole-mount SAN preparations, and in intact living animals.

4.1 Long-term action potential recordings of isolated SAN pacemaker cells.

The perforated patch configuration of the patch-clamp technique was used in current-clamp mode to obtain long-term action potential recordings of spontaneously beating SAN pacemaker cells isolated from WT and HCN4FEA mice. The main advantage of this approach is that it enables electrical access to the intracellular compartment without rupture of the membrane patch. Thereby, the integrity of the cytoplasm is widely preserved, because dilution of the intracellular milieu and washout of cellular factors including cAMP are mostly prevented. This results in considerably more physiological conditions compared to the conventional whole-cell configuration, and allows for ultra-stable recordings of up to one hour. To this end, the pore-forming compound amphotericin B was added to the pipette solution, providing electrical access to the cell within 3-5 minutes after gigaseal formation (Figure 7).

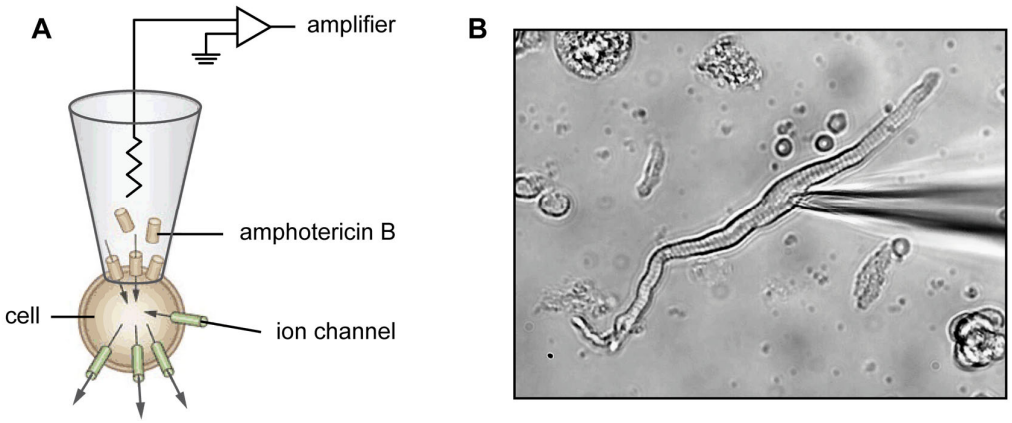

Figure 7. Perforated patch-clamp technique in isolated SAN pacemaker cells. (A) Schematic illustration of the perforated patch-clamp technique. Electrical access to the intracellular compartment is established by the pore-forming compound amphotericin B, making rupture of the membrane patch obsolete. **(B)** Image of an isolated SAN pacemaker cell during patch-clamp recording. Figure is adapted from (Ashcroft and Rorsman, 2013).

4.1.1 Action potential recordings under baseline conditions

First, long-term action potential recordings were performed under baseline conditions. These experiments revealed that cells from both WT and HCN4FEA mice fired spontaneous pacemaker potentials at a stable and regular rhythm (Figure 8 A-B). No differences were observed in the mean firing rate, slope of SDD, and maximum diastolic potential (Figure 8 C-E). Moreover, the averaged action potential shape was similar in WT and HCN4FEA cells (Figure 8F), indicating that the sum of all major depolarizing and repolarizing currents contributing to the pacemaker potential is not significantly altered in HCN4FEA mice. The results suggest that CDR of HCN4 does not play an important role during baseline firing of SAN pacemaker cells.

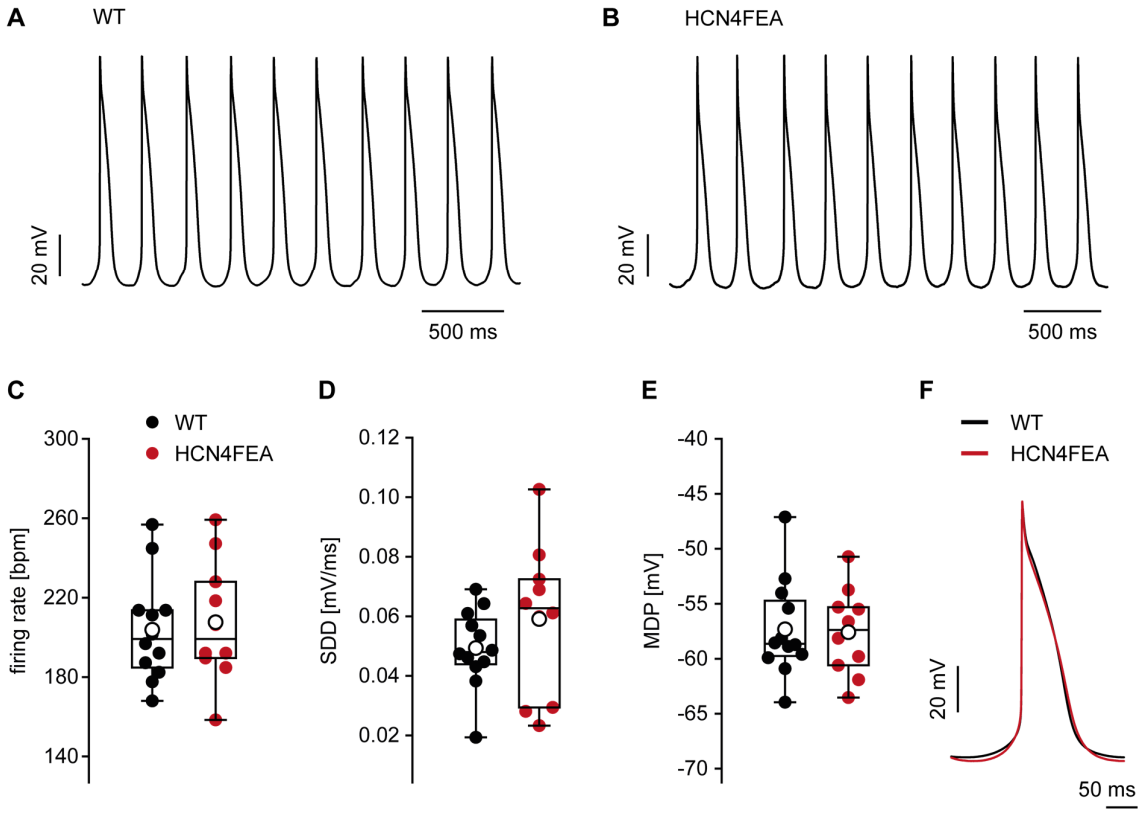

Figure 8. Firing characteristics of isolated SAN cells under baseline conditions. (A-B) Representative action potential traces recorded in SAN pacemaker cells isolated from a WT (A) and HCN4FEA mouse (B). **(C-E)** Mean firing rate, slope of slow diastolic depolarization (SDD), and maximum diastolic potential (MDP) of WT (black) and HCN4FEA cells (red). **(F)** Averaged action potentials obtained from representative recordings of a WT (black) and HCN4FEA cell (red).

Unexpectedly, however, in 90% of HCN4FEA cells a slow and progressive hyperpolarization (ΔV_m [HCN4FEA] = 7.17 ± 0.36 mV) was observed during episodes of rhythmic activity (Figure 9). This ultimately led to disruption of spontaneous action potential firing followed by extended periods of nonfiring, during which the cells remained at hyperpolarized membrane potentials. These episodes lasted for 28.9 ± 3.3 seconds and were characterized by slow recovery from the hyperpolarized potentials, until the cells finally returned to rhythmic firing.

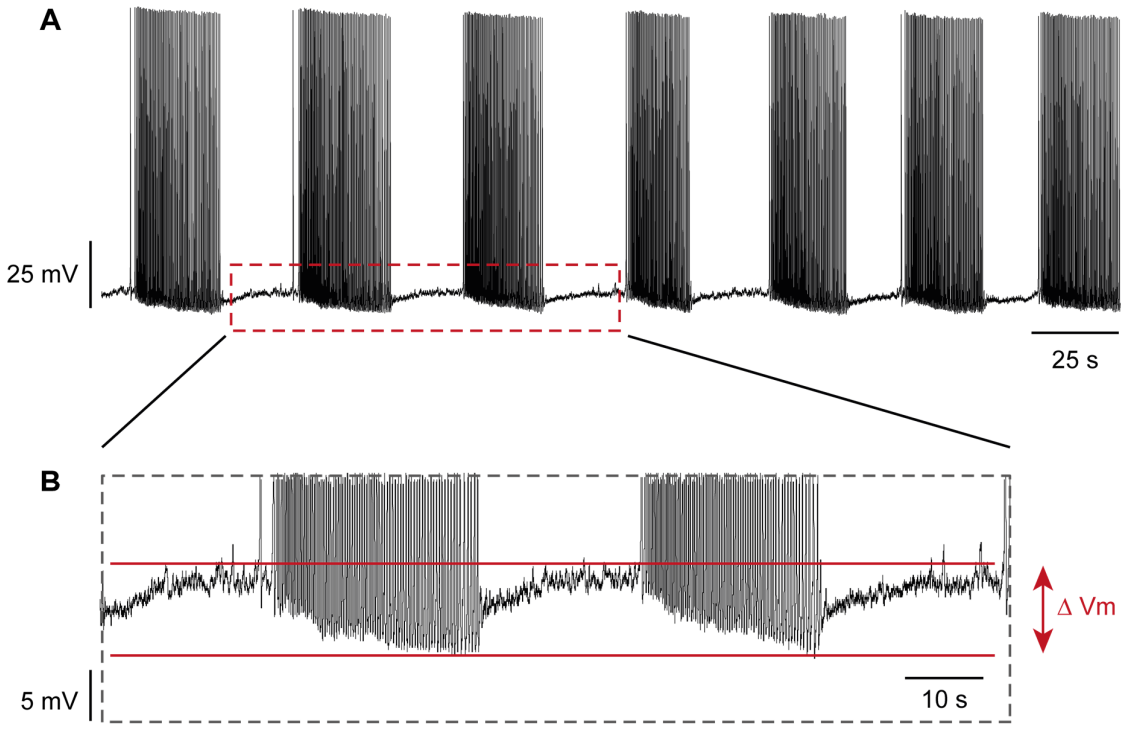

Figure 9. Discovery of the nonfiring activity mode in isolated SAN cells from HCN4FEA mice. (A) Representative long-term action potential recording of an HCN4FEA cell obtained with the perforated patch-clamp technique. The cell periodically alternates between the firing and nonfiring mode. During rhythmic firing the membrane potential progressively hyperpolarizes until firing stops. During nonfiring

the cell slowly recovers from the hyperpolarized potential and depolarizes until it returns to rhythmic firing. **(B)** Inset depicts magnification of the recording shown in (A) to illustrate the difference in membrane potential between onset and termination of the nonfiring episodes (ΔV_m).

Surprisingly, also in 42% of WT cells progressive hyperpolarization (ΔV_m [WT] = 8.16 ± 1.36 mV) was followed by 16.2 ± 1.5 seconds of nonfiring (Figure 10). This finding suggests that besides the well-known firing mode, a second and thus far uncharacterized nonfiring activity mode of SAN pacemaker cells exists. However, the occurrence of nonfiring was by far less pronounced in WT cells. Whereas HCN4FEA cells interrupted rhythmic firing for 37.7 ± 7.4% of the total measurement time, WT cells spent only 6.4 ± 2.8% of time in the nonfiring mode (Figure 10D). These results strongly suggest that CDR of HCN4 is involved in regulating the switch between the two activity modes and is important for maintaining firing and terminating episodes of nonfiring in SAN pacemaker cells.

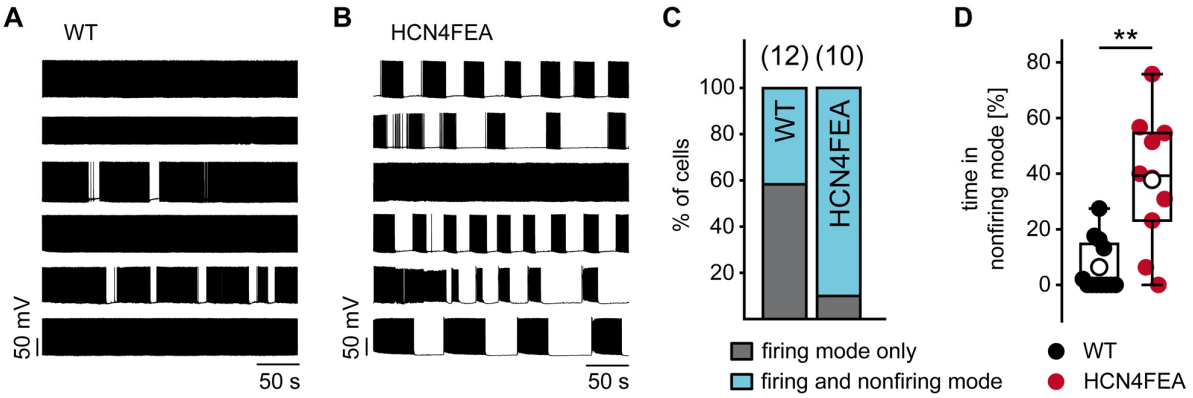

Figure 10. Baseline characterization of the nonfiring mode in WT and HCN4FEA cells. **(A-B)** Representative long-term action potential recordings of six SAN cells isolated from WT mice (A) and six cells from HCN4FEA mice (B). Each line represents a recording from a separate cell. **(C)** Quantification of cells displaying only the firing mode or both activity modes during long-term recordings. **(D)** Percentage of time spent in the nonfiring mode. Significance levels are determined with Mann-Whitney-U-test (** $p < 0.005$).

4.1.2 Application of isoproterenol

In the next experiment, the beta-adrenoceptor agonist isoproterenol (100 nM) was applied to the cells to test the response to increased intracellular cAMP levels by mimicking sympathetic activity (Figure 11). Isoproterenol significantly increased the firing rate and slope of SDD in WT and HCN4FEA cells to the same extent (Figure 11 A-B), suggesting that CDR of HCN4 may indeed not be required to mediate the positive chronotropic effect. Isoproterenol-induced effects on the maximum diastolic potential (MDP) were not observed (Figure 11C). Occurrence of the nonfiring mode, however, was completely abolished in WT cells upon application of isoproterenol, whereas the number of HCN4FEA cells displaying the nonfiring mode was reduced to 57.1% (Figure 11 D-E). This further supports a possible role of HCN4 CDR in regulating the switch between firing and nonfiring.

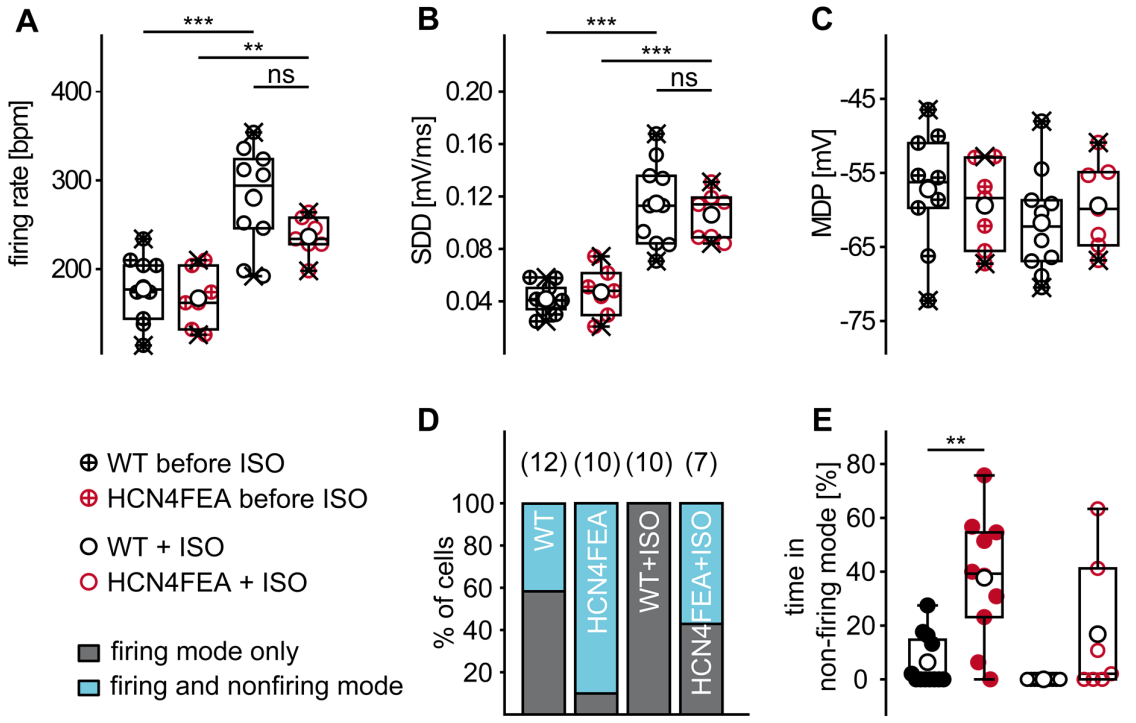

Figure 11. Isoproterenol-induced effects on the firing characteristics of SAN cells. (A-C) Mean firing rate, slope of slow diastolic depolarization (SDD), and maximum diastolic potential (MDP) of WT (black) and HCN4FEA cells (red) before and during superfusion with isoproterenol (ISO, 100 nM). **(D)** Quantification of cells displaying only the firing mode or both activity modes at baseline and in the presence of isoproterenol (ISO, 100 nM). **(E)** Percentage of time spent in the nonfiring mode under baseline conditions and during application of isoproterenol (100 nM). Significance levels in A-C are

determined with Sidakholm post-hoc test following two-way ANOVA (** $p < 0.005$; *** $p < 0.001$). Significance levels in E are determined with Mann-Whitney-U-test (** $p < 0.005$).

4.1.3 Application of carbachol

Next, increasing doses of the cholinergic agonist carbachol (10 nM, 100 nM, 1000 nM) were successively applied to the cells in order to simulate vagal activity and to investigate the firing characteristics of pacemaker cells under decreasing intracellular cAMP levels (Figure 12). Carbachol reliably induced the nonfiring mode in both WT and HCN4FEA cells and reduced the firing rate to the same extent (Figure 12B). The level of hyperpolarization caused by saturating concentrations of carbachol was similar in WT and HCN4FEA cells (Figure 12C). These results indicate that CDR of HCN4 might also not be involved in mediating the negative chronotropic effect. Rather, it provides a further line of evidence for an important role in controlling the transition between the two activity modes of SAN pacemaker cells.

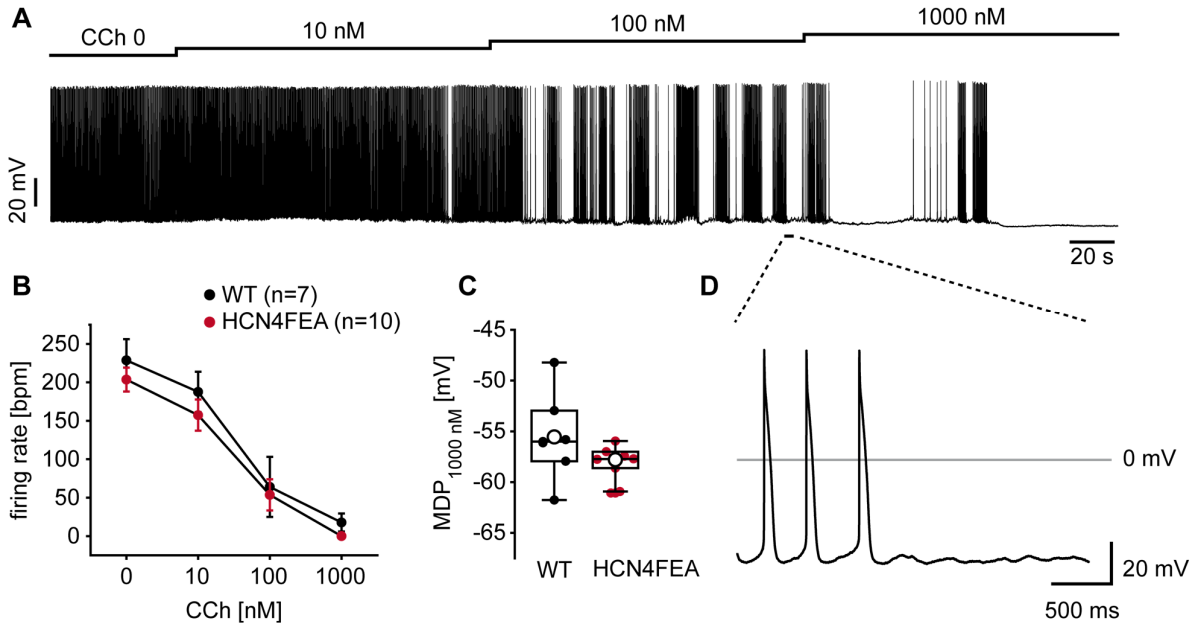

Figure 12. Carbachol (CCh) decreases the firing rate and induces nonfiring in SAN pacemaker cells. (A) Representative long-term current-clamp recording obtained from a WT SAN cell. After baseline measurement (CCh 0), the cells were directly superfused with successively increasing doses of carbachol (10 nM, 100 nM, 1000 nM). **(B)** Cumulative dose-response relationship of carbachol,

depicting the decrease in firing rate of WT (black) and HCN4FEA cells (red). **(C)** Maximum diastolic potential (MDP) of WT (black) and HCN4FEA cells (red) during application of 1000 nM carbachol. **(D)** Magnification of the recording shown in (A), illustrating the transition from firing to nonfiring.

4.1.4 Application of TAT-TRIP8b$_{nano}$

The next experiment was designed to specifically investigate whether the nonfiring mode can be induced by acutely preventing cAMP-dependent activation of HCN4. For this purpose, a membrane-permeable peptide (TAT-TRIP8b$_{nano}$) derived from the auxiliary HCN channel subunit TRIP8b was used (Figure 13). TAT-TRIP8b$_{nano}$ was designed to effectively bind to the CNBD of HCN channels, thereby preventing regulation by cAMP, and its efficacy was validated in SAN cells isolated from mice and rabbits (Saponaro et al., 2018). To assess the effect of TAT-TRIP8b$_{nano}$ on the firing pattern, long-term action potential measurements of WT SAN cells were taken after incubating the cells with the peptide. Indeed, in 100% of WT cells, application of TAT-TRIP8b$_{nano}$ induced and strongly enhanced occurrence of the nonfiring mode, followed by recovery to regular firing. These responses were even more pronounced than the baseline effects observed in the HCN4FEA mutant.

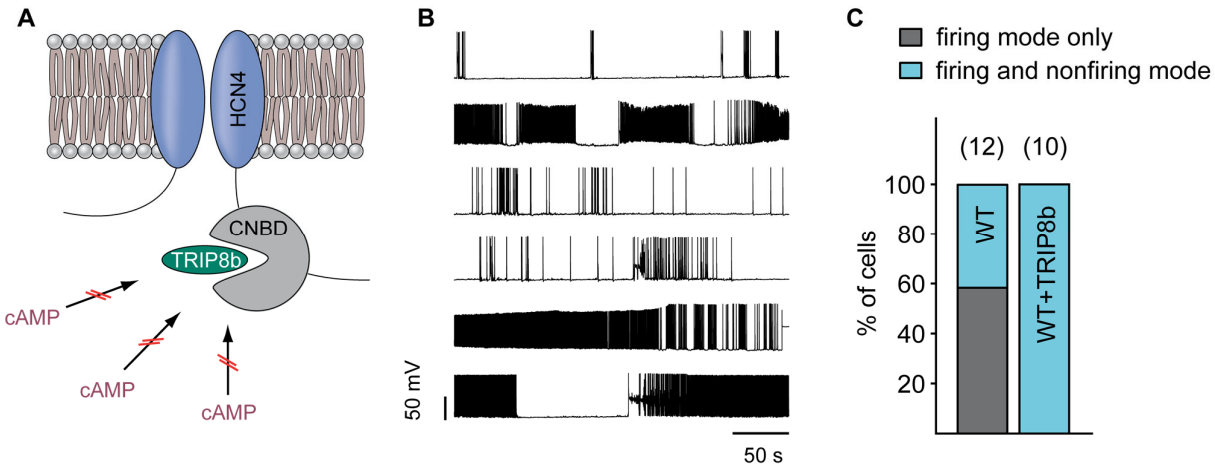

Figure 13. TAT-TRIP8b$_{nano}$ evokes nonfiring in WT SAN cells. (A) Cartoon illustrating the mode of action of TRIP8b. The peptide binds to the CNBD of HCN channels and thereby prevents cAMP-dependent activation. **(B)** Representative long-term action potential recordings of six WT SAN cells after incubation with TAT-TRIP8b$_{nano}$. Each line represents a recording from a separate cell. **(C)** Quantification

of cells displaying only the firing mode or both activity modes during long-term recordings of WT cells under baseline conditions and after application of TAT- TRIP8b$_{nano}$.

Taken together, the results from long-term action potential recordings demonstrate that CDR of HCN4 does not play a major role during baseline firing of SAN pacemaker cells. Furthermore, as determined by pharmacological characterization, HCN4 CDR is most likely not required to mediate the classical chronotropic effect following ANS activity. Surprisingly, the experiments uncovered that in addition to the canonical firing mode, a different and previously unknown nonfiring mode of SAN pacemaker cells exists. This activity mode is present in both WT and HCN4FEA cells, and the results strongly indicate that its frequency is directly controlled by CDR of HCN4.

4.2 Confocal imaging of intracellular calcium transients in the SAN network

How does the newly discovered nonfiring mode affect the intact SAN network? To answer this question, a confocal imaging approach was established that enables measurements of intracellular calcium transients in isolated whole-mount SAN preparations. Optimization of the method as well as related data acquisition were carried out in cooperation with Dr. Verena Brox[1].

4.2.1 Determination of experimental conditions

Since the SAN action potential is mainly carried by Ca^{2+} ions, global intracellular Ca^{2+} transients are only present during action potential firing and were used as a surrogate for pacemaker potentials. In order to measure Ca^{2+} signals in the SAN network, whole-mount SAN preparations were incubated with Fluo-4 AM, a cell-permeable derivative of the fluorescent calcium indicator Fluo-4 (Figure 14). After uptake into the cells, the acetoxymethyl ester (AM) is cleaved, which releases the free, fluorescent Fluo-4 molecule. Binding of Ca^{2+} to Fluo-4 increases the fluorescence intensity by more than 100-fold, along with an only minor wavelength shift (Gee et al., 2000). This makes the dye highly useful for confocal recordings of calcium transients in living tissue preparations.

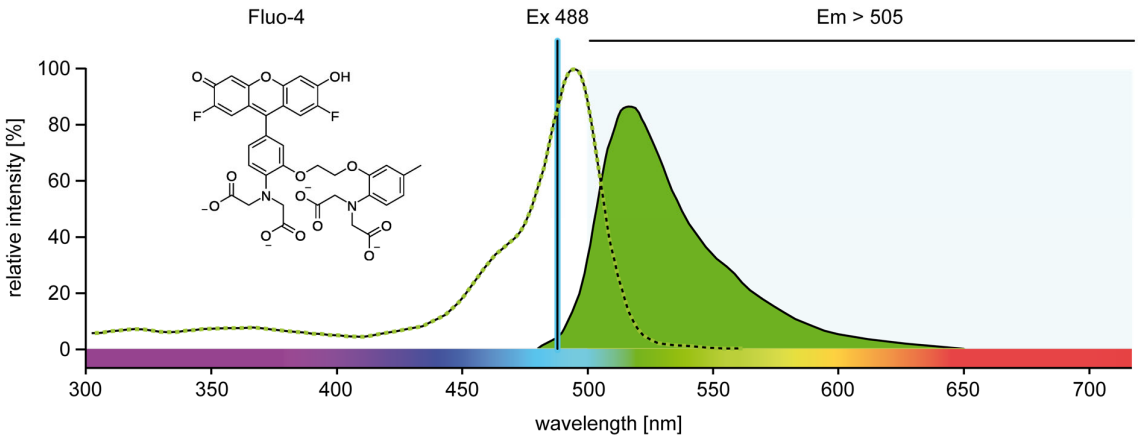

Figure 14. Excitation and emission properties of the green-fluorescent calcium indicator Fluo-4. The structural formula, excitation spectrum (dashed line) and emission spectrum (solid line) of Fluo-4

[1] Dr. Verena Brox. Former scientific collaborator at Pharmacology for Natural Sciences, Department of Pharmacy, Faculty for Chemistry and Pharmacy, Ludwig Maximilian University of Munich (2015-2019).

are shown. For confocal recordings of intracellular calcium transients, an excitation wavelength of 488 nm (blue line) was used and emission was detected at λ > 505 nm.

The SAN is located at the posterior side of the right atrium, extending from the superior vena cava along the sulcus terminalis towards the inferior vena cava (Liu et al., 2007). To gain access to the intact SAN tissue from the endocardial surface, whole-mount SAN preparations were dissected from hearts of WT and HCN4FEA mice (Figure 15) (Fenske et al., 2016). To this end, mice were sacrificed by cervical dislocation, beating hearts were quickly excised and transferred to a sylgard-coated petri dish filled with warm, oxygenated Tyrode's solution (37°C). The remaining part of the aorta was cannulated and the heart was retrogradely perfused with Tyrode's solution to flush any residual blood out of the atria and ventricles (Figure 15A). Subsequently, the larger part of the ventricles was cut off (Figure 15B) and after removing the aortic cannula, the position of the tissue was fixed to the sylgard surface with a pin inserted through the residual left ventricular wall (Figure 15C). Next, a single straight cut was made through the right ventricular wall, tricuspid valve and right atrial wall towards the superior vena cava (Figure 15D). A second incision at the right atrial appendage was made to expose the endocardial surface of the right atrium (Figure 15E). Remaining ventricular tissue and adjacent blood vessels were removed and the tissue preparation was carefully spanned as flat as possible and fixed to the sylgard surface with pins applied close to the edges (Figure 15F). Afterwards, the Tyrode's solution was removed and Fluo-4 loading buffer (20 µM) was directly pipetted onto the SAN region, followed by incubation at room temperature in the dark for 45 minutes. Finally, the loading buffer was washed out and the excitation-contraction-uncoupler blebbistatin (0.2 mg/ml) was applied in order to prevent the tissue explants from beating and to minimize motion artifacts in the recordings. After 5-10 minutes of equilibration, the Fluo-4-loaded whole-mount SAN preparations were used for confocal imaging of intracellular calcium transients in larger sections (Figure 16), and in individual pacemaker cells embedded in the intact SAN network (Figure 17). The experimental setup was composed of an upright Leica TCS SP8 confocal laser scanning microscope equipped with a 20x water immersion objective. The tissue was exposed to an excitation wavelength of 488 nm produced by an optically pumped semiconductor laser (OPSL) and calcium transients were recorded over time by detecting emission at wavelengths above 505 nm (Figure 14).

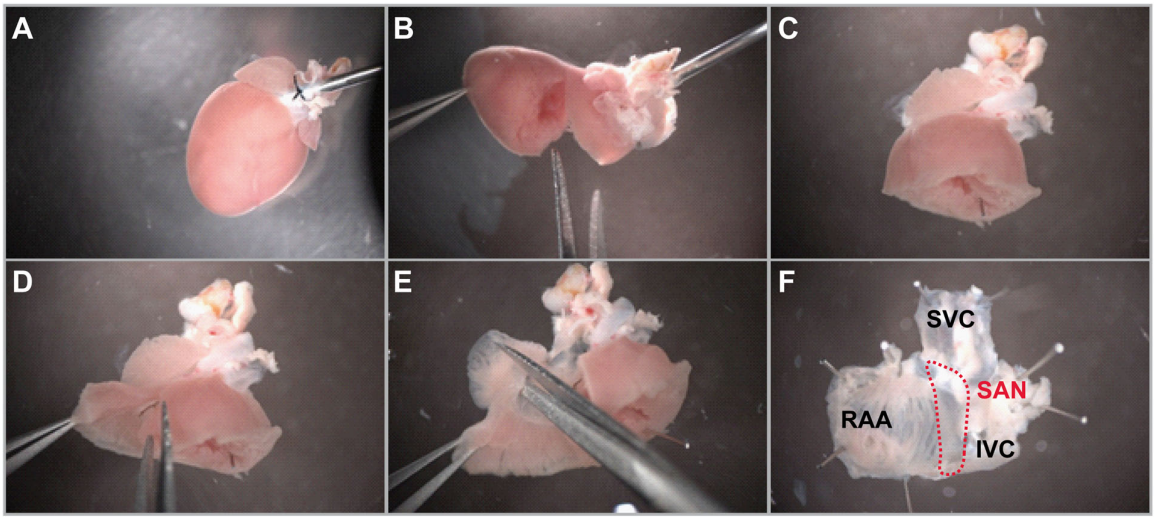

Figure 15. Dissection of intact whole-mount SAN preparations. (A) Excised mouse heart in a sylgard-coated petri dish. The remaining part of the aorta is cannulated to flush any residual blood out of the atria and ventricles. **(B)** The greatest part of the ventricles is cut off with scissors. **(C)** Aortic cannulation is removed and the tissue is fixed to the sylgard surface with a pin. **(D)** A single straight cut is made through the remaining right ventricular wall, tricuspid valve and right atrial wall towards the superior vena cava. **(E)** Another incision is made at the right atrial appendix, allowing the endocardial surface to be exposed. **(F)** The whole mount SAN preparation is spanned as flat as possible and its positions is fixed with pins applied close to the edges. Residual ventricular tissue and adjacent blood vessels were removed. The localization of the SAN region (red) is indicated. Abbreviations: SVC, superior vena cava; RAA, right atrial appendage; IVC, inferior vena cava; SAN, sinoatrial node.

4.2.2 Detection of subthreshold calcium signals

The measurements revealed that the substantial majority of individual pacemaker cells in WT SAN preparations generated global intracellular Ca^{2+} transients at a regular rhythm, indicating that these cells fire continuously without entering the nonfiring mode (Figure 16A, 17A). In a subset of HCN4FEA cells, however, variable phenomena of subthreshold Ca^{2+} activity were observed. One fraction of cells displayed highly localized, spontaneous Ca^{2+} events during diastole (Figure 16B). In other cells, local Ca^{2+} releases triggered propagated Ca^{2+} waves that were spreading uni- or bidirectionally along the long axis of the cell (Figure 17B). These Ca^{2+} signals were not always limited to a single cell but were also transmitted to surrounding cells, resulting in small cell clusters with irregular Ca^{2+} activity. The Ca^{2+} signals in these cells did not

evoke global Ca^{2+} transients and were not related to global Ca^{2+} transients of neighboring pacemaker cells, strongly suggesting that these cells are indeed nonfiring. Furthermore, the observations indicate that there are intercellular interactions between nonfiring pacemaker cells and neighboring cells in the firing mode, which can be expected to have a functional impact on the concerted activity of the whole SAN network.

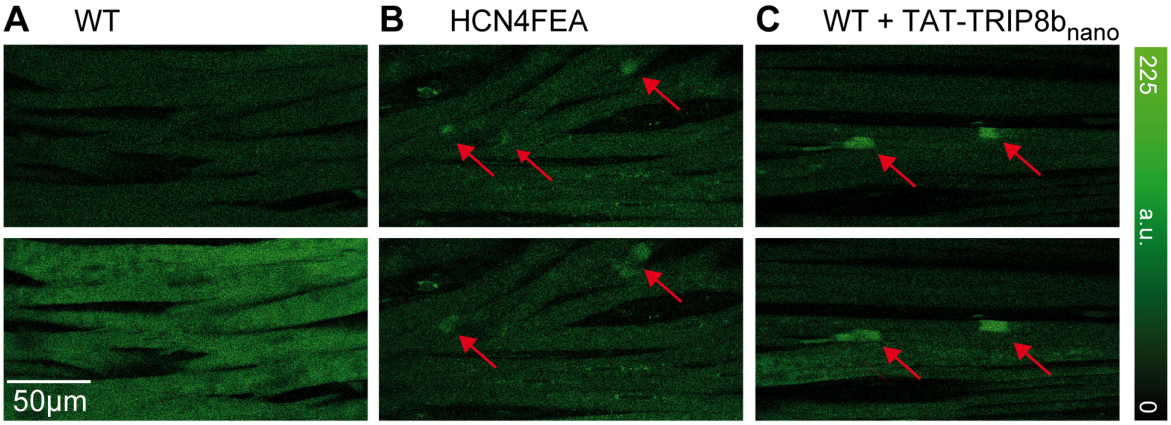

Figure 16. Confocal calcium imaging in optical sections of whole-mount SAN preparations. (A-C) Images of confocal calcium recordings from intact SAN tissue preparations of (A) WT, (B) HCN4FEA, and (C) WT after application of TAT-TRIP8b$_{nano}$. Right panel, reference for Fluo-4 fluorescence in arbitrary units [a.u.]. Red arrows indicate irregular subthreshold calcium signals observed in (B) HCN4FEA explants and (C) WT preparations after application of TAT-TRIP8bnano.

While under baseline conditions such irregular Ca^{2+} activity was only sporadically found in the WT SAN, it could reliably be induced by incubating the preparations with TAT-TRIP8b$_{nano}$ prior to experiments (Figure 16C, 17C). This further confirms that the subthreshold Ca^{2+} signals are directly caused by lack of HCN4 CDR, and that they represent a network phenomenon corresponding to the nonfiring mode observed in isolated SAN cells.

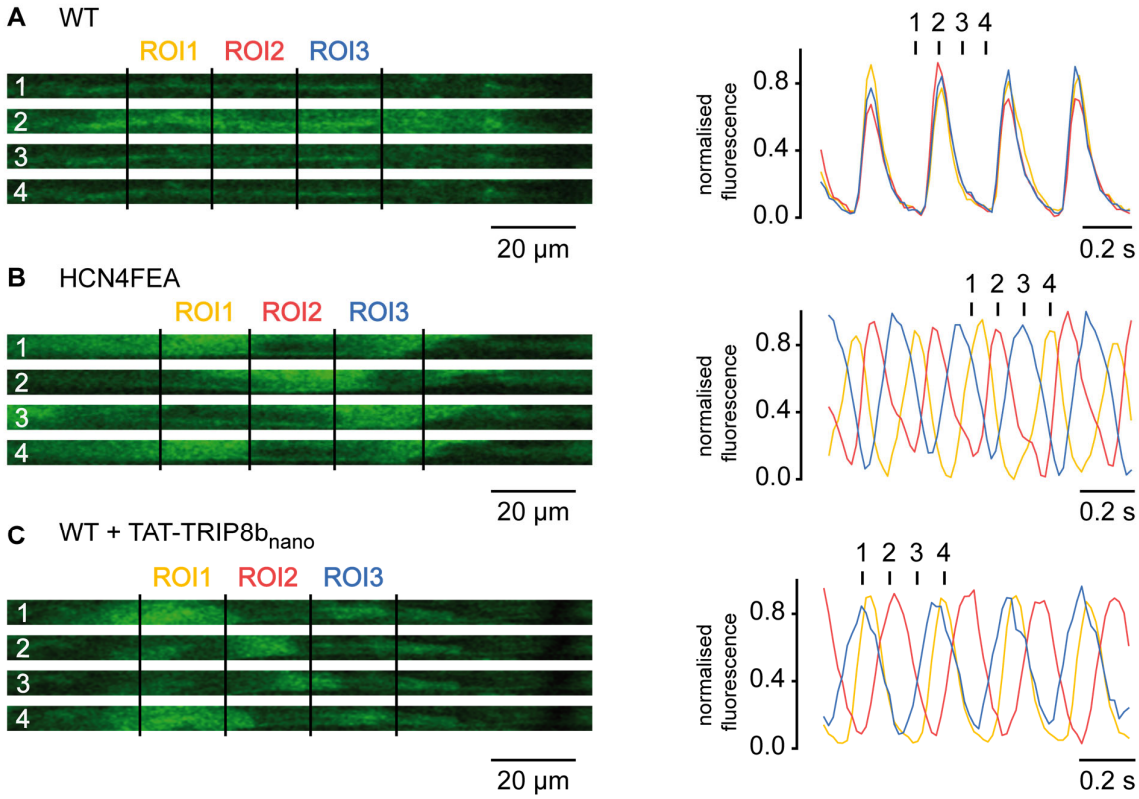

Figure 17. Confocal calcium imaging of single pacemaker cells embedded in the SAN network. (A-C) Left panels, time-lapse of confocal calcium recordings from single pacemaker cells embedded in the intact SAN network within tissue preparations from (A) WT, (B) HCN4FEA, and (C) WT after application of TAT-TRIP8b$_{nano}$. Images were taken at four consecutive time points numbered 1-4. Right panels, calcium transients calculated from the respective recordings in the left panels. Color coding corresponds to the regions of interest (ROI) indicated in the left panels. Time points 1-4 of the images shown in the left panels are indicated.

Taken together, the results from confocal imaging of calcium transients in whole-mount SAN preparations provide evidence that nonfiring pacemaker cells are also present in the intact SAN network. At the tissue level, the nonfiring mode becomes apparent due to irregular Ca^{2+} activity and lack of global intracellular Ca^{2+} transients. Moreover, the experiments uncovered a direct interaction between nonfiring pacemaker cells and surrounding cells in the firing mode, suggesting a functional influence of these cells on the overall SAN activity.

4.3 *In vivo* cardiac electrophysiological study (EPS)

In the next step, it was investigated how loss of HCN4 CDR affects overall SAN function and subsequent impulse propagation throughout the CCS *in vivo*. To this end, a right heart catheter-based electrophysiological study (EPS) in intact living animals was newly established and the experimental procedure was significantly refined to enable direct assessment of cardiac electrophysiological parameters (Hennis et al., 2021c). These include sinus node recovery time (SNRT), sinoatrial conduction time (SACT), AV-nodal conduction properties, Wenckebach periodicity, atrial and ventricular refractory periods, and vulnerability to atrial and ventricular arrhythmia. Specifically, the protocols to measure sinoatrial conduction time and AV-nodal refractory curves were derived from analogous human protocols (Rosenblueth, 1958; Narula et al., 1972; Strauss et al., 1973; Simson et al., 1979) and combined with previously published animal protocols (Berul et al., 1996; Berul, 2003; Li and Wehrens, 2010) to be optimized for application in the mouse heart. Moreover, atrial and ventricular burst stimulation protocols were adapted from the literature to investigate susceptibility to atrial and ventricular arrhythmias (Westphal et al., 2013; Clasen et al., 2018).

4.3.1 Surgical procedure

Performing *in vivo* EPS requires a surgical procedure during which an octapolar electrophysiology catheter is inserted into the right jugular vein and advanced into the right atrium and ventricle (Figure 18). This enables recording of intracardiac electrograms of the atrial and ventricular myocardium. At the same time, the catheter electrodes can be used for intracardiac pacing of the right atrium or ventricle. Programmed electrical stimulation protocols provide unique opportunities for detecting cardiac arrhythmias and investigating mechanisms that underlie defects in impulse formation or conduction.

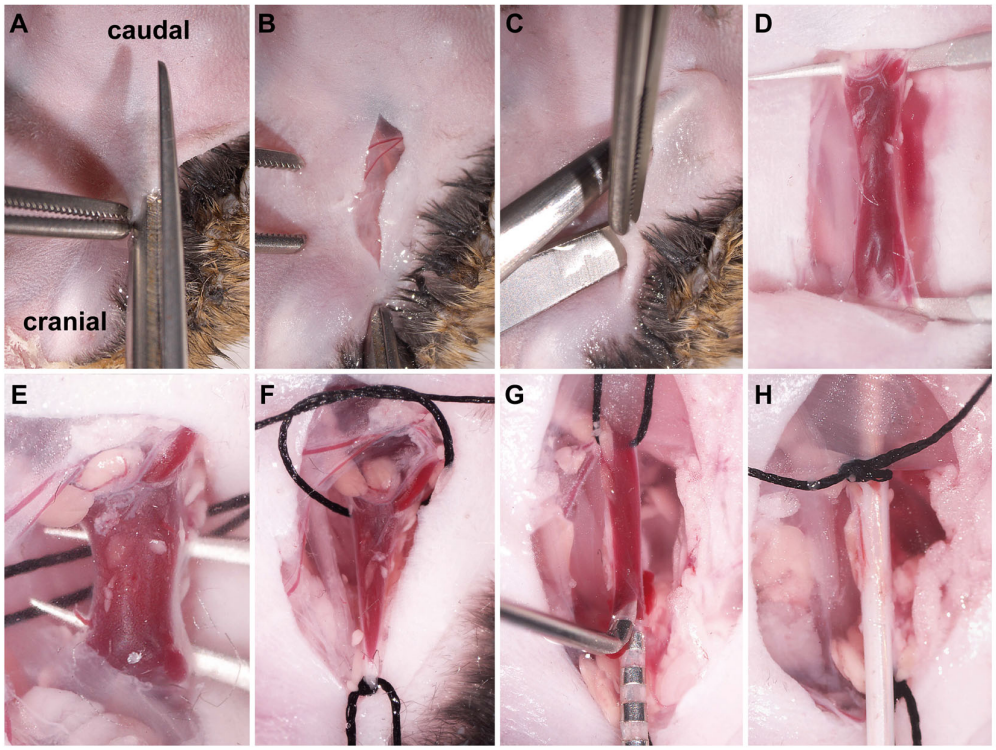

Figure 18. Surgical procedure of the *in vivo* EPS technique. (A-B) A straight incision is made from below the chin towards the chest area. **(C)** A subcutaneous pocket is formed with the blunt face of scissors. **(D)** The right external jugular vein is exposed and isolated from surrounding muscle and fat tissue. (**E)** Two surgical sutures are drawn underneath the blood vessel. **(F)** The proximal part of the jugular vein is tied off with a surgical knot and a second, loose knot is placed around the distal part. **(G)** A custom-made, angled cannula is used to puncture the vein at the most proximal part. The electrophysiology catheter is inserted into the opening underneath the cannula tip and advanced towards the heart. **(H)** Once the catheter is located in the correct position, the second suture is secured to fix the position of the catheter tip inside the heart. Figure is adapted from (Hennis et al., 2021c).

To prepare mice for surgery, anesthesia was induced and maintained by isoflurane inhalation, and lidocaine was subcutaneously administered across the surgical area to ensure sufficient local anesthesia. Subcutaneous needle electrodes were applied to the limbs in order to obtain surface ECG recordings during the entire procedure. Subsequently, a straight skin incision was made from below the chin towards the transversal pectoral muscles (Figure 18 A-B), and a subcutaneous pocket was formed using the blunt face of scissors (Figure 18C). The right external jugular vein was

exposed and isolated by bluntly dissecting surrounding muscle and fat tissue with angled forceps (Figure 18D). Two surgical sutures were drawn underneath the blood vessel (Figure 18E) and the first suture was placed to the most proximal part of the jugular vein. A surgical knot was formed and the vein was tied off as close to the head as possible. Tension was applied by retracting the suture towards the head with a clamp (Figure 18F). A loose knot in the second suture was formed and the suture end was gently pulled towards the tail with a needle holder. This stretches the jugular vein, resulting in temporary obstruction of blood flow. A custom-made, angled cannula was used to puncture the vein at the most proximal part. The vascular wall was slightly lifted and the electrophysiology catheter was carefully inserted into the opening underneath the cannula tip (Figure 18G). The cannula was removed and the catheter was pushed forwards, while its position was monitored by observing the electrical signals on the computer screen. Once the electrodes were located in the right atrium and ventricle, as judged by the intracardiac ECG signals, the second suture was secured to keep the catheter fixed in its position (Figure 18H).

After completion of surgery, the correct catheter placement was verified by comparing surface and intracardiac ECG traces (Figure 19). The surface ECG recordings consist of three different traces according to Einthoven lead I, II, and III (Figure 19A). The intracardiac recordings consist of two atrial leads (HRAd, distal high right atrium; HRAp, proximal high right atrium) and two ventricular leads (RVd, distal right ventricle; RVp, proximal right ventricle) (Figure 19B). The designations *proximal* and *distal* describe the location of the electrodes relative to the catheter tip. In case of correct catheter placement, the P waves and QRS complexes in the surface ECG occur synchronously to the atrial (A) and ventricular (V) signals in the intracardiac traces. In the atrial leads, the size of A signals is greater than that of V signals because the respective electrodes are located in the right atrium. The opposite applies to the ventricular leads, where V signals are larger than A signals because the corresponding electrodes are located in the right ventricle. In some experiments, a small His signal (H) can be detected in the RVd lead, indicating electrical activation of the His bundle (Figure 19B).

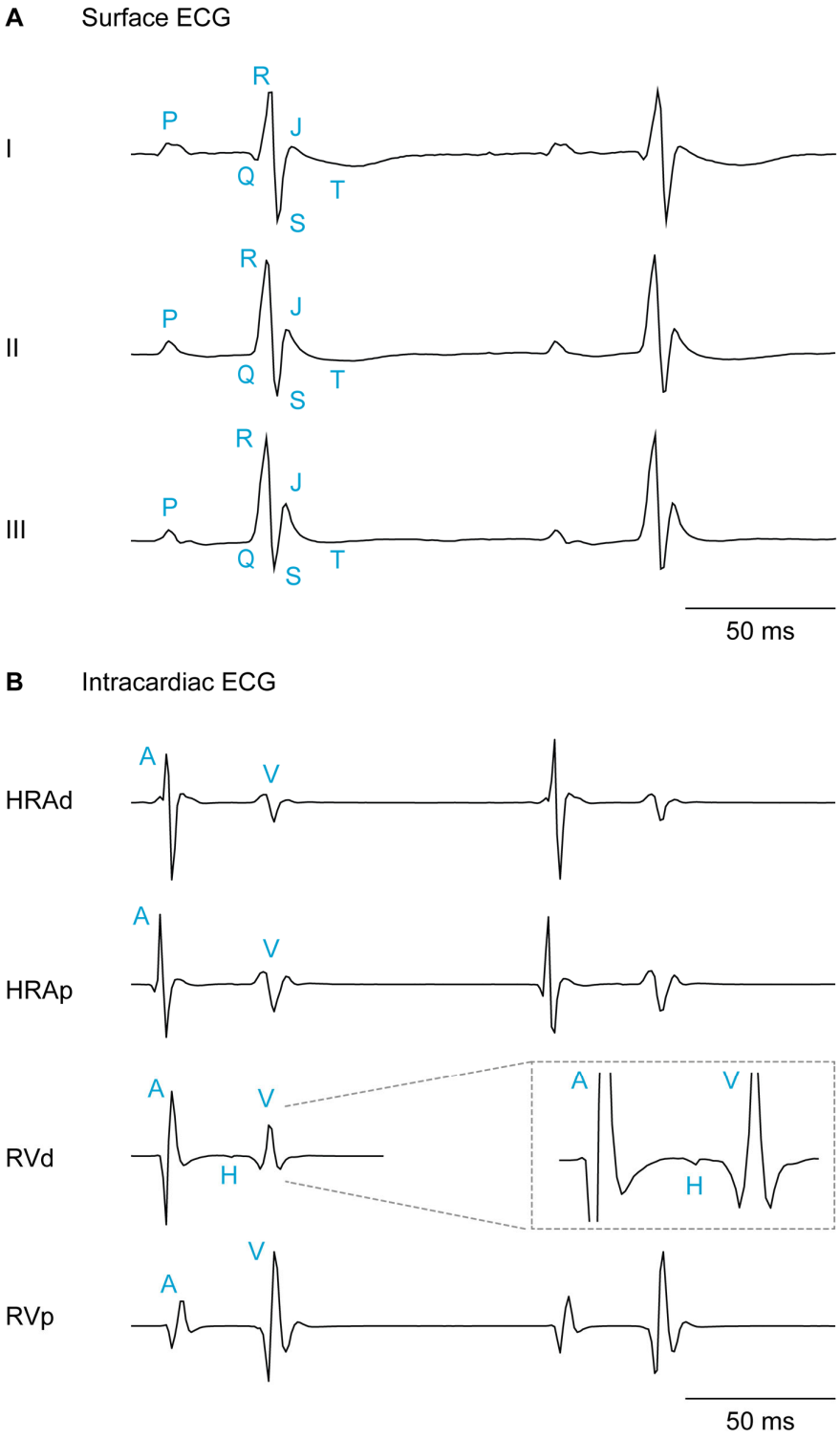

Figure 19. Simultaneous surface and intracardiac ECG recordings. **(A)** Surface ECG traces according to Einthoven lead I, II, and III. The P wave reflects atrial activation, followed by the QRS

complex which represents ventricular activation. The J wave marks early ventricular repolarization and the T wave indicates end of ventricular repolarization. **(B)** Intracardiac ECG recordings (HRAd, distal high right atrium; HRAp, proximal high right atrium**;** RVd, distal right ventricle; RVp, proximal right ventricle). The P waves and QRS complexes in the surface ECG leads occur synchronously to the atrial (A) and ventricular (V) signals in the intracardiac leads. Sometimes, a small His signal (H) can be detected in the RVd lead. Figure is adapted from (Hennis et al., 2021c).

4.3.2 Programmed electrical stimulation protocols

During programmed electrical stimulation, the catheter delivers constant current pulses, and the atrial or ventricular electrodes can be individually chosen as output electrodes in order to pace the right atrial or ventricular myocardium, respectively. The responses to the specific stimulation protocols are recorded and retrospectively analyzed to determine a variety of cardiac electrophysiological parameters. To this end, the time intervals between any two points of the recordings can be measured with an accuracy of ± 1 ms. Afterwards, these values are transferred to a spreadsheet software to perform calculations, graph plotting and statistical analysis. In this study, the following stimulation protocols were used:

4.3.2.1 Sinus node recovery time (SNRT)

Sinus node recovery time is a measure for the integrity and functionality of SAN automaticity. In a diseased SAN with impaired impulse formation, SNRT will be prolonged. To determine SNRT, SAN automaticity is effectively suppressed by atrial overdrive pacing (Figure 20). To this end, a 30 second train of atrial stimuli at a fixed pacing cycle length (S1S1) below the intrinsic sinus cycle length is applied. Upon termination of overdrive pacing, the time interval between the last stimulation spike and the first spontaneous, sinus node triggered atrial activation (S1A2) is measured, which reflects the time required for SAN recovery and return to spontaneous sinus rhythm. This value is directly influenced by the baseline heart rate. To correct for differences in heart rate, rate-corrected SNRT (cSNRT) is calculated by subtracting the average sinus cycle length (SCL) from SNRT.

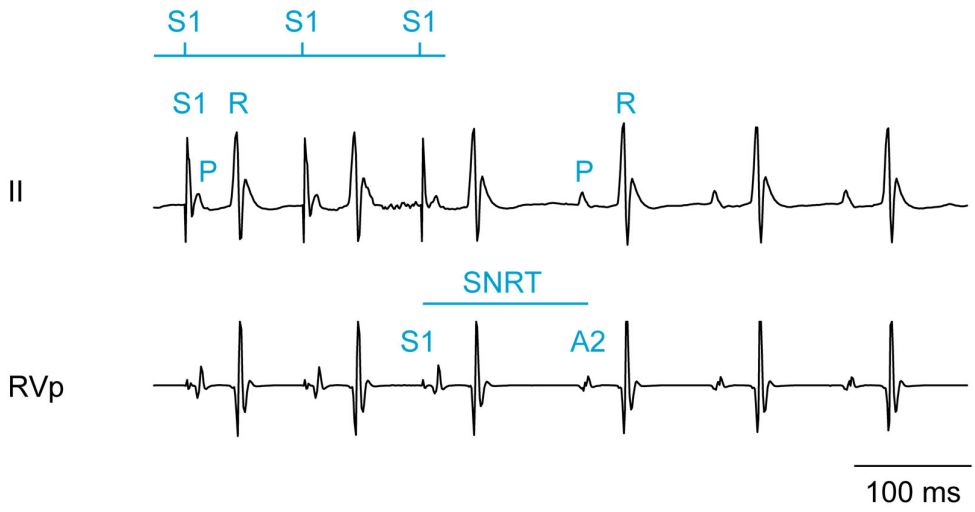

Figure 20. Stimulation protocol to determine sinus node recovery time (SNRT). Timing of stimuli, surface ECG lead II and intracardiac lead RVp are displayed. SNRT is defined as the time interval between the last stimulation spike and the first spontaneous, sinus node triggered atrial activation (S1A2). Figure is adapted from (Hennis et al., 2021c).

4.3.2.2 Strauss method to determine sinoatrial conduction time (SACT)

Sinoatrial conduction time is defined as the time interval required for an electrical impulse generated in the SAN to exit the nodal tissue and to reach the surrounding atrial myocardium. SACT will be prolonged in a diseased SAN, in which impulse propagation through the nodal tissue and its exit pathways is impaired. In analogy to human studies (Narula et al., 1972; Strauss et al., 1973; Reiffel et al., 1974; LaBarre et al., 1979), two different methods were established to indirectly determine SACT by premature atrial stimulation. The Strauss method makes use of single atrial stimuli randomly applied during spontaneous sinus rhythm. To this end, up to 100 stimuli are applied to scan through the entire sinus cycle. At each stimulation event, the baseline cycle length (A1A1), coupling interval of the premature atrial signal (A1A2), return cycle length (A2A3), and post-return cycle length (A3A4) are measured. For data analysis, the A2A3 and A3A4 intervals are plotted against the corresponding A1A2 intervals (Figure 21A). To account for differences in the baseline heart rate, all intervals can be normalized to the atrial baseline cycle length (A1A1) and the calculated ratios are

plotted accordingly (Figure 21B). Data analysis with absolute time intervals and normalized cycle lengths is carried out identically.

Within the respective graphs, four different zones can be identified based on the differential responses to premature stimulation. To do so, four different straight lines are constructed.

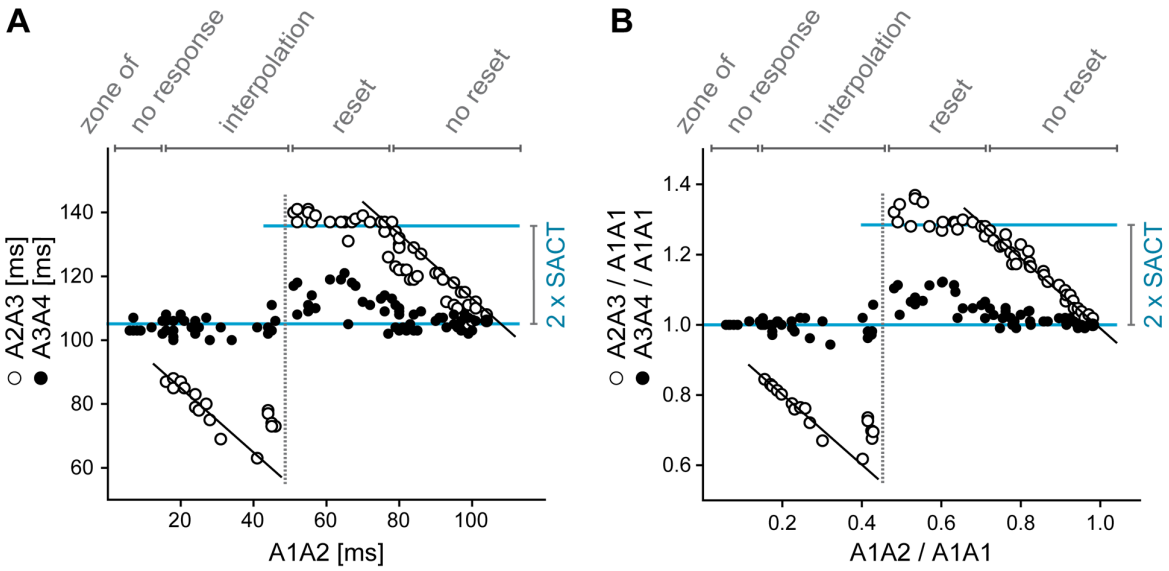

Figure 21. Strauss method to determine sinoatrial conduction time (SACT). (A) Up to 100 premature atrial stimuli are applied during spontaneous sinus rhythm. For data analysis, the return cycle lengths (A2A3) and post-return cycle lengths (A3A4) are plotted against the corresponding coupling intervals of the premature stimulus (A1A2). See text for further details. **(B)** To correct for differences in baseline heart rate, all values are normalized to the baseline cycle length (A1A1) and data analysis is carried out analogously. Figure is adapted from (Hennis et al., 2021c).

First, a horizontal straight line is constructed that represents the mean baseline cycle length during all stimulation events (mean A1A1 value, lower horizontal line (blue) in Figure 21A). Ideally, the post-return cycle lengths (A3A4 values) lie close to this line, indicating that the spontaneous sinus rhythm was only minimally disturbed by premature stimulation (Reiffel et al., 1974; Kugler et al., 1979). In addition, a diagonal straight line is constructed, that intersects the x-axis at (2xA1A1/0) and the y-axis at (0/2xA1A1) (slope = -1; upper right part of the graph). At long A1A2 intervals, the A2A3 data points lie on this line, which is referred to as line of full compensatory pauses

(given by: A2A3 = 2x A1A1 – A1A2 (Figure 21A) or, in case of normalized cycle lengths, given by: y = 2 – A1A2/A1A1 (Figure 21B)). The corresponding zone is called zone of no reset, because the A1A2 intervals are too long for the stimuli to penetrate and reset the SAN before it generates the next spontaneous impulse (Figure 22A). Consequently, the atrial excitations generated by premature stimulation (A2) collide with the impulses generated by the SAN and both become extinguished, leading to pauses in spontaneous atrial depolarizations. These pauses are fully compensatory, because the respective intervals are twice as long as the A1A1 intervals during baseline sinus rhythm (A1A2 + A2A3 = 2x A1A1).

At successively shorter A1A2 intervals, the A2A3 values deviate from the line of full compensatory pauses and yield a plateau. A second horizontal line is constructed (upper horizontal line (blue) in Figure 21A), which intersects the line of full compensatory pauses at the point where the A2A3 values begin to deviate from it. The pauses are no longer fully compensatory (A1A2 + A2A3 < 2x A1A1) and the corresponding zone is called zone of reset, because the stimuli penetrate and reset the SAN before the next spontaneous impulse is generated (Figure 22B). Under the assumption that impulse propagation into and out of the SAN is equally fast, SACT can be derived from the first A2A3 intervals deviating from the line of full compensatory pauses. Accordingly, the difference between these return cycle lengths (A2A3, upper horizontal line) and the baseline cycle lengths (A1A1, lower horizontal line), divided by two, gives the sinoatrial conduction time according to the Strauss method (SACT SM).

$$\text{SACT SM} = \frac{\text{A2A3} - \text{A1A1}}{2}$$

At further decreasing A1A2 coupling intervals, a sudden transition to shorter return cycle lengths occurs, which marks the beginning of the zone of interpolation. A second diagonal line is constructed that intersects the x-axis at (1xA1A1/0) and the y-axis at (0/1xA1A1) (slope = -1; lower left part of the graph in Figure 21A). This line is termed line of complete interpolation (given by: A2A3 = A1A1 – A1A2 or, in case of normalized cycle lengths, given by: y = 1 – A1A2/A1A1), because the premature stimuli fail to enter the SAN due to refractoriness of the surrounding perinodal tissue (Figure 22C).

Consequently, the atrial responses A2 are completely interpolated between two regular, SAN-triggered atrial activations (A1A2 + A2A3 = A1A1).

At even shorter A1A2 intervals, the premature stimuli do not elicit atrial responses due to refractoriness of the atrial myocardium (atrial effective refractory period, AERP). The corresponding zone is referred to as zone of no response (Figure 22D).

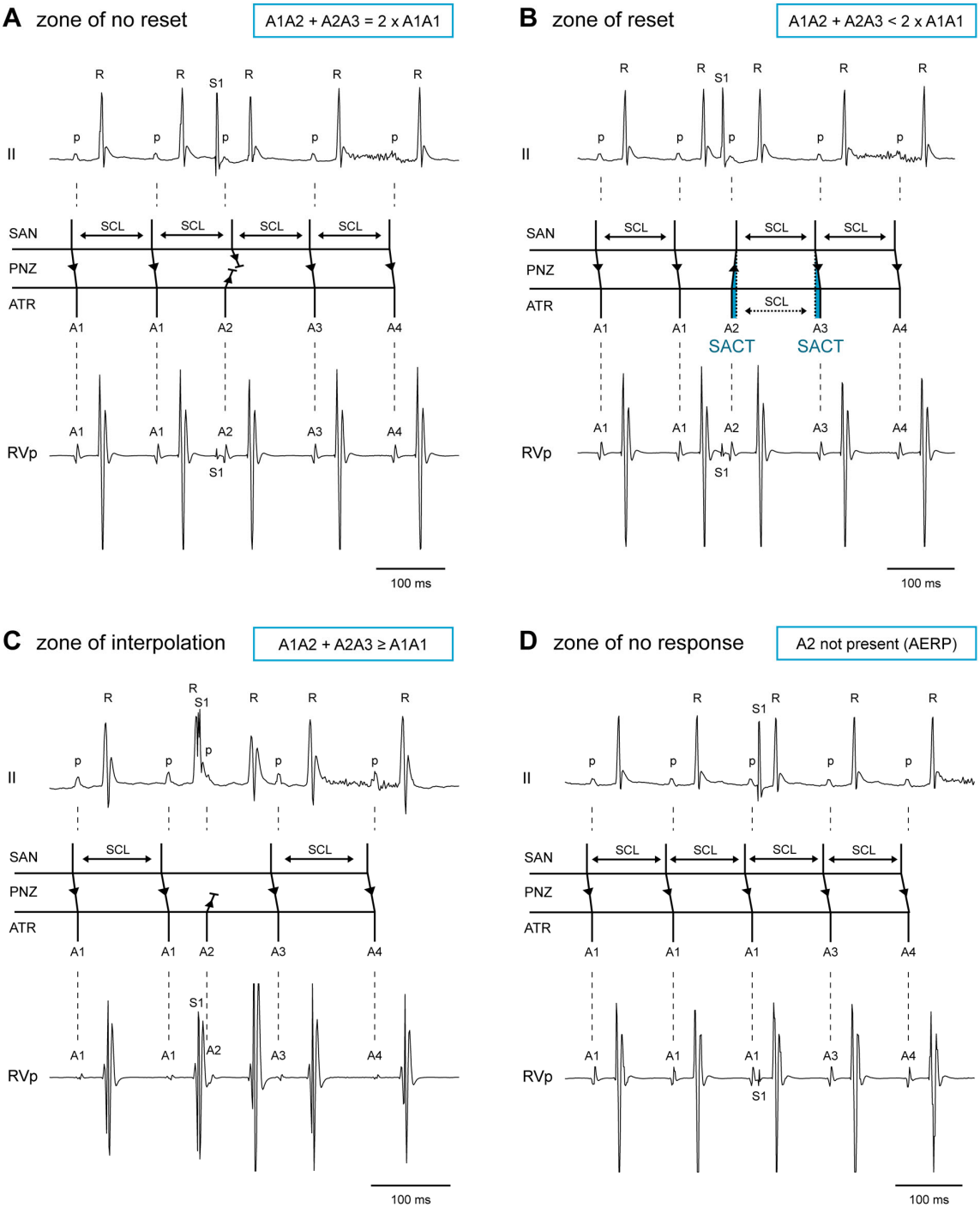

Figure 22. ECG recordings during measurement of SACT with the Strauss method. Surface ECG lead II (upper panels) and intracardiac ECG lead RVp (lower panels) during the SACT stimulation protocol are depicted. The underlying mechanisms in the SAN, perinodal zone (PNZ) and right atrium (ATR) are visualized in the middle panels. **(A)** Zone of no reset. The A1A2 intervals are too long for the stimuli to penetrate and reset the SAN before it generates the next spontaneous impulse. Therefore, the atrial excitations generated by premature stimulation (A2) collide with the impulses generated by the SAN and become extinguished, leading to pauses in spontaneous atrial depolarizations. **(B)** Zone of reset. The stimuli penetrate and reset the SAN before the next spontaneous impulse is generated. In the zone of reset, SACT can be derived by dividing the difference between the return cycle lengths (A2A3) and the baseline cycle lengths (A1A1) by two. **(C)** Zone of interpolation. The premature stimuli fail to enter SAN due to refractoriness of the surrounding tissue. Consequently, the atrial responses A2 are completely interpolated between two regular SAN-triggered atrial activations. **(D)** Zone of no response. The premature stimuli do not elicit atrial responses due to refractoriness of the atrial myocardium (atrial effective refractory period, AERP). Figure is adapted from (Hennis et al., 2021c).

4.3.2.3 Narula method to determine sinoatrial conduction time (SACT)

In contrast to the Strauss method, which is used to measure SACT during spontaneous sinus rhythm, the Narula method is based on a train of eight atrial stimuli (S1) applied at a fixed pacing cycle length (Figure 23).

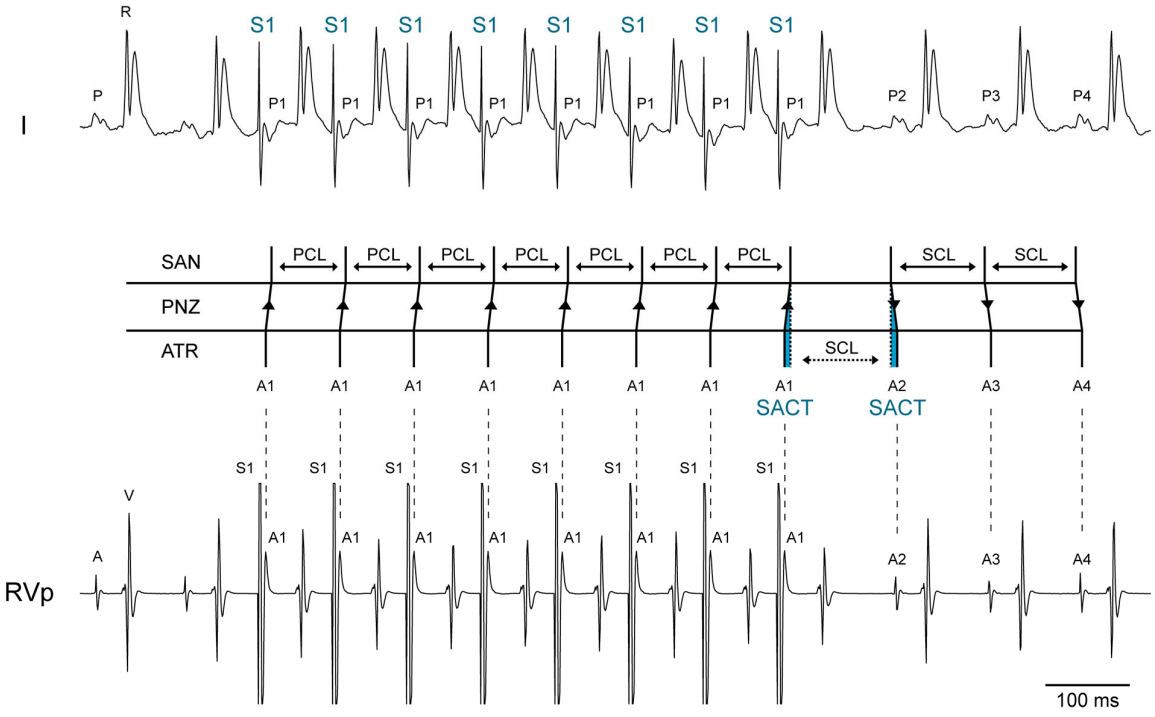

Figure 23. ECG recordings during measurement of SACT with the Narula method. Surface ECG lead I (upper panel) and intracardiac ECG lead RVp (lower panel) during the SACT stimulation protocol are depicted. The underlying mechanisms in the SAN, perinodal zone (PNZ) and right atrium (ATR) are visualized in the middle panel. See text for details. Figure is adapted from (Hennis et al., 2021c).

For the pacing cycle length (PCL), S1S1 intervals are chosen that are only slightly shorter than the intrinsic sinus cycle length (SCL). This ensures that atrial stimulation will not induce substantial overdrive suppression. The method relies on the assumption that the premature stimuli penetrate and reset the SAN, with equally fast impulse propagation into and out of the SAN. Following atrial stimulation, the return cycle length (A1A2) and post-pacing sinus cycle length (A2A3) are measured. In analogy to the Strauss method, SACT according to the Narula method (SACT NM) is calculated as the difference between A1A2 and A2A3, divided by two.

$$\text{SACT NM} = \frac{\text{A1A2} - \text{A2A3}}{2}$$

4.3.2.4 AV-nodal conduction properties

Conduction properties of the AVN can be best described and quantified by assessing refractoriness of the tissue. During the refractory period, depolarized tissues cannot be re-excited by premature stimulation. However, this rule should not be considered absolute, since there are gradual degrees of refractoriness depending on the timing of premature stimulation. Therefore, a series of stimuli applied during and after the end of repolarization will induce differential responses. Very early stimulations during the absolute refractory period (ARP) do not induce a response at all. Later stimulations elicit graded responses that are not conducted through the tissue, and the corresponding time frame is called effective refractory period (ERP). During the relative refractory period (RRP), the stimuli induce responses with reduced amplitude, duration, and upstroke velocity, and these responses are propagated through the tissue by reduced speed. Subsequent stimuli that are applied after the end of repolarization elicit normal responses, indicating that the tissue has fully recovered.

In the AVN, individual cells are connected via gap junctions and electrical impulses can only be conducted from one cell to its neighboring cells. Since functionally different types of cardiac tissue as well as junctions between these tissues are present, propagation of electrical activity in the AVN is discontinuous (Rosenblueth, 1955; 1958; Jalife, 1983). From proximal to distal, three functionally distinct regions are longitudinally connected, namely 1) the transitional cell zone, 2) the central zone of the compact AVN, and 3) the penetrating part of the His bundle (Figure 24A) (De Carvalho and De Almeida, 1960; Jalife, 1983). Accordingly, three different cell types with distinct electrophysiological properties are present in the AVN and perinodal region, i.e., the atrionodal (AN), nodal (N), and nodal-His (NH) cells (Figure 24A) (Hoffman et al., 1958; De Carvalho and De Almeida, 1960; Efimov et al., 2004). The AN cells are located in the transitional cell zone and display intermediate functional properties between atrial and nodal cells. The N cells make up the central zone and are responsible for the major part of AV conduction delay following premature stimulation. This conduction delay is caused by a slower rising phase and longer duration of action potentials in N cells, which can be attributed to lower Na^+ channel expression and to the fact that action potentials are mainly driven by inward L-type Ca^{2+} currents. The NH cells are found in the penetrating part of the His bundle and have intermediate properties between N cells and His bundle cells. Due to depressed excitability and decremental conduction, impulse propagation in the central zone is slower than in the fully excitable AN and NH cell zones. During normal sinus rhythm, impulses arrive from the atrial myocardium and are propagated across the different AV nodal tissue zones to the ventricles, without significantly impaired conduction velocity. Upon premature stimulation, however, electrical signals can arrive in a central tissue region that has only partially recovered from a previous depolarization. Consequently, the impulses will stop in the central AV node, become extinguished, or will be re-initiated and further conducted after a delay that is necessary for recovery from the previous depolarization, leading to discontinuous AV conduction (Jalife, 1983).

The EPS stimulation protocols designed to determine AV-nodal conduction properties make use of discontinuous conduction induced by progressively premature stimulation (Figure 24B). The stimuli (S) are applied to the right atrium (A), which is located proximally to the AVN and represents the input to the AV conduction system. The response is recorded at the distally located His bundle (H) or right ventricle (V), representing the output of the system. First, a train of eight stimuli at a fixed pacing

cycle length (S1S1) below the intrinsic sinus cycle length is applied, allowing for reasonable stabilization of refractoriness. Subsequently, one extrastimulus (S2) is applied and the S1S2 coupling intervals are reduced stepwise in order to scan through the full range of atrial diastole. By use of this protocol, AV-nodal recovery curves and refractory curves can be obtained (Figure 25).

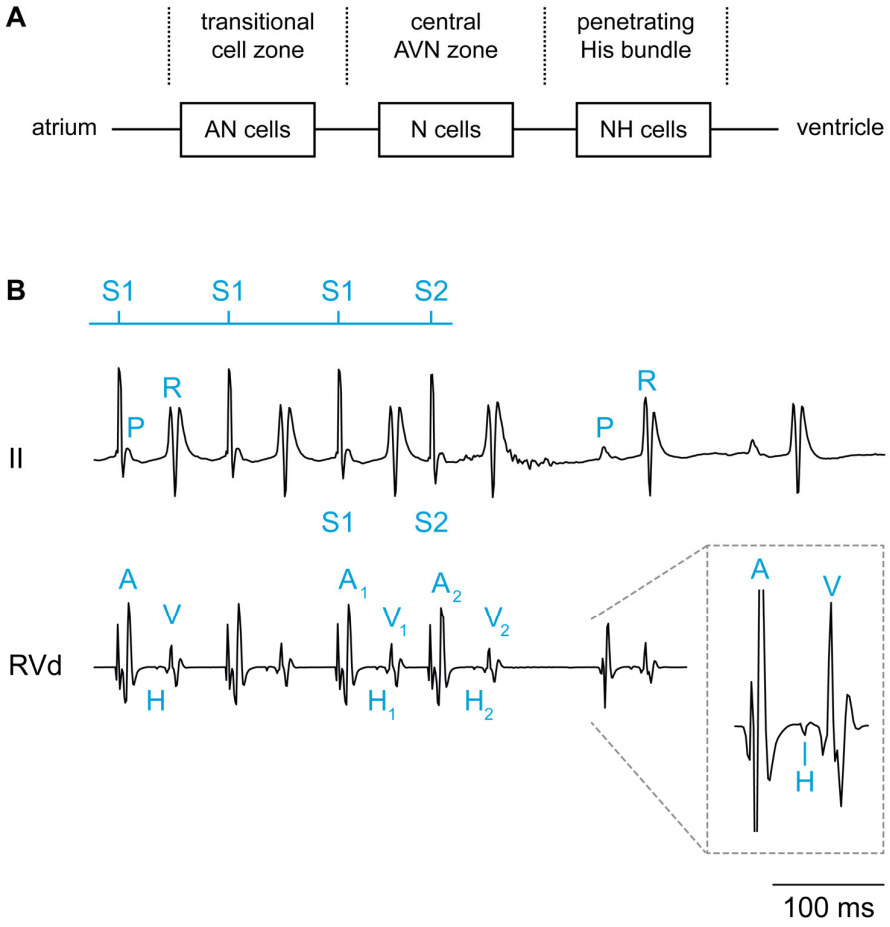

Figure 24. AV-nodal conduction properties are investigated by premature atrial stimulation. (A) Schematic model of the AV conduction system. The AVN consists of three functionally distinct, longitudinally connected regions, which are composed of three different cell types with distinct electrophysiological properties. See text for further details. **(B)** Stimulation protocol used for determination of AV-nodal refractory periods. Timing of stimuli, surface ECG lead II and intracardiac lead RVd are displayed. Figure is adapted from (Hennis et al., 2021c).

Recovery curves are constructed by plotting A2V2 (or A2H2) against A1A2 (Figure 25A) (Rosenblueth, 1958; Simson et al., 1979; Billette, 1987). At successively decreasing A1A2 intervals, the A2V2 latency intervals increase. There is only a minor A2V2 lengthening for relatively long A1A2 intervals (right part of the curve). At shorter A1A2 intervals, the A2V2 lengthening becomes progressively larger (left part of the curve). The diagonal line (slope = -1) indicates the segment of the curve at which A2V2 lengthening is equal to A1A2 shortening. At even shorter A1A2 intervals, A2V2 lengthening further increases until AV-nodal conduction is lost. The purpose of the recovery curve is to visualize the conduction time through the AVN as a function of the available recovery time from the last successful antegrade impulse conduction.

To construct AV-nodal refractory curves, the output intervals V1V2 (or H1H2) are plotted against the corresponding input intervals A1A2 (Figure 25B). These curves can be analyzed to quantify the relative (AVRRP), functional (AVFRP), and effective refractory period of the AV conduction system (AVERP). As atrial intervals (A1A2) become shorter due to progressively premature stimulation, ventricular intervals (V1V2) also progressively decrease. At relatively long A1A2 intervals, these decreases are proportional to each other and the data points fall on a straight line (identity line, slope = +1; right part of the refractory curve). This line depicts the theoretical curve of no AV conduction delay. At a certain point of A1A2 shortening, decremental conduction occurs. As a consequence, the A2V2 conduction time increases and the corresponding V1V2 intervals fall above the identity line. The point at which AV conduction delay first occurs marks the beginning of the relative refractory period of the AV conduction system (AVRRP). Subsequently, the V1V2 intervals further decrease until a minimum value is reached, which indicates the functional refractory period (AVFRP). This parameter is a measure of the output from the AVN tissue (y-value of the minimum of the refractory curve) and quantitatively describes the ability of the tissue to sustain conduction of premature impulses, thereby indicating the fastest possible conduction velocity that can be achieved by the AVN. At even shorter A1A2 intervals, V1V2 (and H1H2) surprisingly begin to increase, because impulse propagation temporarily stops at a junctional location and is then re-initiated. Finally, at very short A1A2 values, a critical coupling interval is reached at which complete block of premature impulse propagation and, hence, loss of AV-nodal conduction occurs. The respective A1A2 interval is defined as the beginning of the effective refractory period of the AV conduction system (AVERP).

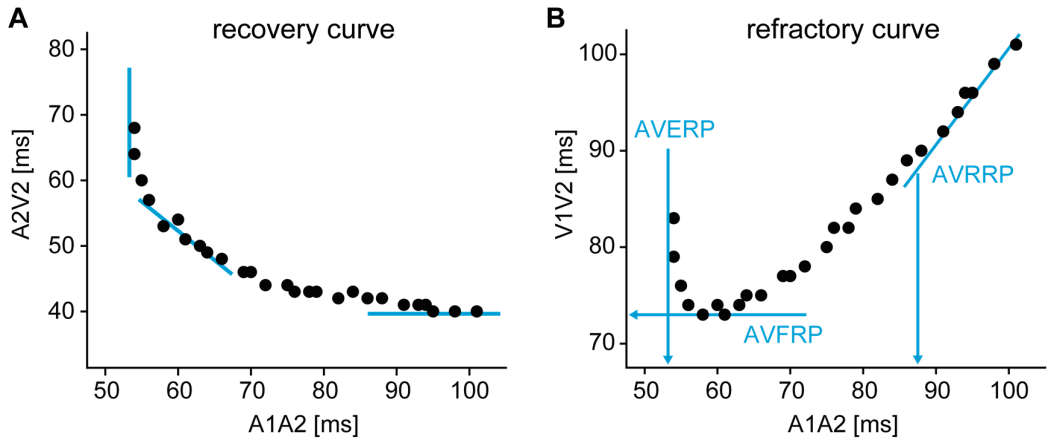

Figure 25. AV-nodal recovery and refractory curves. (A) AV-nodal recovery curves are derived from recordings using the premature stimulation protocol shown in Figure X. The curves are constructed by plotting A2V2 or A2H2 intervals against A1A2. **(B)** AV-nodal refractory curves are obtained by plotting V1V2 or H1H2 against A1A2. From these curves, the relative (AVRRP), functional (AVFRP), and effective refractory period (AVERP) of the AV conduction system can be determined. See text for further details. Figure is adapted from (Hennis et al., 2021c).

4.3.2.5 Wenckebach periodicity and 2:1 conduction

For further investigation of dromotropic function, the Wenckebach point and 2:1 conduction pattern are determined. For this purpose, short trains of eight stimuli are applied to the right atrium and the coupling interval S1S1 is reduced stepwise to 30 ms. During progressively decreasing coupling intervals, impulse propagation to the ventricles is gradually prolonged until block of AV conduction occurs. This means that one of the eight stimuli elicits an atrial response that is not conducted to the ventricles. The coupling interval at which AV block first occurs is defined as the antegrade Wenckebach point (WBP, Figure 26). After the skipped ventricular activation, the AV conduction interval resets and the cycle repeats.

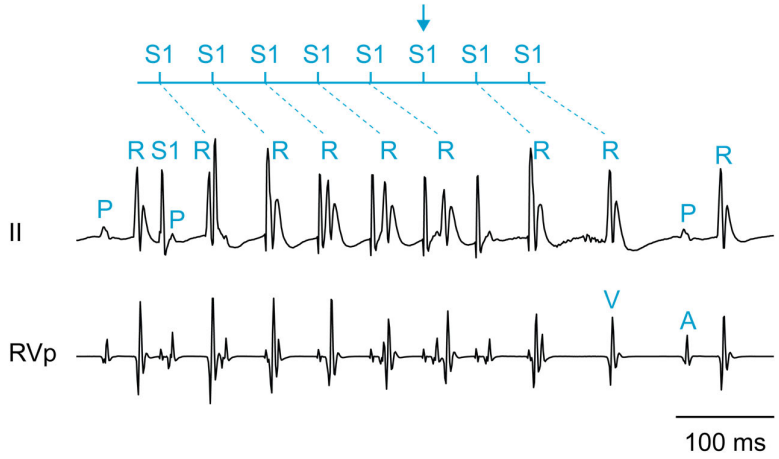

Figure 26. Wenckebach point (WBP). Stimulation protocol to determine the antegrade Wenckebach point. Timing of stimuli, surface ECG lead II and intracardiac lead RVp are displayed. WBP is defined as the S1S1 coupling interval at which AV block first occurs (indicated by blue arrow). Figure is adapted from (Hennis et al., 2021c).

Upon even shorter S1S1 intervals, more ventricular activations are skipped until only every second atrial response is propagated to the ventricles. The coupling interval at which 2:1 AV block first occurs is defined as the 2:1 cycle length (Figure 27). In diseased hearts with impaired atrioventricular conduction, these effects will occur earlier and values obtained for WBP and 2:1 cycle length will be increased.

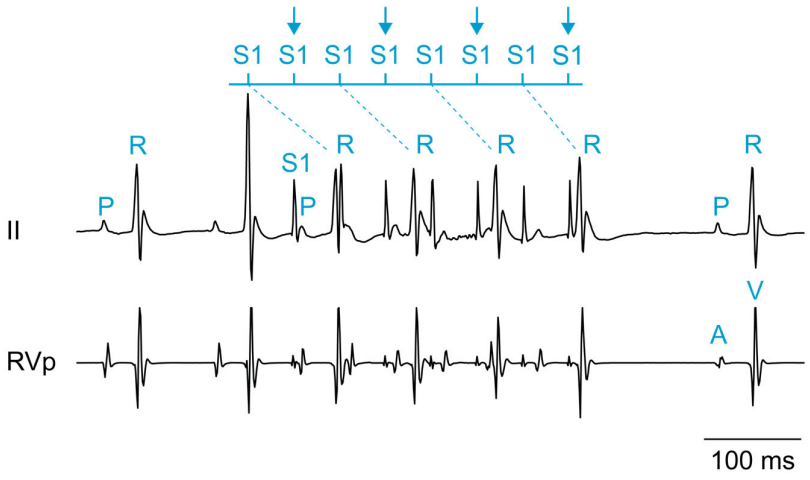

Figure 27. 2:1 conduction. Stimulation protocol to determine the 2:1 cycle length. Timing of stimuli, surface ECG lead II and intracardiac lead RVp are displayed. The 2:1 cycle length is defined as the S1S1 coupling interval at which 2:1 AV block first occurs (indicated by blue arrows). Figure is adapted from (Hennis et al., 2021c).

4.3.2.6 Ventricular effective refractory period (VERP)

In addition to assessing refractoriness of the AV conduction system, the effective refractory period of the ventricular myocardium (VERP) is typically determined during EPS. In analogy to measuring AV-nodal conduction properties, the protocol for VERP makes use of progressively premature stimulation of the right ventricle (Figure 28). For this purpose, a train of eight stimuli at a fixed pacing cycle length (S1S1) below the intrinsic sinus cycle length is applied to induce stabilization of refractoriness. The stimuli (S1) excite the ventricular myocardium (V1), followed by retrograde activation of the atria (A1). Subsequently, one extrastimulus (S2) is applied and the S1S2 coupling intervals are reduced stepwise to 30 ms. Below a critical S1S2 coupling interval, the extrastimuli S2 fail to induce ventricular responses due to refractoriness of the tissue. The coupling interval at which loss of ventricular activation first occurs is defined as the beginning of the ventricular effective refractory period (VERP).

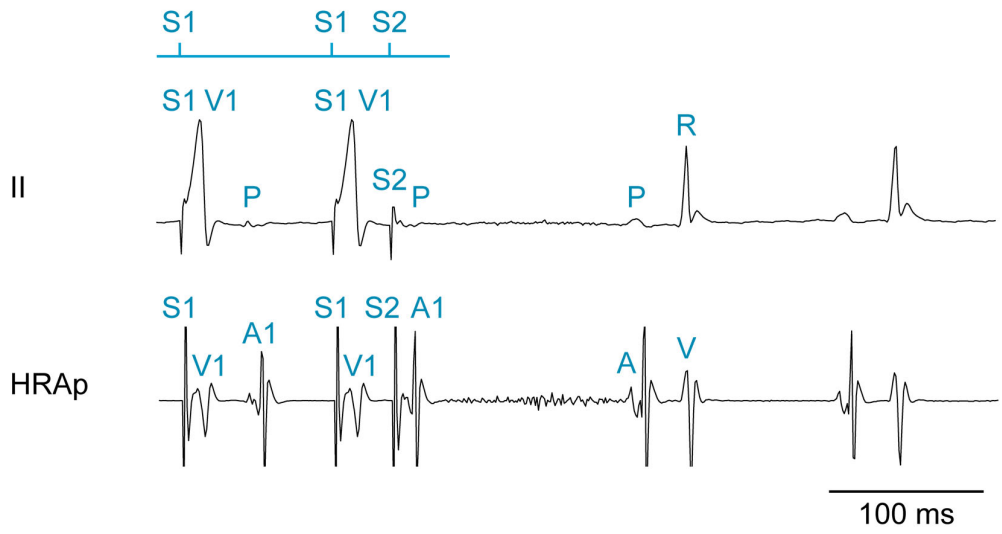

Figure 28. Ventricular effective refractory period (VERP). Stimulation protocol to determine VERP. Timing of stimuli, surface ECG lead II and intracardiac lead HRAp are displayed. Ventricular stimulation induces excitation of the ventricular myocardium, followed by retrograde atrial activation. Beginning of VERP is defined as the first (longest) S1S2 coupling interval at which loss of ventricular activation occurs. Figure is adapted from (Hennis et al., 2021c).

4.3.2.7 Atrial effective refractory period (AERP)

Furthermore, the effective refractory period of the atrial myocardium can be assessed. However, with an atrial stimulation protocol similar to VERP, a methodological problem occurs. At short S1S2 coupling intervals, the atrial signal generated by the premature stimulus S2 is buried in the ventricular complex originating from the last S1 stimulus and, thus, AERP cannot be reliably determined. To circumvent this problem, a specifically adapted three-step protocol is used (Figure 29). First, a train of eight atrial stimuli at a fixed pacing cycle length (S1S1) below the intrinsic sinus cycle length is applied. Second, an additional extrastimulus S2 at a coupling interval 5 ms below the previously determined AVERP is included (for details see chapter 4.3.2.4). This leads to AV conduction block of the atrial signal produced by S2 and, as a consequence, no ventricular complex is present to superimpose the next atrial activation. Third, a progressively premature extrastimulus S3 is applied and the beginning of the atrial effective refractory period (AERP) is defined as the first (longest) S2S3 coupling interval with loss of atrial response.

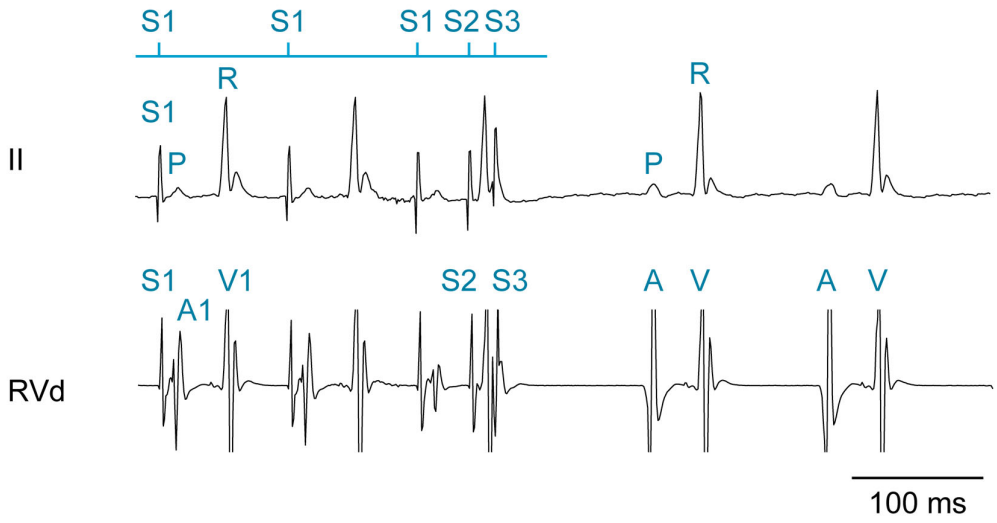

Figure 29. Atrial effective refractory period (AERP). Stimulation protocol to determine AERP. Timing of stimuli, surface ECG lead II and intracardiac lead RVd are displayed. The additional extrastimulus S2 is included to prevent superposition of atrial and ventricular signals at short coupling intervals. Beginning of AERP is defined as the first (longest) S2S3 coupling interval at which loss of atrial activation occurs. Figure is adapted from (Hennis et al., 2021c).

4.3.2.8 Susceptibility to atrial and ventricular arrhythmia

Finally, the EPS approach can be used to test vulnerability of the atrial and ventricular myocardium *in vivo*. To investigate susceptibility to atrial arrhythmia, the following atrial burst stimulation protocol was established (Westphal et al., 2013). A train of 100 stimuli is applied to the right atrium and the S1S1 coupling interval is reduced stepwise from 50 ms to 10 ms. This ensures that the S1S1 intervals reach values below the right atrial effective refractory period (AERP). With this stimulation protocol, episodes of atrial arrhythmia can be induced (Figure 30). To investigate susceptibility to ventricular arrhythmia, a modified ventricular burst stimulation protocol (Clasen et al., 2018) was established and validated in a mouse line with dysfunctional lysosomal Ca^{2+} signaling in cardiomyocytes (Figure 31). In this protocol, a train of 20 ventricular stimuli at a fixed pacing cycle length (S1S1) below the intrinsic sinus cycle length is applied, followed by a fast burst of eight ventricular extrastimuli (S2). The S2S2 coupling intervals are successively reduced and range from 50 ms to 20 ms. By use of these fast ventricular bursts, episodes of ventricular arrhythmia (Figure 31) can be triggered.

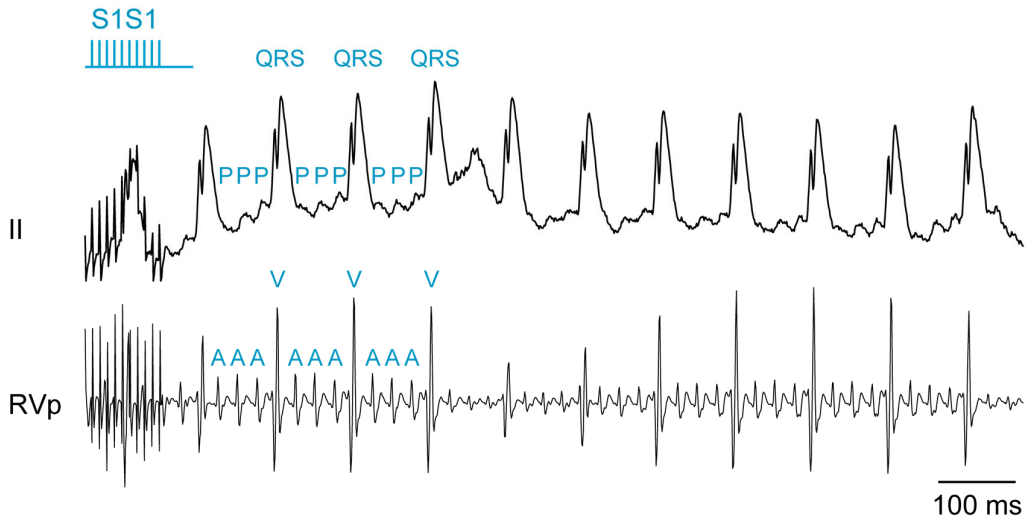

Figure 30. Atrial flutter induced by atrial burst stimulation. Stimulation protocol to test susceptibility to atrial arrhythmia. Timing of stimuli, surface ECG lead II and intracardiac lead RVp are displayed. Sustained atrial flutter was identified by a typical saw-tooth pattern of P waves in the surface ECG (upper trace) and a regular 3:1 AV-conduction pattern in the intracardiac ECG (lower trace). Atrial and ventricular intervals during atrial flutter were regular at cycle lengths of 26 ms and 104.3 ± 0.5 ms, respectively. Figure is adapted from (Hennis et al., 2021c).

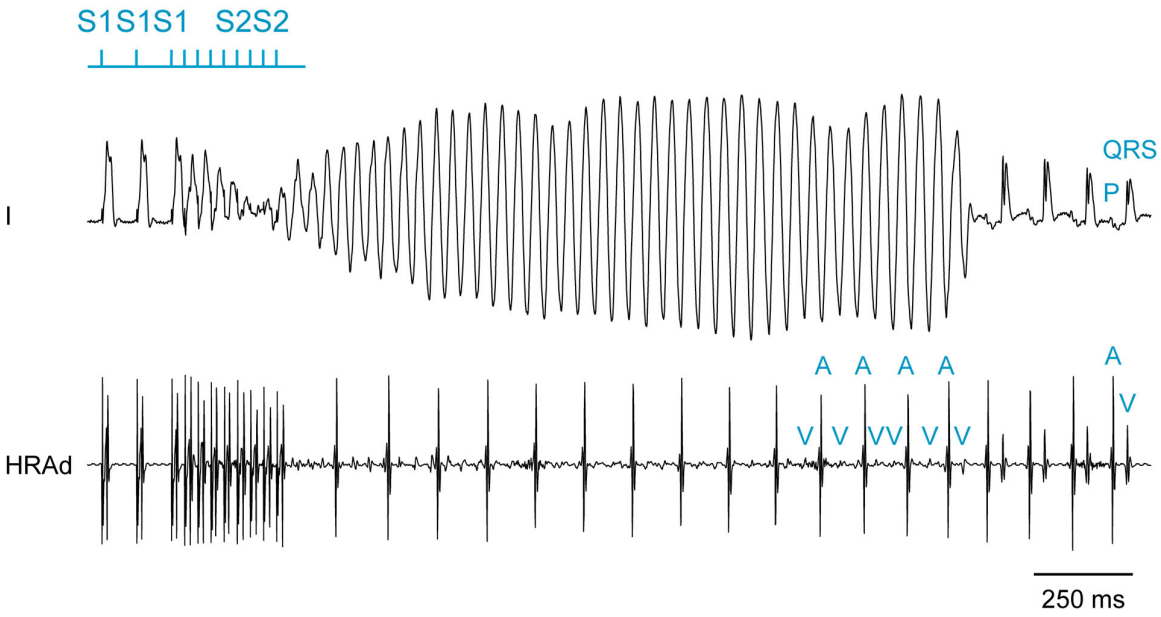

Figure 31. Nonsustained ventricular tachycardia (NSVT) induced by ventricular burst stimulation. Stimulation protocol to test vulnerability to ventricular arrhythmia. Timing of stimuli, surface ECG lead I and intracardiac lead HRAd are displayed. Ventricular burst pacing induced a 1.8 second run of NSVT that was spontaneously terminated, followed by return to baseline sinus rhythm. Figure is adapted from (Hennis et al., 2021c).

Taken together, the presented *in vivo* EPS approach is similar to that performed in humans and yields highly reliable results. It is specifically tailored to analyze preclinical mouse models and to elucidate mechanisms underlying disorders in cardiac impulse formation and propagation. In this study, *in vivo* EPS was used to investigate SAN and CCS function in HCN4FEA mice.

4.3.3 EPS in HCN4FEA mice

Up to this point, it was discovered that isolated SAN pacemaker cells can adopt a previously unknown nonfiring mode, during which spontaneous action potential firing is interrupted and the cells remain at hyperpolarized membrane potentials. The occurrence of nonfiring and the transition between the nonfiring and firing mode seem to be directly controlled by CDR of HCN4. Nonfiring pacemaker cells were also identified in the intact SAN tissue, where they appear to interact with neighboring cells in the firing mode. These interactions are predicted to have a functional impact on the activity of the whole SAN network. To investigate how loss of HCN4 CDR affects SAN and CCS function *in vivo*, the newly established EPS technique was carried out in intact living WT and HCN4FEA animals.

4.3.3.1 SAN function

In the first part of the experiment, the integrity and functionality of SAN automaticity was investigated by assessing sinus node recovery time (SNRT). The corresponding stimulation protocol was applied twice at pacing cycle lengths of 90 ms and 100 ms. Furthermore, rate-corrected sinus node recovery time (cSNRT) was calculated for both pacing cycle lengths. The results show that in HCN4FEA animals, SNRT is markedly prolonged as compared to WT mice (Figure 32). This clearly demonstrates that loss of HCN4 CDR leads to delayed impulse formation within the SAN *in vivo*.

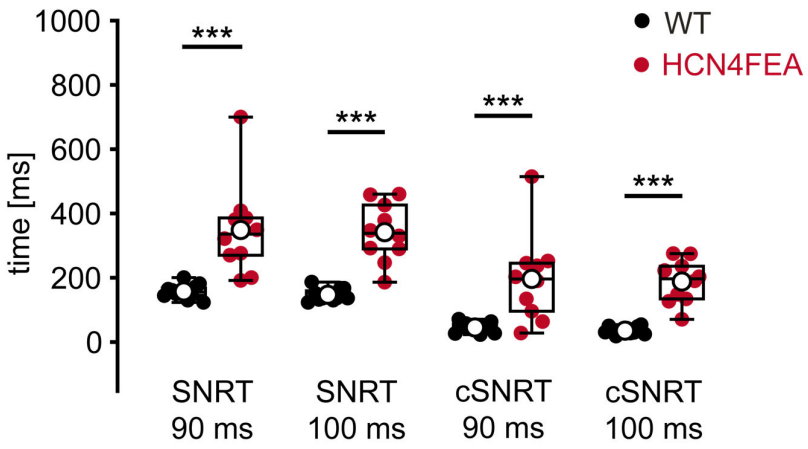

Figure 32. Sinus node recovery time (SNRT) is prolonged in HCN4FEA animals. Parameters for sinus node recovery time (SNRT) and rate-corrected sinus node recovery time (cSNRT) as determined during *in vivo* EPS at pacing cycle lengths of 90 ms and 100 ms. Increased values in HCN4FEA mice indicate that impulse formation in the SAN is delayed. Significance levels are determined with Sidakholm post-hoc test following two-way ANOVA for repeated measured (general linear model; *** $p < 0.001$).

Next, impulse propagation through the SAN tissue was investigated by determining sinoatrial conduction time (SACT) with the Strauss method (Figure 33). SACT was significantly prolonged in HCN4FEA mice, indicating that in addition to delayed impulse formation, impulse conduction from the central SAN to the surrounding atrial myocardium is impaired.

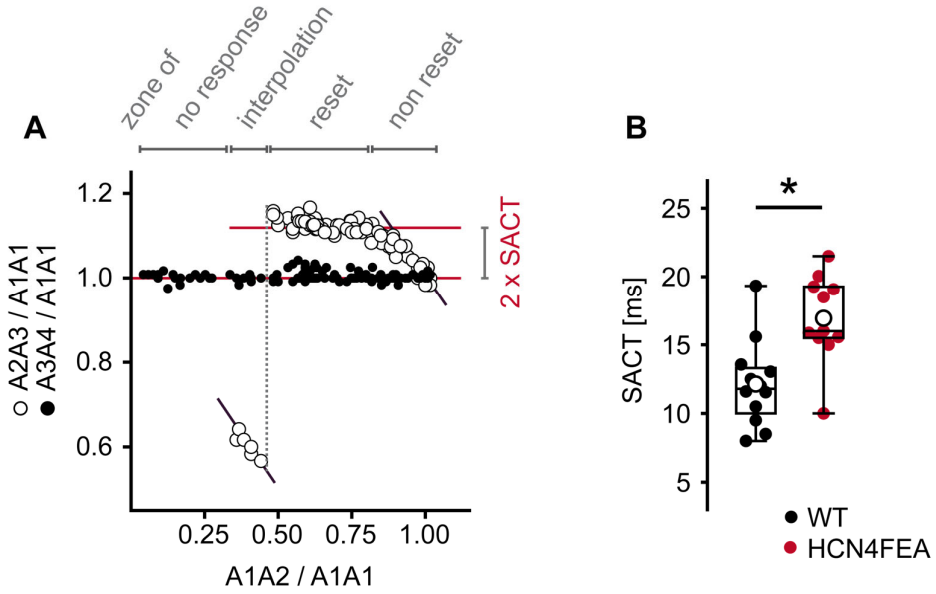

Figure 33. Sinoatrial conduction time (SACT) is prolonged in HCN4FEA animals. (A) Representative graph to determine sinoatrial conduction time (SACT) with the Strauss method. For details see chapter 4.3.2.2. **(B)** Quantification of SACT in WT and HCN4FEA mice. Loss of HCN4 CDR leads to increased values for SACT, indicating that velocity of impulse propagation through the SAN is reduced. Significance levels are determined with student´s paired t-test combined with Holm-Bonferroni correction for multiple comparisons (* $p < 0.05$).

Together, these results provide strong evidence that loss of HCN4 CDR leads to intrinsic SAN dysfunction *in vivo*. This finding is reflected by increases in SNRT and SACT, indicating delayed impulse formation within the SAN and prolonged impulse propagation through the nodal tissue, respectively.

4.3.3.2 AVN function

In the next step, possible effects of the HCN4FEA mutations on AV-nodal conduction properties were investigated by measuring AV-nodal recovery and refractory curves (Figure 34). In both WT and HCN4FEA animals the curves appeared normal and were similar between the two groups of mice.

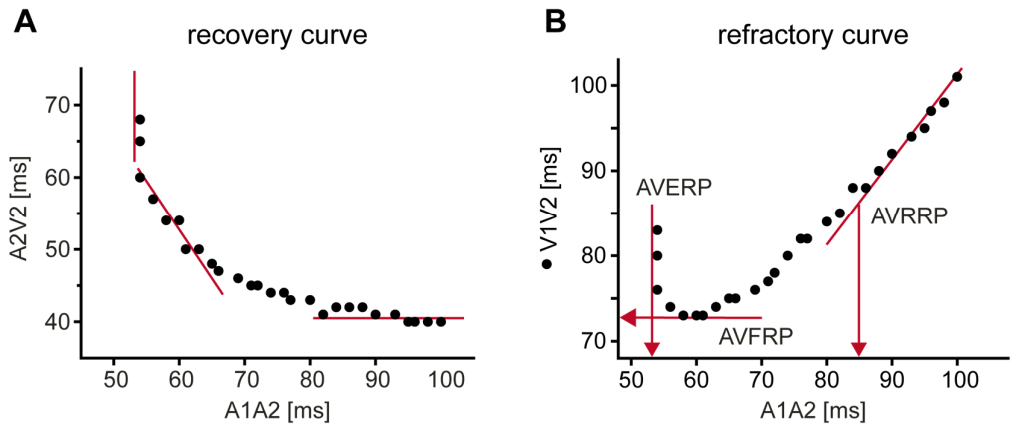

Figure 34. AV-nodal recovery curves and refractory curves. (A-B) Representative AV-nodal recovery curve (A) and refractory curve (B) derived from premature atrial stimulation during *in vivo* EPS in a WT mouse. The curves appeared normal in both WT and HCN4FEA mice and were similar between the two groups of animals. For details see chapter 4.3.2.4.

Subsequently, the refractory curves (Figure 34B) were analyzed as described in chapter 4.3.2.4 to obtain specific values for the relative (AVRRP), functional (AVFRP) and effective refractory period of the AV conduction system (AVERP). Quantification and statistical analysis revealed no differences in any of these parameters (Figure 35), indicating that despite loss of HCN4 CDR, AV-nodal conduction is normal in HCN4FEA mice.

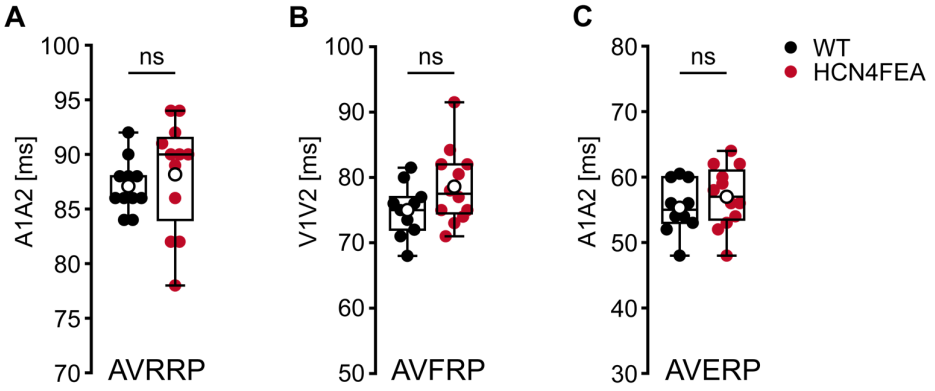

Figure 35. Relative (AVRRP), functional (AVFRP) and effective refractory period of the AV conduction system (AVERP) are similar in WT and HCN4FEA mice. (A-C) Values for AVRRP (A), AVFRP (B) and AVERP (C) were derived from premature atrial stimulation at a pacing cycle length of 100 ms. No statistically significant differences between WT and HCN4FEA mice were found in these parameters, indicating that AV-nodal refractoriness is not affected by loss of HCN4 CDR. For details see chapter 4.3.2.4. Significance levels are determined with student´s paired t-test combined with Holm-Bonferroni correction for multiple comparisons (ns, not significant: $p > 0.05$).

Furthermore, the antegrade Wenckebach point and 2:1 cycle length were assessed (Figure 36 A-B). Both parameters were similar between WT and HCN4FEA mice, further confirming that AVN function is not significantly affected by loss of HCN4 CDR.

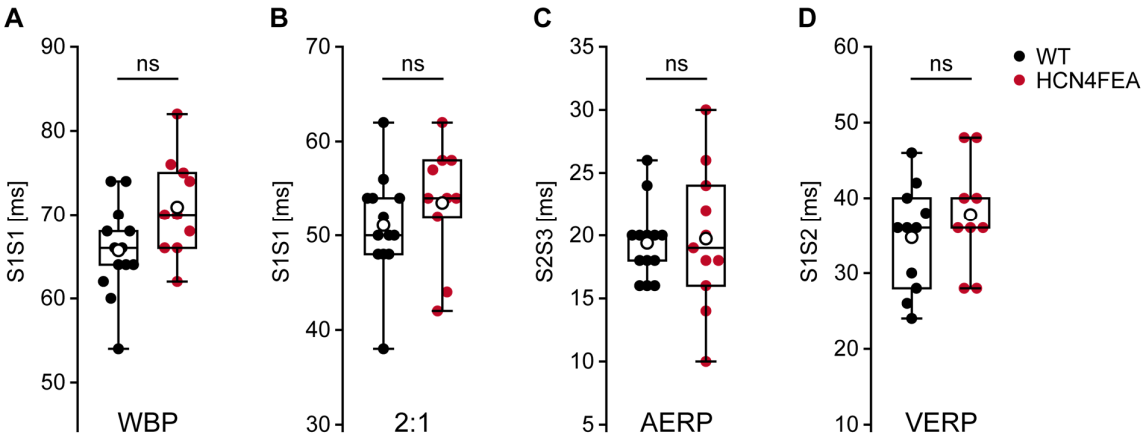

Figure 36. Wenckebach point (WBP), 2:1 cycle length (2:1), atrial effective refractory period (AERP), and ventricular effective refractory period (VERP) are unaltered in HCN4FEA mice. (A-B) The antegrade Wenckebach point (WBP) and 2:1 cycle length (2:1) were determined by premature atrial stimulation during *in vivo* EPS. For details see chapter 4.3.2.5. **(C)** The atrial effective refractory period (AERP) was derived using a modified three-step protocol. For details see chapter 4.3.2.7. **(D)** The ventricular effective refractory period (VERP) was determined by premature ventricular stimulation. For details see chapter 4.3.2.6. No statistically significant differences were found in any of these parameters, indicating that dromotropic function and excitability of the working myocardium is normal in HCN4FEA mice. Significance levels are determined with student´s paired t-test combined with Holm-Bonferroni correction for multiple comparisons (ns, not significant: $p > 0.05$).

4.3.3.3 Atrial and ventricular refractoriness

Finally, to exclude impairment of excitability in the working myocardium, the effective refractory period of the right atrium (AERP) and ventricle (VERP) were determined (Figure 36 C-D). Both parameters were similar in WT and HCN4FEA animals, indicating that refractoriness and, thus, excitability of both tissues remains unaffected by the mutations.

In summary, the results from *in vivo* EPS revealed that loss of HCN4 CDR leads to intrinsic SAN dysfunction characterized by delayed impulse formation and impaired impulse propagation through the nodal tissue. In contrast, AVN function is not affected, which is consistent with the fact that HCN4 expression is lower in the AVN than in the SAN (Baruscotti et al., 2011; Mesirca et al., 2014). This provides a plausible explanation for the finding that at least CDR of HCN4 does not play a major role in AV-nodal impulse conduction. Finally, refractoriness of the atrial and ventricular myocardium is unaltered, which excludes an impact on cardiac excitability downstream of the CCS.

5. Discussion

5.1 Discovery of the nonfiring activity mode in SAN pacemaker cells

In this study, the cAMP-insensitive HCN4FEA mouse model (Fenske et al., 2020) was used to investigate the role of HCN4 CDR in the cardiac pacemaker process. The main finding of the present study is the discovery of a novel nonfiring activity mode in isolated SAN cells. During nonfiring, the cells interrupt spontaneous electrical activity for up to one minute and remain at hyperpolarized membrane potentials, followed by recovery to regular action potential firing. The changing between firing and nonfiring occurs at a very long timescale. Therefore, this unexpected discovery was only possible by means of ultra-stable long-term perforated patch-clamp recordings, and in the context of the HCN4FEA mutant in which nonfiring is heavily exaggerated. Under baseline conditions, nonfiring was less frequently observed in WT cells. However, the nonfiring mode could be reliably induced by lowering intracellular cAMP concentrations via application of the cholinergic receptor agonist carbachol. Furthermore, the occurrence of nonfiring was drastically increased by incubating the cells with TAT-TRIP8b$_{nano}$, a membrane-permeable peptide that prevents cAMP-dependent activation of HCN channels (Saponaro et al., 2018). Application of the beta-adrenoceptor agonist isoproterenol, which leads to an increase in intracellular cAMP concentrations, completely abolished nonfiring in WT cells. This provides striking evidence for a critical role of HCN4 CDR in regulating the frequency of the nonfiring mode. It leads to the conclusion that cAMP-dependent activation of HCN4 is responsible for terminating nonfiring episodes and maintaining spontaneous action potential firing in SAN pacemaker cells.

5.2 Hysteresis of HCN4 causes the switch between firing and nonfiring

The molecular mechanism that causes the switch between firing and nonfiring can be explained by a biophysical phenomenon described as dynamic mode shifts or hysteresis behavior of HCN channels (Azene et al., 2005; Mannikko et al., 2005; Elinder et al., 2006; Zhao et al., 2009; Xiao et al., 2010; Fenske et al., 2020). It describes the fact that voltage-dependent activation of the channel is a dynamic and

history-dependent process, i.e., the position of the activation curve (current-voltage relationship) dynamically shifts as a function of the membrane potential (Figure 37). This can be observed as a left shift of the activation curve towards more negative voltages at depolarized membrane potentials, and as a right shift of the activation curve towards more positive voltages at hyperpolarized membrane potentials. A prerequisite for the validity of the following model is fulfilled by the slow activation and deactivation kinetics of HCN4 (Biel et al., 2002). Up to now, it was completely unclear how voltage-dependent gating of the channel could affect cardiac pacemaking, since the activation and deactivation time constants are 100-1000 times slower than the pacemaker cycle length. Consequently, HCN4 channel activity is barely influenced by the fast voltage changes during individual action potentials (APD90 = 50 – 80 ms) and is, thus, mainly dependent on the mean membrane potential. Accordingly, the HCN4-mediated I_f current can be considered nearly constant throughout the pacemaker cycle, which results in an almost time-independent, bidirectionally flowing background current during SAN action potentials (Peters et al., 2021). In the context of the slow changing between firing and nonfiring, however, the purpose of the slow gating kinetics and slow hysteresis becomes clear. The mean membrane potential of SAN pacemaker cells is more depolarized during firing and more hyperpolarized during nonfiring (blue line in Figure 37A). As a consequence of hysteresis behavior, the activation curve of HCN4 slowly shifts towards more negative voltages during firing (Figure 37B). Less channels become available, and the HCN4-mediated current becomes smaller which is reflected by progressive hyperpolarization. At a critical point, the shift of the activation curve is completed, and the cells switch into the nonfiring mode. The mean membrane potential abruptly drops to more hyperpolarized values and, consequently, the activation curve of HCN4 slowly shifts towards more positive voltages (Figure 37B). This is accompanied by slow recovery from the hyperpolarized potentials until the threshold for firing is reached. When the cells switch back to the firing mode, the mean membrane potential abruptly jumps to more depolarized values and the cycle repeats. In addition to hysteresis, CDR of HCN4 directly determines the position of the activation curve and, thus, regulates the time point at which the cells switch between the two activity modes. Due to lack of CDR in HCN4FEA cells, the activation curve cannot be shifted to sufficiently positive voltages, which leads to more frequently occurring and longer lasting episodes of nonfiring. The same consideration applies to reduced cAMP levels or acute inhibition of CDR in WT cells following application of carbachol or

TAT-TRIP8b$_{nano}$, respectively. In contrast, application of isoproterenol in WT cells leads to a pronounced shift of the activation curve towards more positive voltages, which completely abolishes the switch to the nonfiring mode.

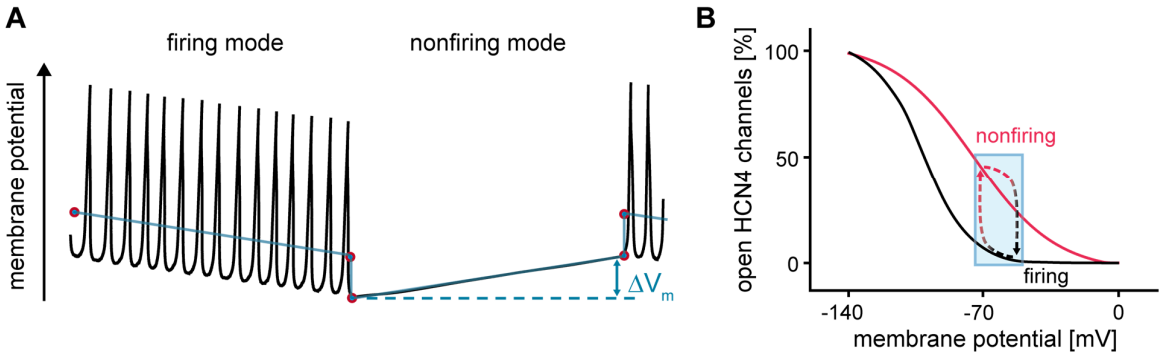

Figure 37. Hysteresis behavior of HCN4 causes the switch between firing and nonfiring. **(A)** Schematic illustration of a typical episode of firing and nonfiring in a SAN pacemaker cell. The blue line indicates the mean membrane potential. Note that at the end of firing, the mean membrane potential abruptly drops to more hyperpolarized values. Vice versa, at the end of nonfiring, the mean membrane potential abruptly jumps to more depolarized values. **(B)** Theoretical activation curves (current-voltage relationship) of HCN4 during firing (black line) and nonfiring (red line). Due to hysteresis behavior, the activation curve slowly shifts towards more hyperpolarized values during firing and towards more depolarized values during nonfiring. The blue box indicates the range of physiological membrane potentials. See text for details. Figure is adapted from (Fenske et al., 2020).

5.3 Concept of tonic entrainment in the SAN

In the intact SAN tissue, individual pacemaker cells are electrically coupled via gap junctions. Within this network, nonfiring pacemaker cells become apparent due to localized, subthreshold Ca^{2+} signals and lack of global intracellular Ca^{2+} transients. These Ca^{2+} signals were sometimes observed to be transmitted to neighboring cells, resulting in small cell clusters with irregular Ca^{2+} activity. The finding strongly suggests the presence of intercellular interactions between nonfiring cells and surrounding cells in the firing mode, which can be expected to have an impact on the overall SAN network activity. To answer the question how these long-lasting interactions occur, the following concept of tonic entrainment was proposed (Fenske et al., 2020). Pacemaker cells in the nonfiring mode are more hyperpolarized and will electrotonically draw flows of cations, including Ca^{2+}, from more depolarized neighboring cells in the firing mode

via gap junctions. This will slightly depolarize the nonfiring cells and hyperpolarize the firing cells to the same extent. When a new equilibrium is reached, the firing rate of the respective cell cluster will be decreased and, thus, a bradycardic network rhythm emerges (Figure 38). At the same time, the tonic cation flow will redistribute Ca^{2+} ions towards the nonfiring cells, which is the underlying cause for subthreshold Ca^{2+} activity. According to this new concept, nonfiring pacemaker cells can be considered a physiologically important, inhibitory component within the SAN network. Their influence on neighboring cells in the firing mode might be highly relevant to stabilize SAN network activity and to ensure proper function of the pacemaker process by suppressing overshooting excitation. Since tonic entrainment occurs between pacemaker cells within the SAN itself, it can be classified as a second component of the intrinsic entrainment process. In contrast to the fast effects of phasic entrainment, which occur at a beat-to-beat time scale, nonfiring episodes are considerably longer and, hence, induce long-lasting effects of tonic inhibition. However, the transition to nonfiring is also dependent on intracellular cAMP levels. In this way, ANS activity directly controls the extent of tonic inhibition by regulating the number of pacemaker cells in the nonfiring mode. Consequently, the tonic entrainment process also contributes significantly to neuronal entrainment in the SAN.

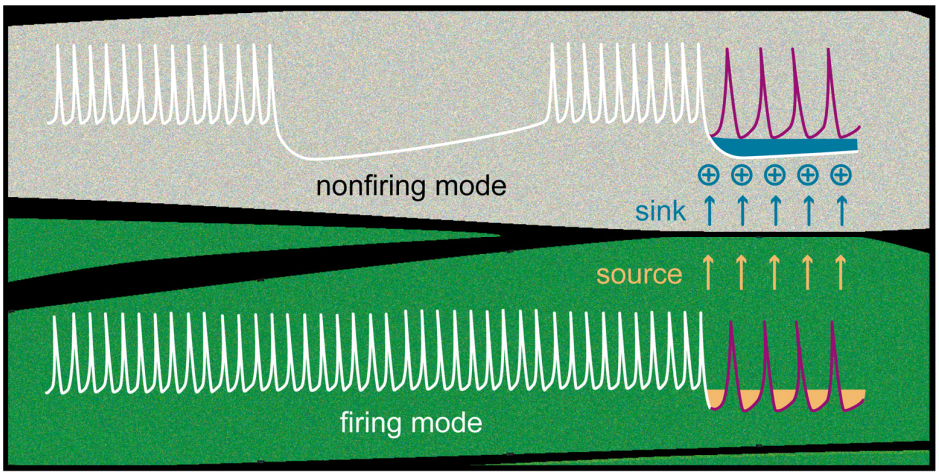

Figure 38. Tonic entrainment process in the SAN network. Schematic illustration of two pacemaker cells embedded in the SAN network. The cells are electrically coupled via gap junctions. The nonfiring cell (grey) is more hyperpolarized and acts as sink in the tonic entrainment process, whereas the firing cell (green) is more depolarized and acts as source. Due to the differences in membrane potential, a

tonic flow of cations (arrows) towards the nonfiring cell occurs, until a new equilibrium is reached. As a result, a bradycardic network rhythm emerges (purple). See text for details. Figure is adapted from (Fenske et al., 2020).

Under physiological conditions, a stable balance between inhibition (nonfiring cells) and excitation (firing cells) is controlled by CDR of HCN4. This fits well to the concept that inhibitory elements generally increase the stability of electrically active networks (Hennis et al., 2021a). Accordingly, it has been established that inhibitory interneurons are necessary to balance the activity of otherwise unstable neuronal networks in the brain (Markram et al., 2004; Sadeh and Clopath, 2021). In the context of nonfiring pacemaker cells, it is likely that such properties of neuronal networks are also attributable to the SAN, where inhibitory control of excitability may be equally essential to ensure a stable function of the pacemaker process. In the absence of HCN4 CDR, however, the precise balance between inhibition and excitation is lost. The resulting overactive inhibition leads to disruption of the pacemaker process and impairment of SAN network function.

5.4 Sinus node dysfunction and arrhythmias due to loss of HCN4 CDR

In the intact living animal, lack of HCN4 CDR manifests as intrinsic sinus node dysfunction. If too many cells enter the nonfiring mode, delayed impulse formation in the central SAN and prolonged impulse propagation from the SAN to the surrounding atrial myocardium occur. This results in chronotropic incompetence of the SAN, which is defined as the inability to reach the normal maximum firing rate. In contrast, AV-nodal conduction properties are unaffected and the general dromotropic function is normal, indicating that the AVN remains chronotropically competent. In line with these findings, *in vivo* telemetric ECG recordings have revealed that the overall cardiac phenotype of HCN4FEA mice includes pronounced bradycardia and chronotropic incompetence (Fenske et al., 2020). In-depth analysis of these ECG recordings uncovered severe sinus dysrhythmia and the presence of two distinct types of arrhythmias, namely isorhythmic AV dissociation (IAVD) and junctional escape rhythm (JER) (Figure 39). During IAVD, two independent pacemakers are synchronously active, i.e., the SAN activates the atria and a second, subsidiary pacemaker activates the ventricles independently from SAN function. As a consequence, atrial and

ventricular complexes dissociate from each other. However, the atrial and ventricular intervals remain isorhythmic, because the firing rates of the SAN and the subsidiary pacemaker are roughly equal (Figure 39A). During JER, the firing rate of the subsidiary pacemaker is faster than that of the SAN and, thus, effectively suppresses SAN function. As a result, the subsidiary pacemaker first activates the ventricles, followed by retrograde activation of the atria (Figure 39B).

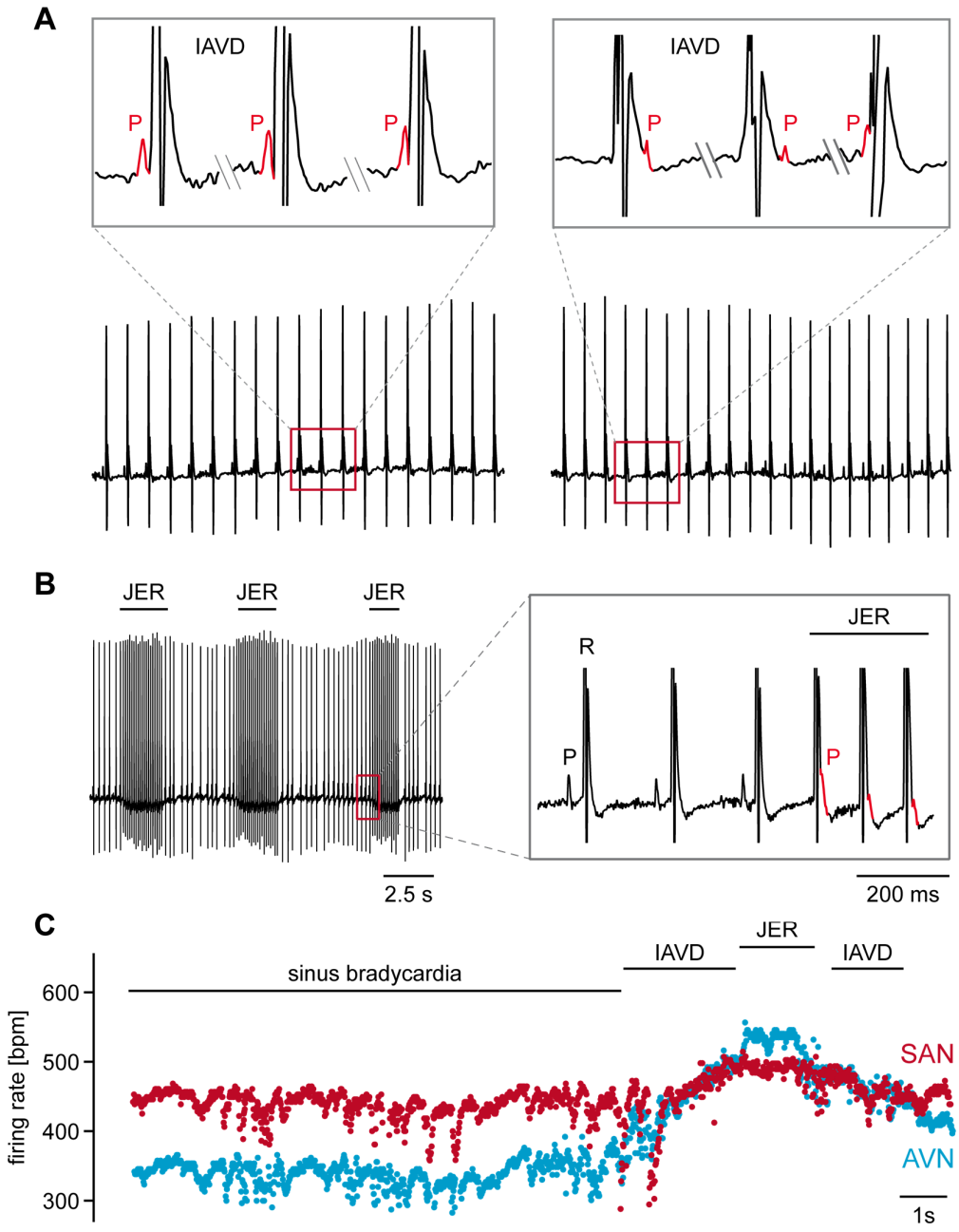

Figure 39. Isorhythmic AV dissociation (IAVD) and junctional escape rhythm (JER) in HCN4FEA mice. (A) Telemetric ECG recordings from HCN4FEA mice highlighting episodes of Isorhythmic AV dissociation (IAVD). The SAN activates the atria and the AVN independently activates the ventricles. Consequently, the atrial and ventricular complexes dissociate from each other, while atrial and ventricular intervals remain Isorhythmic. This gives rise to the characteristic flirtatious P waves (upper panels). **(B)** ECG recording during episodes of junctional escape rhythm (JER). The AVN suppresses SAN function and first activates the ventricles, followed by retrograde activation of the atria. As a result, the P waves occur behind the QRS complexes (right panel). **(C)** SAN firing rate and putative AVN firing rate to illustrate chronotropic incompetence of the SAN combined with chronotropic competence of the AVN. Upon activation of the sympathetic nervous system, the SAN firing rate cannot be sufficiently increased, whereas the AVN firing rate is increased normally. When the AVN firing rate roughly equals that of the SAN, IAVD occurs. When the AVN firing rate exceeds that of the SAN, JER occurs. Figure is adapted from (Fenske et al., 2020).

In HCN4FEA mice, both arrhythmias are spontaneously induced during HR acceleration following activation of the sympathetic nervous system (SNS). Their occurrence is attributable to the fact that the coordinated activity of the SAN and AVN is disturbed. Upon SNS activation, the firing rate of the SAN cannot be sufficiently increased due to chronotropic incompetence. In contrast, the AVN is chronotropically competent and its firing rate can be increased normally. IAVD occurs when the AVN firing rate is accelerated and approximately matches that of the SAN. JER occurs when the AVN firing rate exceeds that of the SAN and fully suppresses SAN activity (Figure 39C) (Fenske et al., 2020).

5.5 Inappropriate HR decreases during vagal activity

Lack of HCN4 CDR also leads to overshooting HR responses during activation of the parasympathetic nervous system, giving rise to severely enhanced HR decreases. This has been demonstrated in combined telemetric ECG and blood pressure recordings (Fenske et al., 2020). In HCN4FEA mice, vagal activity shifts too many cells into the nonfiring mode, which inappropriately increases the level of inhibition and, thus, disturbs the balance between excitation and inhibition in the SAN network. This leads to an overshooting drop in HR and, as a result, severe sinus bradycardia and sinus pauses occur. CDR of HCN4 effectively counteracts this effect and can thereby dampen the HR-lowering influences of the parasympathetic nervous system.

Taken together, the major role of HCN4 CDR is to protect the SAN network from potentially harmful influences by the ANS. Loss of HCN4 CDR leads to overshooting HR responses reflected by escape arrhythmias and bradycardia, which are caused by intrinsically impaired responsiveness of the SAN to ANS activity (Fenske et al., 2020).

5.6 CDR of HCN4 is not required to mediate the classical chronotropic effect

The second major finding of the present study is that CDR of HCN4 does not represent the main subcellular mechanism to mediate the classical chronotropic effect as proposed by DiFrancesco and others (Brown et al., 1979; DiFrancesco et al., 1986; DiFrancesco and Tortora, 1991; DiFrancesco, 1993). This can be concluded from long-term action potential recordings of isolated SAN cells, which revealed no differences between WT and HCN4FEA cells in baseline firing rates, as well as a similar increase and reduction in the firing rate upon application of isoproterenol and carbachol, respectively. These findings are in line with the results from telemetric ECG recordings in conscious animals (Fenske et al., 2020). While ECG recordings from HCN4FEA mice uncovered severe bradycardia, the HR regulation dynamics (HR_{max}/HR_{min}) and full HR range (HR_{max}-HR_{min}) are completely preserved (Figure 40). This indicates that acceleration and deceleration of HR following ANS activity are mainly driven by ion channels and transporters other than HCN4. However, CDR of HCN4 is crucial for determining absolute HR values and preventing bradycardia. If CDR is missing, too many cells switch into the nonfiring mode and impulse formation and conduction in the SAN are slowed down. Consequently, the average HR and full HR range shift towards lower HR values, and intrinsic bradycardia arises. Taken together, CDR of HCN4 plays an important role in setting the intrinsic HR, while it is not required for changing HR *per se*.

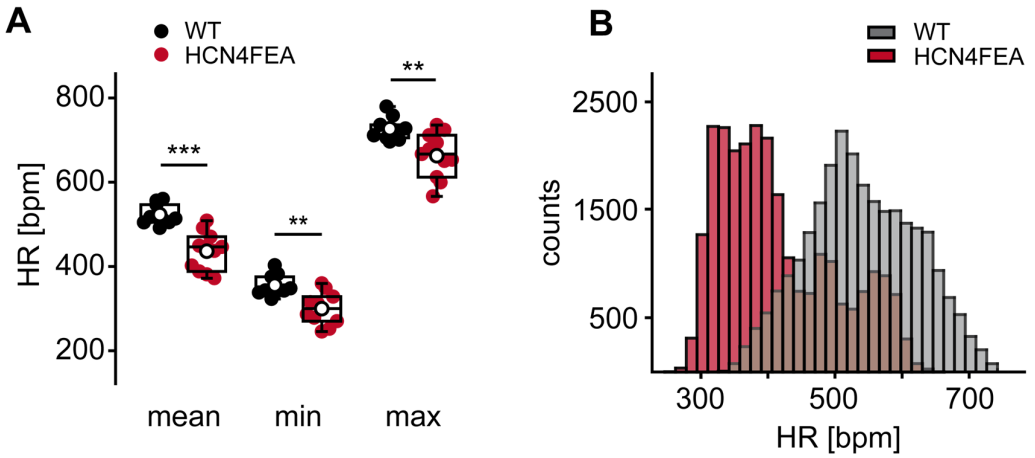

Figure 40. Bradycardia with preserved HR regulation in HCN4FEA mice. (A) Parameters for mean, minimum and maximum HR determined from 72 h telemetric ECG recordings in WT and HCN4FEA mice. Absolute values are lower in HCN4FEA mice, whereas HR regulation dynamics (HR_{max}/HR_{min}) and HR range (HR_{max}-HR_{min}) are completely preserved. This provides further evidence that CDR of HCN4 is not required to mediate the classical chronotropic effect. **(B)** Representative HR histograms of a WT and HCN4FEA mouse derived from 72 h telemetric ECG recordings. Histograms of HCN4FEA mice are shifted towards lower values, demonstrating severe intrinsic bradycardia. Figure is adapted from (Fenske et al., 2020).

Previous animal studies investigating the role of HCN4 in the heart, however, led to conflicting and partially contradictory conclusions (Hennis et al., 2021b). In 2003, the first HCN4 knockout mouse model was created (Stieber et al., 2003). Interestingly, this study revealed that global HCN4-deficiency causes embryonic lethality, which is attributable to a severely diminished I_f current during cardiac development. The authors reported that in embryonic $HCN4^{-/-}$ hearts, HR is strongly reduced by approximately 40%. Furthermore, HR as well as action potential firing rate in isolated embryonic $HCN4^{-/-}$ cardiomyocytes cannot be increased by cAMP. Similar results were obtained in a different study investigating a mouse model with only a single amino acid exchange (R669Q) in the HCN4 CNBD (Harzheim et al., 2008). This mutation abolishes CDR of HCN4, while leaving all other functional properties unaffected. Most importantly, also HCN4 R669Q mice are embryonically lethal, which strongly suggests that basal cAMP-dependent activation of HCN4 is a general prerequisite for the physiological function of the channel, and that preventing CDR alone has similar functional effects to completely knocking out HCN4. The main findings from this study include that

embryonic HCN4 R669Q hearts display significantly reduced HRs and abolished responsiveness to catecholaminergic stimulation. Together, these studies support the classical theory that CDR of HCN4 is responsible for mediating the chronotropic effect. However, the conclusions that can be drawn from these results are limited, since in embryonic hearts the SAN and CCS are not yet completely developed.

To enable investigation of adult animals lacking HCN4, several inducible, global (Herrmann et al., 2007) or cardiac-specific (Hoesl et al., 2008; Baruscotti et al., 2011) HCN4 knockout mouse models were created. In contrast to the findings from embryonic hearts, the chronotropic effect, as determined by responsiveness to beta-adrenergic stimulation, was fully preserved in all of these mouse models. A further study, in which a transgenic approach was used to achieve cardiac-specific silencing of I_f (hHCN4-AYA mice), confirmed these results (Mesirca et al., 2014). In addition, the majority of the studies reported severe bradycardia and sinus dysrhythmia, suggesting that absence of HCN4 gives rise to intrinsically reduced HRs and overshooting parasympathetic responses (Baruscotti et al., 2011; Mesirca et al., 2014). To further study the contribution of HCN4 to autonomic HR regulation, Kozasa et al. created a transgenic mouse model with inducible, global overexpression or knockdown of HCN4 (Kozasa et al., 2018). Interestingly, HCN4 overexpression did not induce tachycardia, but reduced heart rate variability and attenuated HR-lowering responses to cervical vagus nerve stimulation *in vivo*. In contrast, conditional knockdown of HCN4 led to pronounced bradycardia and overshooting responses to vagus nerve stimulation. HR responses to beta-adrenergic stimulation, however, were not altered in both groups of mice. To investigate the role of HCN4 CDR more directly, a further transgenic mouse model was created (Alig et al., 2009). These mice are characterized by cardiac-specific expression of a mutant construct (hHCN4-573X), which is based on a mutation originally identified in a human patient with idiopathic sinus node dysfunction (Schulze-Bahr et al., 2003). The mutation leads to a large C-terminal truncation that includes the CNBD of HCN4 and, thus, suppresses cAMP-sensitivity of the channel in a dominant-negative manner. Also in these mice, the authors reported a significant reduction in HR at rest and during exercise, whereas the relative range of HR regulation was preserved. However, the observations cannot be attributed to loss of HCN4 CDR alone, since the truncation of the C-terminus exceeds the region of the CNBD by far. As a consequence, it is reasonable to assume that the truncated HCN4 channels not only lose cAMP sensitivity, but also lack other regulatory domains including binding sites for

intracellular channel modulators (e.g., kinases or cytoskeletal proteins). Therefore, the possibility cannot be excluded that absence of other mechanisms to modulate HCN4 activity is responsible for the cardiac phenotype of these mice.

In addition to animal studies, several human studies investigating HCN4 channelopathies (Verkerk and Wilders, 2014; 2015) have shown that the mutations reported in the respective studies result in loss of HCN4 function and lead to heterogeneous cardiac syndromes, most of them including bradycardia. However, in the majority of these channelopathies the chronotropic response to beta-adrenergic stimulation is preserved. While this argues against the classical theory of the chronotropic effect, a direct interpretation of these cardiac symptoms on HCN4 function is not possible, since all human patients identified so far carry heterozygous mutations and, thus, also express a non-mutated HCN4 copy.

Taken together, the main findings from the present study lead to the conclusion that CDR of HCN4 is responsible for setting the intrinsic HR and protecting the SAN network from destabilizing ANS input. This is achieved by regulating the number of pacemaker cells in the nonfiring mode, thereby creating a stable balance between excitation and inhibition in the SAN. In contrast, CDR of HCN4 is not required for changing HR *per se*. This is contradictory to the classical theory of the chronotropic effect, and to previous studies investigating HCN4-deficient embryonic hearts. These studies supported the concept that CDR of HCN4 is the main subcellular mechanism in the SAN to mediate HR regulation by the ANS (Stieber et al., 2003; Harzheim et al., 2008). However, the present findings are well consistent with the results from previously published studies on adult mice with absent or dysfunctional HCN4 channels (Herrmann et al., 2007; Hoesl et al., 2008; Alig et al., 2009; Baruscotti et al., 2011; Mesirca et al., 2014; Kozasa et al., 2018). The majority of these studies reports bradycardia and severe sinus dysrhythmia, whereas HR regulation by the ANS is not significantly affected. Furthermore, the results of the present study are in line with human studies on HCN4 channelopathies (Verkerk and Wilders, 2014; 2015). The respective mutations result in loss of HCN4 function and the patients display heterogeneous cardiac symptoms, including bradycardia, while the chronotropic response to beta-adrenergic stimulation is mostly preserved.

5.7 Alternative mechanisms to mediate HR regulation by the ANS

As discussed above, evidence is increasing that CDR of HCN4 is not the main mechanism in SAN pacemaker cells to mediate the chronotropic effect. This leads to the conclusion that acceleration and deceleration of HR following ANS activity are mainly driven by ion channels and/or transporters other than HCN4. Consequently, the question arises as to which molecular component of the SAN pacemaker process actually mediates HR regulation by the ANS (Hennis et al., 2021b). Since several proteins associated with the *membrane clock* and *calcium clock* are targeted and modulated by ANS activity, there are various potential candidates to possibly mediate the chronotropic effect on the subcellular level (Figure 41).

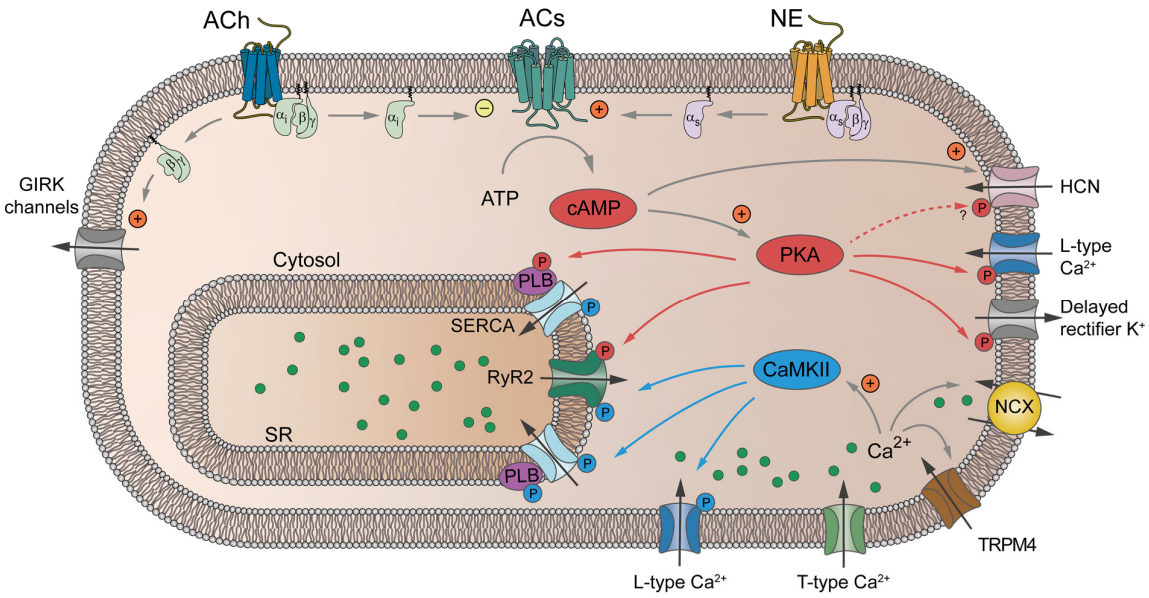

Figure 41. Signal transduction pathways in SAN pacemaker cells. Gs protein-coupled receptors are activated by norepinephrine (NE) released from sympathetic nerve terminals. Subsequent Gαs signaling stimulates adenylyl cyclases (ACs) to synthetize cAMP from ATP. Increasing intracellular cAMP levels directly activate HCN channels and stimulate protein kinase A (PKA), which in turn phosphorylates and activates several target proteins (highlighted by red arrows and red circles). Moreover, activation of the sympathetic nervous system leads to an increase in the intracellular Ca^{2+} concentration, thereby increasing the activity of the sodium calcium exchanger (NCX), transient receptor potential melastatin 4 channel (TRPM4), and Ca^{2+}/calmodulin-dependent kinase II (CaMKII). Various target proteins are phosphorylated and activated by CaMKII (indicated by blue arrows and blue circles). Altogether, this

increases the rate of SDD and rate of membrane repolarization, leading to acceleration of the action potential frequency (see text for details). Conversely, Gi protein-coupled receptors are activated by acetylcholine (ACh) released from vagal nerve terminals. Gαi signaling inhibits ACs and, thus, induces the opposite effects. Moreover, the β/γ-subunit activates G protein-coupled inwardly-rectifying potassium channels (GIRK), thereby shifting the MDP to more hyperpolarized values and additionally slowing down the firing rate. Abbreviations: ACh, acetylcholine; ACs, adenylyl cyclases; ATP, adenosine triphosphate; CaMKII, Ca^{2+}/calmodulin-dependent kinase II; GIRK, G protein-coupled inwardly rectifying potassium channel; HCN, hyperpolarization-activated cyclic nucleotide-gated channel; NE, norepinephrine; PKA, protein kinase A; PLB, phospholamban; RyR2, ryanodine receptor 2; SERCA, sarco-/endoplasmic reticulum Ca^{2+} ATPase; SR, sarcoplasmic reticulum; TRPM4, transient receptor potential melastatin 4 channel. Figure is adapted from (Hennis et al., 2021b).

Upon release of norepinephrine (NE) from sympathetic nerve terminals, the stimulating adenylyl cyclase−cAMP−protein kinase A cascade is activated. Increasing activity of protein kinase A (PKA) leads to phosphorylation and activation of various target proteins that have been shown to be involved in pacemaker activity (MacDonald et al., 2020). Among them are L-type Ca^{2+} channels (van der Heyden et al., 2005), phospholamban (Vinogradova et al., 2010), ryanodine receptors (Shan et al., 2010), delayed rectifier potassium channels (Lei et al., 2000), and HCN channels (Liao et al., 2010). Furthermore, it is known that sympathetic activity stimulates Ca^{2+}/calmodulin-dependent kinase II (CaMKII) (Wu et al., 2009; Grimm and Brown, 2010; Wu and Anderson, 2014), which shares several downstream targets with PKA such as L-type Ca^{2+} channels (Vinogradova et al., 2000), phospholamban, and ryanodine receptor 2 (Li et al., 2016).

In the past, many of these ANS targets have been extensively studied to identify a potential contribution to mediating the chronotropic effect. Investigation of voltage-gated Ca^{2+} channels has revealed that $I_{Ca,L}$ is enhanced by PKA-dependent (van der Heyden et al., 2005; Mangoni and Nargeot, 2008) and CaMKII-dependent phosphorylation (Dzhura et al., 2000; Vinogradova et al., 2000; Mangoni and Nargeot, 2008). Accordingly, experiments with $Ca_V1.3$ knockout mice demonstrated slower firing rates and a reduced slope of SDD in isolated SAN pacemaker cells (Mangoni et al., 2003; Baudot et al., 2020). However, augmentation of $I_{Ca,L}$ alone seems not to be sufficient to induce a physiological increase in action potential firing rate following beta-adrenergic stimulation (Vinogradova et al., 2002; Lakatta et al., 2010). Furthermore, a potential isoproterenol-induced effect on $I_{Ca,T}$ in the SAN is not yet completely resolved

(Hagiwara et al., 1988; Li et al., 2012). Another hypothesis assumes that modulation of the *calcium clock* is responsible for HR regulation by the ANS. This concept is based on two different effects induced by activation of PKA and CaMKII. First, Ca^{2+} reuptake into the SR will be accelerated due to CaMKII-dependent phosphorylation of the sarco-/endoplasmic reticulum ATPase (SERCA) (Narayanan and Xu, 1997) and/or PKA/CaMKII-dependent phosphorylation of phospholamban (Vinogradova et al., 2010; Li et al., 2016), which leads to disinhibition of SERCA. Second, local Ca^{2+} releases (LCRs) from the SR will be increased by PKA/CaMKII-dependent phosphorylation of ryanodine receptor 2 (RyR2) (Vinogradova et al., 2002; Bers, 2006; Shan et al., 2010). Accordingly, LCRs will be enhanced and will occur at earlier time points in the pacemaker cycle, leading to elevated intracellular Ca^{2+} levels during diastole. This will activate the transmembrane sodium calcium exchanger (NCX) and increase the depolarizing I_{NCX} current, which ultimately accelerates SDD and increases the firing frequency (Bogdanov et al., 2006; Maltsev and Lakatta, 2009; Lakatta et al., 2010).

There are several independent studies that support this theory (Hennis et al., 2021b). Accordingly, FRET experiments have demonstrated that PKA activity in isolated SAN pacemaker cells is directly connected to adaption of the firing rate following adrenergic or cholinergic stimulation (Behar et al., 2016). Furthermore, increased PKA activity by beta-adrenergic stimulation leads to enhanced LCRs, whereas inhibition of PKA diminishes LCRs and significantly interferes with spontaneous action potential firing (Vinogradova et al., 2006). In addition to PKA-dependent effects, it has been shown that CaMKII activity is crucial to induce a physiological HR increase via augmentation of LCRs (Wu et al., 2009; Swaminathan et al., 2011). Moreover, it has been indicated that the rate of Ca^{2+} reuptake into the SR during diastole directly influences the chronotropic state of the SAN. Accordingly, pharmacological inhibition of SERCA prolongs the pacemaker cycle length in isolated SAN cells, while PKA/CaMKII-dependent phosphorylation of phospholamban reduces the LCR period and pacemaker cycle length by disinhibition of SERCA (Vinogradova et al., 2010; Li et al., 2016). Furthermore, there is evidence that modulation of RyR2 activity is crucial for physiological HR regulation (Vinogradova et al., 2006; Eschenhagen, 2010; Shan et al., 2010). This has been shown by direct pharmacological inhibition of RyRs as well as by genetic inhibition of PKA-dependent RyR2 phosphorylation. Both interventions lead to diminished augmentation of I_{NCX}, reduced acceleration of SDD and blunted increases in firing rate after beta-adrenergic stimulation of SAN pacemaker cells (Rigg

et al., 2000; Lakatta et al., 2010; Shan et al., 2010). Finally, investigation of NCX function has revealed a fundamental role in SAN pacemaking and significant contribution to positive chronotropic modulation (Zhou and Lipsius, 1993; Bogdanov et al., 2001; Bogdanov et al., 2006). Mathematical I_{NCX} and Ca^{2+} dynamics model simulations, as well as experiments with NCX knockout mice have demonstrated that loss of NCX function leads to decreased or completely abolished responsiveness of the SAN to isoproterenol stimulation (Bogdanov et al., 2006; Gao et al., 2013; Maltsev et al., 2013). In addition to effects on NCX activity, elevated intracellular Ca^{2+} levels in the SAN can also activate the transient receptor potential melastatin 4 channel (TRPM4), which has been shown to contribute to membrane depolarization at negative potentials (Hof et al., 2013; Guinamard et al., 2015). However, pharmacological blockade of TRPM4 by 9-phenanthrol and investigation of $TRPM4^{-/-}$ mice revealed that relevant HR-lowering effects occur only at already low initial heart rates.

In conclusion, there are numerous redundant processes involved in this cascade, that have all been shown to be important for HR modulation when studied individually. However, it is well possible that some of these processes represent backup mechanisms with the purpose to maintain proper chronotropic responses if one or several other components should fail. Therefore, the main subcellular mechanism in SAN pacemaker cells to mediate HR regulation by the ANS remains yet to be identified.

6. Summary

Since the 1980s, it has been postulated that CDR of HCN4 is responsible for mediating the chronotropic effect. However, this classical theory did not remain without controversy and over the past 20 years, several animal studies have led to conflicting conclusions about the functional significance of HCN4 CDR in the SAN. The present study was designed to experimentally review this classical concept by making use of the novel, cAMP-insensitive HCN4FEA mouse line.

The main finding of this study is the unexpected discovery of a previously unknown nonfiring activity mode in SAN pacemaker cells. The frequency of the nonfiring mode is directly controlled by CDR of HCN4. Nonfiring pacemaker cells were also identified in the intact SAN network, where they have an impact on overall SAN activity via the tonic entrainment process. Through these interactions, nonfiring cells form a physiologically important, inhibitory component within the SAN. CDR of HCN4 controls the number of pacemaker cells in the nonfiring mode and thereby creates a stable balance between inhibition and excitation at the network level. *In vivo*, this balance is crucial for normal SAN function and contributes to determining the intrinsic HR. Absence of HCN4 CDR gives rise to significant SAN dysfunction, characterized by delayed impulse formation in the central SAN and impaired impulse propagation to the surrounding atrial myocardium. Therefore, intact CDR is essential to maintain a robust SAN pacemaker process, which is required to counteract bradycardia and overshooting HR responses to ANS activity. Conversely, CDR is not involved in ANS-induced HR changes, since in the HCN4FEA mutant the general chronotropic responses to adrenergic and cholinergic stimulation are preserved.

In conclusion, CDR of HCN4 is responsible for setting the intrinsic HR and for protecting the SAN network from potentially harmful ANS input. In contrast, it is not required for changing HR *per se*. This provides new evidence against a major role of HCN4 CDR in mediating the classical chronotropic effect and defines a novel concept for HCN4 function in the central SAN pacemaker process.

7. References

Alig, J., Marger, L., Mesirca, P., Ehmke, H., Mangoni, M.E., and Isbrandt, D. (2009). Control of heart rate by cAMP sensitivity of HCN channels. *Proc Natl Acad Sci U S A* 106**,** 12189-12194, doi: 10.1073/pnas.0810332106.

Ashcroft, F.M., and Rorsman, P. (2013). K(ATP) channels and islet hormone secretion: new insights and controversies. *Nat Rev Endocrinol* 9**,** 660-669, doi: 10.1038/nrendo.2013.166.

Azene, E.M., Xue, T., Marban, E., Tomaselli, G.F., and Li, R.A. (2005). Non-equilibrium behavior of HCN channels: insights into the role of HCN channels in native and engineered pacemakers. *Cardiovasc Res* 67**,** 263-273, doi: 10.1016/j.cardiores.2005.03.006.

Baruscotti, M., Bucchi, A., Viscomi, C., Mandelli, G., Consalez, G., Gnecchi-Rusconi, T., Montano, N., Casali, K.R., Micheloni, S., Barbuti, A., and Difrancesco, D. (2011). Deep bradycardia and heart block caused by inducible cardiac-specific knockout of the pacemaker channel gene Hcn4. *Proc Natl Acad Sci U S A* 108**,** 1705-1710, doi: 10.1073/pnas.1010122108.

Baudot, M., Torre, E., Bidaud, I., Louradour, J., Torrente, A.G., Fossier, L., Talssi, L., Nargeot, J., Barrere-Lemaire, S., Mesirca, P., and Mangoni, M.E. (2020). Concomitant genetic ablation of L-type Cav1.3 (alpha1D) and T-type Cav3.1 (alpha1G) Ca(2+) channels disrupts heart automaticity. *Sci Rep* 10**,** 18906, doi: 10.1038/s41598-020-76049-7.

Behar, J., Ganesan, A., Zhang, J., and Yaniv, Y. (2016). The Autonomic Nervous System Regulates the Heart Rate through cAMP-PKA Dependent and Independent Coupled-Clock Pacemaker Cell Mechanisms. *Front Physiol* 7**,** 419, doi: 10.3389/fphys.2016.00419.

Bers, D.M. (2006). Cardiac ryanodine receptor phosphorylation: target sites and functional consequences. *Biochem J* 396**,** e1-3, doi: 10.1042/BJ20060377.

Berul, C.I. (2003). Electrophysiological phenotyping in genetically engineered mice. *Physiol Genomics* 13**,** 207-216, doi: 10.1152/physiolgenomics.00183.2002.

Berul, C.I., Aronovitz, M.J., Wang, P.J., and Mendelsohn, M.E. (1996). In vivo cardiac electrophysiology studies in the mouse. *Circulation* 94**,** 2641-2648, doi: 10.1161/01.cir.94.10.2641.

Biel, M., Schneider, A., and Wahl, C. (2002). Cardiac HCN channels: structure, function, and modulation. *Trends Cardiovasc Med* 12**,** 206-212, doi: 10.1016/s1050-1738(02)00162-7.

Biel, M., Wahl-Schott, C., Michalakis, S., and Zong, X. (2009). Hyperpolarization-activated cation channels: from genes to function. *Physiol Rev* 89**,** 847-885, doi: 10.1152/physrev.00029.2008.

Billette, J. (1987). Atrioventricular nodal activation during periodic premature stimulation of the atrium. *Am J Physiol* 252**,** H163-177, doi: 10.1152/ajpheart.1987.252.1.H163.

Bogdanov, K.Y., Maltsev, V.A., Vinogradova, T.M., Lyashkov, A.E., Spurgeon, H.A., Stern, M.D., and Lakatta, E.G. (2006). Membrane potential fluctuations resulting from submembrane Ca2+ releases in rabbit sinoatrial nodal cells impart an exponential phase to the late diastolic depolarization that controls their chronotropic state. *Circ Res* 99**,** 979-987, doi: 10.1161/01.RES.0000247933.66532.0b.

Bogdanov, K.Y., Vinogradova, T.M., and Lakatta, E.G. (2001). Sinoatrial nodal cell ryanodine receptor and Na(+)-Ca(2+) exchanger: molecular partners in pacemaker regulation. *Circ Res* 88**,** 1254-1258, doi: 10.1161/hh1201.092095.

Boyett, M.R. (2009). 'And the beat goes on.' The cardiac conduction system: the wiring system of the heart. *Exp Physiol* 94**,** 1035-1049, doi: 10.1113/expphysiol.2009.046920.

Brown, H.F., Difrancesco, D., and Noble, S.J. (1979). How does adrenaline accelerate the heart? *Nature* 280**,** 235-236, doi: 10.1038/280235a0.

Camelliti, P., Green, C.R., Legrice, I., and Kohl, P. (2004). Fibroblast network in rabbit sinoatrial node: structural and functional identification of homogeneous and heterogeneous cell coupling. *Circ Res* 94**,** 828-835, doi: 10.1161/01.RES.0000122382.19400.14.

Clasen, L., Eickholt, C., Angendohr, S., Jungen, C., Shin, D.I., Donner, B., Furnkranz, A., Kelm, M., Klocker, N., Meyer, C., and Makimoto, H. (2018). A modified approach for programmed electrical

stimulation in mice: Inducibility of ventricular arrhythmias. *PLoS One* 13**,** e0201910, doi: 10.1371/journal.pone.0201910.

Dai, G., Aman, T.K., Dimaio, F., and Zagotta, W.N. (2021). Electromechanical coupling mechanism for activation and inactivation of an HCN channel. *Nat Commun* 12**,** 2802, doi: 10.1038/s41467-021-23062-7.

De Carvalho, A., and De Almeida, D. (1960). Spread of activity through the atrioventricular node. *Circ Res* 8**,** 801-809, doi: 10.1161/01.res.8.4.801.

Difrancesco, D. (1993). Pacemaker mechanisms in cardiac tissue. *Annu Rev Physiol* 55**,** 455-472, doi: 10.1146/annurev.ph.55.030193.002323.

Difrancesco, D., Ferroni, A., Mazzanti, M., and Tromba, C. (1986). Properties of the hyperpolarizing-activated current (if) in cells isolated from the rabbit sino-atrial node. *J Physiol* 377**,** 61-88, doi: 10.1113/jphysiol.1986.sp016177.

Difrancesco, D., and Tortora, P. (1991). Direct activation of cardiac pacemaker channels by intracellular cyclic AMP. *Nature* 351**,** 145-147, doi: 10.1038/351145a0.

Dzhura, I., Wu, Y., Colbran, R.J., Balser, J.R., and Anderson, M.E. (2000). Calmodulin kinase determines calcium-dependent facilitation of L-type calcium channels. *Nat Cell Biol* 2**,** 173-177, doi: 10.1038/35004052.

Efimov, I.R., Nikolski, V.P., Rothenberg, F., Greener, I.D., Li, J., Dobrzynski, H., and Boyett, M. (2004). Structure-function relationship in the AV junction. *Anat Rec A Discov Mol Cell Evol Biol* 280**,** 952-965, doi: 10.1002/ar.a.20108.

Elinder, F., Mannikko, R., Pandey, S., and Larsson, H.P. (2006). Mode shifts in the voltage gating of the mouse and human HCN2 and HCN4 channels. *J Physiol* 575**,** 417-431, doi: 10.1113/jphysiol.2006.110437.

Eschenhagen, T. (2010). Is ryanodine receptor phosphorylation key to the fight or flight response and heart failure? *J Clin Invest* 120**,** 4197-4203, doi: 10.1172/JCI45251.

Fenske, S., Hennis, K., Rotzer, R.D., Brox, V.F., Becirovic, E., Scharr, A., Gruner, C., Ziegler, T., Mehlfeld, V., Brennan, J., Efimov, I.R., Pauza, A.G., Moser, M., Wotjak, C.T., Kupatt, C., Gonner, R., Zhang, R., Zhang, H., Zong, X., Biel, M., and Wahl-Schott, C. (2020). cAMP-dependent regulation of HCN4 controls the tonic entrainment process in sinoatrial node pacemaker cells. *Nat Commun* 11**,** 5555, doi: 10.1038/s41467-020-19304-9.

Fenske, S., Krause, S.C., Hassan, S.I., Becirovic, E., Auer, F., Bernard, R., Kupatt, C., Lange, P., Ziegler, T., Wotjak, C.T., Zhang, H., Hammelmann, V., Paparizos, C., Biel, M., and Wahl-Schott, C.A. (2013). Sick sinus syndrome in HCN1-deficient mice. *Circulation* 128**,** 2585-2594, doi: 10.1161/CIRCULATIONAHA.113.003712.

Fenske, S., Probstle, R., Auer, F., Hassan, S., Marks, V., Pauza, D.H., Biel, M., and Wahl-Schott, C. (2016). Comprehensive multilevel in vivo and in vitro analysis of heart rate fluctuations in mice by ECG telemetry and electrophysiology. *Nat Protoc* 11**,** 61-86, doi: 10.1038/nprot.2015.139.

Gao, Z., Rasmussen, T.P., Li, Y., Kutschke, W., Koval, O.M., Wu, Y., Wu, Y., Hall, D.D., Joiner, M.L., Wu, X.Q., Swaminathan, P.D., Purohit, A., Zimmerman, K., Weiss, R.M., Philipson, K.D., Song, L.S., Hund, T.J., and Anderson, M.E. (2013). Genetic inhibition of Na+-Ca2+ exchanger current disables fight or flight sinoatrial node activity without affecting resting heart rate. *Circ Res* 112**,** 309-317, doi: 10.1161/CIRCRESAHA.111.300193.

Gee, K.R., Brown, K.A., Chen, W.N., Bishop-Stewart, J., Gray, D., and Johnson, I. (2000). Chemical and physiological characterization of fluo-4 Ca(2+)-indicator dyes. *Cell Calcium* 27**,** 97-106, doi: 10.1054/ceca.1999.0095.

Grimm, M., and Brown, J.H. (2010). Beta-adrenergic receptor signaling in the heart: role of CaMKII. *J Mol Cell Cardiol* 48**,** 322-330, doi: 10.1016/j.yjmcc.2009.10.016.

Guinamard, R., Bouvagnet, P., Hof, T., Liu, H., Simard, C., and Salle, L. (2015). TRPM4 in cardiac electrical activity. *Cardiovasc Res* 108**,** 21-30, doi: 10.1093/cvr/cvv213.

Hagiwara, N., Irisawa, H., and Kameyama, M. (1988). Contribution of two types of calcium currents to the pacemaker potentials of rabbit sino-atrial node cells. *J Physiol* 395**,** 233-253, doi: 10.1113/jphysiol.1988.sp016916.

Han, Y., Lyman, K.A., Foote, K.M., and Chetkovich, D.M. (2020). The structure and function of TRIP8b, an auxiliary subunit of hyperpolarization-activated cyclic-nucleotide gated channels. *Channels (Austin)* 14**,** 110-122, doi: 10.1080/19336950.2020.1740501.

Harzheim, D., Pfeiffer, K.H., Fabritz, L., Kremmer, E., Buch, T., Waisman, A., Kirchhof, P., Kaupp, U.B., and Seifert, R. (2008). Cardiac pacemaker function of HCN4 channels in mice is confined to embryonic development and requires cyclic AMP. *EMBO J* 27**,** 692-703, doi: 10.1038/emboj.2008.3.

Hennis, K., Biel, M., Wahl-Schott, C., and Fenske, S. (2021a). Beyond pacemaking: HCN channels in sinoatrial node function. *Prog Biophys Mol Biol* doi: 10.1016/j.pbiomolbio.2021.03.004.

Hennis, K., Rotzer, R.D., Piantoni, C., Biel, M., Wahl-Schott, C., and Fenske, S. (2021b). Speeding Up the Heart? Traditional and New Perspectives on HCN4 Function. *Front Physiol* 12**,** 669029, doi: 10.3389/fphys.2021.669029.

Hennis, K., Rotzer, R.D., Rilling, J., Wu, Y., Thalhammer, S.B., Biel, M., Wahl-Schott, C., and Fenske, S. (2021c). In vivo and ex vivo electrophysiological study of the mouse heart to characterize the cardiac conduction system, including atrial and ventricular vulnerability. *Nature Protocols (accepted)* doi.

Herrmann, S., Layh, B., and Ludwig, A. (2011). Novel insights into the distribution of cardiac HCN channels: an expression study in the mouse heart. *J Mol Cell Cardiol* 51**,** 997-1006, doi: 10.1016/j.yjmcc.2011.09.005.

Herrmann, S., Stieber, J., Stockl, G., Hofmann, F., and Ludwig, A. (2007). HCN4 provides a 'depolarization reserve' and is not required for heart rate acceleration in mice. *EMBO J* 26**,** 4423-4432, doi: 10.1038/sj.emboj.7601868.

Hoesl, E., Stieber, J., Herrmann, S., Feil, S., Tybl, E., Hofmann, F., Feil, R., and Ludwig, A. (2008). Tamoxifen-inducible gene deletion in the cardiac conduction system. *J Mol Cell Cardiol* 45**,** 62-69, doi: 10.1016/j.yjmcc.2008.04.008.

Hof, T., Simard, C., Rouet, R., Salle, L., and Guinamard, R. (2013). Implication of the TRPM4 nonselective cation channel in mammalian sinus rhythm. *Heart Rhythm* 10**,** 1683-1689, doi: 10.1016/j.hrthm.2013.08.014.

Hoffman, B.F., De Carvalho, A.P., and De Mello, W.C. (1958). Transmembrane potentials of single fibres of the atrio-ventricular node. *Nature* 181**,** 66-67, doi: 10.1038/181066a0.

Hulsmans, M., Clauss, S., Xiao, L., Aguirre, A.D., King, K.R., Hanley, A., Hucker, W.J., Wulfers, E.M., Seemann, G., Courties, G., Iwamoto, Y., Sun, Y., Savol, A.J., Sager, H.B., Lavine, K.J., Fishbein, G.A., Capen, D.E., Da Silva, N., Miquerol, L., Wakimoto, H., Seidman, C.E., Seidman, J.G., Sadreyev, R.I., Naxerova, K., Mitchell, R.N., Brown, D., Libby, P., Weissleder, R., Swirski, F.K., Kohl, P., Vinegoni, C., Milan, D.J., Ellinor, P.T., and Nahrendorf, M. (2017). Macrophages Facilitate Electrical Conduction in the Heart. *Cell* 169**,** 510-522 e520, doi: 10.1016/j.cell.2017.03.050.

Jalife, J. (1983). The sucrose gap preparation as a model of AV nodal transmission: are dual pathways necessary for reciprocation and AV nodal "echoes"? *Pacing Clin Electrophysiol* 6**,** 1106-1122, doi: 10.1111/j.1540-8159.1983.tb04449.x.

Jalife, J. (1984). Mutual entrainment and electrical coupling as mechanisms for synchronous firing of rabbit sino-atrial pace-maker cells. *J Physiol* 356**,** 221-243, doi: 10.1113/jphysiol.1984.sp015461.

Kozasa, Y., Nakashima, N., Ito, M., Ishikawa, T., Kimoto, H., Ushijima, K., Makita, N., and Takano, M. (2018). HCN4 pacemaker channels attenuate the parasympathetic response and stabilize the spontaneous firing of the sinoatrial node. *J Physiol* 596**,** 809-825, doi: 10.1113/JP275303.

Kugler, J.D., Gillette, P.C., Mullins, C.E., and Mcnamara, D.G. (1979). Sinoatrial conduction in children: an index of sinoatrial node function. *Circulation* 59**,** 1266-1276, doi: 10.1161/01.cir.59.6.1266.

Labarre, A., Strauss, H.C., Scheinman, M.M., Evans, G.T., Bashore, T., Tiedeman, J.S., and Wallace, A.G. (1979). Electrophysiologic effects of disopyramide phosphate on sinus node function in patients with sinus node dysfunction. *Circulation* 59**,** 226-235, doi: 10.1161/01.cir.59.2.226.

Lakatta, E.G., Maltsev, V.A., and Vinogradova, T.M. (2010). A coupled SYSTEM of intracellular Ca2+ clocks and surface membrane voltage clocks controls the timekeeping mechanism of the heart's pacemaker. *Circ Res* 106**,** 659-673, doi: 10.1161/CIRCRESAHA.109.206078.

Lei, M., Brown, H.F., and Terrar, D.A. (2000). Modulation of delayed rectifier potassium current, iK, by isoprenaline in rabbit isolated pacemaker cells. *Exp Physiol* 85**,** 27-35, doi.

Li, N., Csepe, T.A., Hansen, B.J., Dobrzynski, H., Higgins, R.S., Kilic, A., Mohler, P.J., Janssen, P.M., Rosen, M.R., Biesiadecki, B.J., and Fedorov, V.V. (2015). Molecular Mapping of Sinoatrial Node HCN Channel Expression in the Human Heart. *Circ Arrhythm Electrophysiol* 8**,** 1219-1227, doi: 10.1161/CIRCEP.115.003070.

Li, N., and Wehrens, X.H. (2010). Programmed electrical stimulation in mice. *J Vis Exp* doi: 10.3791/1730.

Li, Y., Sirenko, S., Riordon, D.R., Yang, D., Spurgeon, H., Lakatta, E.G., and Vinogradova, T.M. (2016). CaMKII-dependent phosphorylation regulates basal cardiac pacemaker function via modulation of local Ca2+ releases. *Am J Physiol Heart Circ Physiol* 311**,** H532-544, doi: 10.1152/ajpheart.00765.2015.

Li, Y., Wang, F., Zhang, X., Qi, Z., Tang, M., Szeto, C., Li, Y., Zhang, H., and Chen, X. (2012). beta-Adrenergic stimulation increases Cav3.1 activity in cardiac myocytes through protein kinase A. *PLoS One* 7**,** e39965, doi: 10.1371/journal.pone.0039965.

Liao, Z., Lockhead, D., Larson, E.D., and Proenza, C. (2010). Phosphorylation and modulation of hyperpolarization-activated HCN4 channels by protein kinase A in the mouse sinoatrial node. *J Gen Physiol* 136**,** 247-258, doi: 10.1085/jgp.201010488.

Liu, J., Dobrzynski, H., Yanni, J., Boyett, M.R., and Lei, M. (2007). Organisation of the mouse sinoatrial node: structure and expression of HCN channels. *Cardiovasc Res* 73**,** 729-738, doi: 10.1016/j.cardiores.2006.11.016.

Ludwig, A., Zong, X., Jeglitsch, M., Hofmann, F., and Biel, M. (1998). A family of hyperpolarization-activated mammalian cation channels. *Nature* 393**,** 587-591, doi: 10.1038/31255.

Macdonald, E.A., Rose, R.A., and Quinn, T.A. (2020). Neurohumoral Control of Sinoatrial Node Activity and Heart Rate: Insight From Experimental Models and Findings From Humans. *Front Physiol* 11**,** 170, doi: 10.3389/fphys.2020.00170.

Maltsev, A.V., Yaniv, Y., Stern, M.D., Lakatta, E.G., and Maltsev, V.A. (2013). RyR-NCX-SERCA local cross-talk ensures pacemaker cell function at rest and during the fight-or-flight reflex. *Circ Res* 113**,** e94-e100, doi: 10.1161/CIRCRESAHA.113.302465.

Maltsev, V.A., and Lakatta, E.G. (2009). Synergism of coupled subsarcolemmal Ca2+ clocks and sarcolemmal voltage clocks confers robust and flexible pacemaker function in a novel pacemaker cell model. *Am J Physiol Heart Circ Physiol* 296**,** H594-615, doi: 10.1152/ajpheart.01118.2008.

Mangoni, M.E., Couette, B., Bourinet, E., Platzer, J., Reimer, D., Striessnig, J., and Nargeot, J. (2003). Functional role of L-type Cav1.3 Ca2+ channels in cardiac pacemaker activity. *Proc Natl Acad Sci U S A* 100**,** 5543-5548, doi: 10.1073/pnas.0935295100.

Mangoni, M.E., and Nargeot, J. (2008). Genesis and regulation of the heart automaticity. *Physiol Rev* 88**,** 919-982, doi: 10.1152/physrev.00018.2007.

Mannikko, R., Pandey, S., Larsson, H.P., and Elinder, F. (2005). Hysteresis in the voltage dependence of HCN channels: conversion between two modes affects pacemaker properties. *J Gen Physiol* 125**,** 305-326, doi: 10.1085/jgp.200409130.

Marionneau, C., Couette, B., Liu, J., Li, H., Mangoni, M.E., Nargeot, J., Lei, M., Escande, D., and Demolombe, S. (2005). Specific pattern of ionic channel gene expression associated with pacemaker activity in the mouse heart. *J Physiol* 562**,** 223-234, doi: 10.1113/jphysiol.2004.074047.

Markram, H., Toledo-Rodriguez, M., Wang, Y., Gupta, A., Silberberg, G., and Wu, C. (2004). Interneurons of the neocortical inhibitory system. *Nat Rev Neurosci* 5**,** 793-807, doi: 10.1038/nrn1519.

Mesirca, P., Alig, J., Torrente, A.G., Muller, J.C., Marger, L., Rollin, A., Marquilly, C., Vincent, A., Dubel, S., Bidaud, I., Fernandez, A., Seniuk, A., Engeland, B., Singh, J., Miquerol, L., Ehmke, H.,

Eschenhagen, T., Nargeot, J., Wickman, K., Isbrandt, D., and Mangoni, M.E. (2014). Cardiac arrhythmia induced by genetic silencing of 'funny' (f) channels is rescued by GIRK4 inactivation. *Nat Commun* 5**,** 4664, doi: 10.1038/ncomms5664.

Mesirca, P., Fedorov, V.V., Hund, T.J., Torrente, A.G., Bidaud, I., Mohler, P.J., and Mangoni, M.E. (2021). Pharmacologic Approach to Sinoatrial Node Dysfunction. *Annu Rev Pharmacol Toxicol* 61**,** 757-778, doi: 10.1146/annurev-pharmtox-031120-115815.

Narayanan, N., and Xu, A. (1997). Phosphorylation and regulation of the Ca(2+)-pumping ATPase in cardiac sarcoplasmic reticulum by calcium/calmodulin-dependent protein kinase. *Basic Res Cardiol* 92 Suppl 1**,** 25-35, doi: 10.1007/BF00794065.

Narula, O.S., Samet, P., and Javier, R.P. (1972). Significance of the sinus-node recovery time. *Circulation* 45**,** 140-158, doi: 10.1161/01.cir.45.1.140.

Nof, E., Antzelevitch, C., and Glikson, M. (2010). The Contribution of HCN4 to normal sinus node function in humans and animal models. *Pacing Clin Electrophysiol* 33**,** 100-106, doi: 10.1111/j.1540-8159.2009.02563.x.

Pauza, D.H., Rysevaite, K., Inokaitis, H., Jokubauskas, M., Pauza, A.G., Brack, K.E., and Pauziene, N. (2014). Innervation of sinoatrial nodal cardiomyocytes in mouse. A combined approach using immunofluorescent and electron microscopy. *J Mol Cell Cardiol* 75**,** 188-197, doi: 10.1016/j.yjmcc.2014.07.016.

Peters, C.H., Liu, P.W., Morotti, S., Gantz, S.C., Grandi, E., Bean, B.P., and Proenza, C. (2021). Bidirectional flow of the funny current (If) during the pacemaking cycle in murine sinoatrial node myocytes. *Proc Natl Acad Sci U S A* 118doi: 10.1073/pnas.2104668118.

Porro, A., Saponaro, A., Gasparri, F., Bauer, D., Gross, C., Pisoni, M., Abbandonato, G., Hamacher, K., Santoro, B., Thiel, G., and Moroni, A. (2019). The HCN domain couples voltage gating and cAMP response in hyperpolarization-activated cyclic nucleotide-gated channels. *Elife* 8doi: 10.7554/eLife.49672.

Reiffel, J.A., Bigger, J.T., Jr., and Konstam, M.A. (1974). The relationship between sinoatrial conduction time and sinus cycle length during spontaneous sinus arrhythmia in adults. *Circulation* 50**,** 924-934, doi: 10.1161/01.cir.50.5.924.

Rigg, L., Heath, B.M., Cui, Y., and Terrar, D.A. (2000). Localisation and functional significance of ryanodine receptors during beta-adrenoceptor stimulation in the guinea-pig sino-atrial node. *Cardiovasc Res* 48**,** 254-264, doi: 10.1016/s0008-6363(00)00153-x.

Rosenblueth, A. (1955). [The operator of the atrioventricular node]. *Arch Inst Cardiol Mex* 25**,** 171-193, doi.

Rosenblueth, A. (1958). Functional refractory period of cardiac tissues. *Am J Physiol* 194**,** 171-183, doi: 10.1152/ajplegacy.1958.194.1.171.

Sadeh, S., and Clopath, C. (2021). Inhibitory stabilization and cortical computation. *Nat Rev Neurosci* 22**,** 21-37, doi: 10.1038/s41583-020-00390-z.

Saponaro, A., Bauer, D., Giese, M.H., Swuec, P., Porro, A., Gasparri, F., Sharifzadeh, A.S., Chaves-Sanjuan, A., Alberio, L., Parisi, G., Cerutti, G., Clarke, O.B., Hamacher, K., Colecraft, H.M., Mancia, F., Hendrickson, W.A., Siegelbaum, S.A., Difrancesco, D., Bolognesi, M., Thiel, G., Santoro, B., and Moroni, A. (2021). Gating movements and ion permeation in HCN4 pacemaker channels. *Mol Cell* 81**,** 2929-2943 e2926, doi: 10.1016/j.molcel.2021.05.033.

Saponaro, A., Cantini, F., Porro, A., Bucchi, A., Difrancesco, D., Maione, V., Donadoni, C., Introini, B., Mesirca, P., Mangoni, M.E., Thiel, G., Banci, L., Santoro, B., and Moroni, A. (2018). A synthetic peptide that prevents cAMP regulation in mammalian hyperpolarization-activated cyclic nucleotide-gated (HCN) channels. *Elife* 7doi: 10.7554/eLife.35753.

Scharr, A. (2011). *Ein genetischer Ansatz zur Analyse der cAMP-abhängigen Modulation des Schrittmacherkanals HCN4.*

Schulze-Bahr, E., Neu, A., Friederich, P., Kaupp, U.B., Breithardt, G., Pongs, O., and Isbrandt, D. (2003). Pacemaker channel dysfunction in a patient with sinus node disease. *J Clin Invest* 111**,** 1537-1545, doi: 10.1172/JCI16387.

Shan, J., Kushnir, A., Betzenhauser, M.J., Reiken, S., Li, J., Lehnart, S.E., Lindegger, N., Mongillo, M., Mohler, P.J., and Marks, A.R. (2010). Phosphorylation of the ryanodine receptor mediates the cardiac fight or flight response in mice. *J Clin Invest* 120**,** 4388-4398, doi: 10.1172/JCI32726.

Simson, M.B., Spear, J., and Moore, E.N. (1979). The relationship between atrioventricular nodal refractoriness and the functional refractory period in the dog. *Circ Res* 44**,** 121-126, doi: 10.1161/01.res.44.1.121.

Stieber, J., Herrmann, S., Feil, S., Loster, J., Feil, R., Biel, M., Hofmann, F., and Ludwig, A. (2003). The hyperpolarization-activated channel HCN4 is required for the generation of pacemaker action potentials in the embryonic heart. *Proc Natl Acad Sci U S A* 100**,** 15235-15240, doi: 10.1073/pnas.2434235100.

Strauss, H.C., Saroff, A.L., Bigger, J.T., Jr., and Giardina, E.G. (1973). Premature atrial stimulation as a key to the understanding of sinoatrial conduction in man. Presentation of data and critical review of the literature. *Circulation* 47**,** 86-93, doi: 10.1161/01.cir.47.1.86.

Swaminathan, P.D., Purohit, A., Soni, S., Voigt, N., Singh, M.V., Glukhov, A.V., Gao, Z., He, B.J., Luczak, E.D., Joiner, M.L., Kutschke, W., Yang, J., Donahue, J.K., Weiss, R.M., Grumbach, I.M., Ogawa, M., Chen, P.S., Efimov, I., Dobrev, D., Mohler, P.J., Hund, T.J., and Anderson, M.E. (2011). Oxidized CaMKII causes cardiac sinus node dysfunction in mice. *J Clin Invest* 121**,** 3277-3288, doi: 10.1172/JCI57833.

Tsutsui, K., Monfredi, O.J., Sirenko-Tagirova, S.G., Maltseva, L.A., Bychkov, R., Kim, M.S., Ziman, B.D., Tarasov, K.V., Tarasova, Y.S., Zhang, J., Wang, M., Maltsev, A.V., Brennan, J.A., Efimov, I.R., Stern, M.D., Maltsev, V.A., and Lakatta, E.G. (2018). A coupled-clock system drives the automaticity of human sinoatrial nodal pacemaker cells. *Sci Signal* 11doi: 10.1126/scisignal.aap7608.

Van Der Heyden, M.A., Wijnhoven, T.J., and Opthof, T. (2005). Molecular aspects of adrenergic modulation of cardiac L-type Ca2+ channels. *Cardiovasc Res* 65**,** 28-39, doi: 10.1016/j.cardiores.2004.09.028.

Verheijck, E.E., Wilders, R., and Bouman, L.N. (2002). Atrio-sinus interaction demonstrated by blockade of the rapid delayed rectifier current. *Circulation* 105**,** 880-885, doi: 10.1161/hc0702.104128.

Verkerk, A.O., and Wilders, R. (2014). Pacemaker activity of the human sinoatrial node: effects of HCN4 mutations on the hyperpolarization-activated current. *Europace* 16**,** 384-395, doi: 10.1093/europace/eut348.

Verkerk, A.O., and Wilders, R. (2015). Pacemaker activity of the human sinoatrial node: an update on the effects of mutations in HCN4 on the hyperpolarization-activated current. *Int J Mol Sci* 16**,** 3071-3094, doi: 10.3390/ijms16023071.

Vinogradova, T.M., Bogdanov, K.Y., and Lakatta, E.G. (2002). beta-Adrenergic stimulation modulates ryanodine receptor Ca(2+) release during diastolic depolarization to accelerate pacemaker activity in rabbit sinoatrial nodal cells. *Circ Res* 90**,** 73-79, doi: 10.1161/hh0102.102271.

Vinogradova, T.M., Brochet, D.X., Sirenko, S., Li, Y., Spurgeon, H., and Lakatta, E.G. (2010). Sarcoplasmic reticulum Ca2+ pumping kinetics regulates timing of local Ca2+ releases and spontaneous beating rate of rabbit sinoatrial node pacemaker cells. *Circ Res* 107**,** 767-775, doi: 10.1161/CIRCRESAHA.110.220517.

Vinogradova, T.M., Lyashkov, A.E., Zhu, W., Ruknudin, A.M., Sirenko, S., Yang, D., Deo, S., Barlow, M., Johnson, S., Caffrey, J.L., Zhou, Y.Y., Xiao, R.P., Cheng, H., Stern, M.D., Maltsev, V.A., and Lakatta, E.G. (2006). High basal protein kinase A-dependent phosphorylation drives rhythmic internal Ca2+ store oscillations and spontaneous beating of cardiac pacemaker cells. *Circ Res* 98**,** 505-514, doi: 10.1161/01.RES.0000204575.94040.d1.

Vinogradova, T.M., Tagirova Sirenko, S., and Lakatta, E.G. (2018). Unique Ca(2+)-Cycling Protein Abundance and Regulation Sustains Local Ca(2+) Releases and Spontaneous Firing of Rabbit Sinoatrial Node Cells. *Int J Mol Sci* 19doi: 10.3390/ijms19082173.

Vinogradova, T.M., Zhou, Y.Y., Bogdanov, K.Y., Yang, D., Kuschel, M., Cheng, H., and Xiao, R.P. (2000). Sinoatrial node pacemaker activity requires Ca(2+)/calmodulin-dependent protein kinase II activation. *Circ Res* 87**,** 760-767, doi: 10.1161/01.res.87.9.760.

Vinogradova, T.M., Zhou, Y.Y., Maltsev, V., Lyashkov, A., Stern, M., and Lakatta, E.G. (2004). Rhythmic ryanodine receptor Ca2+ releases during diastolic depolarization of sinoatrial pacemaker cells do not require membrane depolarization. *Circ Res* 94**,** 802-809, doi: 10.1161/01.RES.0000122045.55331.0F.

Wainger, B.J., Degennaro, M., Santoro, B., Siegelbaum, S.A., and Tibbs, G.R. (2001). Molecular mechanism of cAMP modulation of HCN pacemaker channels. *Nature* 411**,** 805-810, doi: 10.1038/35081088.

Westphal, C., Spallek, B., Konkel, A., Marko, L., Qadri, F., Degraff, L.M., Schubert, C., Bradbury, J.A., Regitz-Zagrosek, V., Falck, J.R., Zeldin, D.C., Muller, D.N., Schunck, W.H., and Fischer, R. (2013). CYP2J2 overexpression protects against arrhythmia susceptibility in cardiac hypertrophy. *PLoS One* 8**,** e73490, doi: 10.1371/journal.pone.0073490.

Wu, Y., and Anderson, M.E. (2014). CaMKII in sinoatrial node physiology and dysfunction. *Front Pharmacol* 5**,** 48, doi: 10.3389/fphar.2014.00048.

Wu, Y., Gao, Z., Chen, B., Koval, O.M., Singh, M.V., Guan, X., Hund, T.J., Kutschke, W., Sarma, S., Grumbach, I.M., Wehrens, X.H., Mohler, P.J., Song, L.S., and Anderson, M.E. (2009). Calmodulin kinase II is required for fight or flight sinoatrial node physiology. *Proc Natl Acad Sci U S A* 106**,** 5972-5977, doi: 10.1073/pnas.0806422106.

Xiao, Y.F., Chandler, N., Dobrzynski, H., Richardson, E.S., Tenbroek, E.M., Wilhelm, J.J., Sharma, V., Varghese, A., Boyett, M.R., Iaizzo, P.A., and Sigg, D.C. (2010). Hysteresis in human HCN4 channels: a crucial feature potentially affecting sinoatrial node pacemaking. *Sheng Li Xue Bao* 62**,** 1-13, doi.

Zagotta, W.N., Olivier, N.B., Black, K.D., Young, E.C., Olson, R., and Gouaux, E. (2003). Structural basis for modulation and agonist specificity of HCN pacemaker channels. *Nature* 425**,** 200-205, doi: 10.1038/nature01922.

Zhao, X., Bucchi, A., Oren, R.V., Kryukova, Y., Dun, W., Clancy, C.E., and Robinson, R.B. (2009). In vitro characterization of HCN channel kinetics and frequency dependence in myocytes predicts biological pacemaker functionality. *J Physiol* 587**,** 1513-1525, doi: 10.1113/jphysiol.2008.163444.

Zhou, L., and Siegelbaum, S.A. (2007). Gating of HCN channels by cyclic nucleotides: residue contacts that underlie ligand binding, selectivity, and efficacy. *Structure* 15**,** 655-670, doi: 10.1016/j.str.2007.04.012.

Zhou, Z., and Lipsius, S.L. (1993). Na(+)-Ca2+ exchange current in latent pacemaker cells isolated from cat right atrium. *J Physiol* 466**,** 263-285, doi.

8. Appendix

8.1 List of abbreviations

A	Atrial signal
AC	Adenylyl cyclase
ACh	Acetylcholine
AERP	Atrial effective refractory period
AM	Acetoxymethyl ester
AN	Atrionodal
ANOVA	Analysis of variance
ANS	Autonomic nervous system
ARP	Absolute refractory period
ATP	Adenosine triphosphate
ATR	Atrium
AV	Atrioventricular
AVERP	Effective refractory period of the AV conduction system
AVFRP	Functional refractory period of the AV conduction system
AVN	Atrioventricular node
AVRRP	Relative refractory period of the AV conduction system
BSA	Bovine serum albumin
CaMKII	Ca^{2+}/calmodulin-dependent kinase II
cAMP	Cyclic adenosine monophosphate
CCh	Carbamoylcholine (carbachol)
CCS	Cardiac conduction system
CDR	cAMP-dependent regulation
CNBD	Cyclic nucleotide-binding domain
cSNRT	Rate-corrected sinus node recovery time
DMSO	Dimethyl sulfoxide
DNA	Deoxyribonucleic acid
ECG	Electrocardiogram
EPS	Electrophysiological study
ERP	Effective refractory period
FRET	Förster resonance energy transfer
GIRK	G protein-coupled inwardly-rectifying potassium channel
GLM	General linear model
H	His bundle signal
HCN	Hyperpolarization-activated cyclic nucleotide-gated cation channel
HCN4FEA	$Hcn4^{tm3(Y527F;R669E;T670A)Biel}$
His	Bundle of His
HR	Heart rate
HRAd	Distal high right atrium
HRAp	Proximal high right atrium
HyD	Hybrid detector
IAVD	Isorhythmic atrioventricular dissociation
ISO	Isoproterenol
JER	Junctional escape rhythm

KB	Kraftbrühe
LA	Left atrium
LBB	Left bundle branch
LCR	Local calcium release
LV	Left ventricle
MDP	Maximum diastolic potential
N	Nodal
NCX	Sodium-calcium exchanger
NE	Norepinephrine
NH	Nodal-His
NSVT	Nonsustained ventricular tachycardia
OPSL	Optically pumped semiconductor laser
PBS	Phosphate-buffered saline
PCL	Pacing cycle length
PCR	Polymerase chain reaction
PF	Purkinje fibres
PKA	Protein kinase A
PLB	Phospholamban
PLL	Poly-L-lysine
PNZ	Perinodal zone
PSNS	Parasympathetic nervous system
RA	Right atrium
RBB	Right bundle branch
RRP	Relative refractory period
RV	Right ventricle
RVd	Distal right ventricle
RVp	Proximal right ventricle
RyR	Ryanodine receptor
S	Stimulus
SACT	Sinoatrial conduction time
SACT NM	Sinoatrial conduction time Narula method
SACT SM	Sinoatrial conduction time Strauss method
SAN	Sinoatrial node
SCL	Sinus cycle length
SEM	Standard error of the mean
SERCA	Sarco-/endoplasmic reticulum Ca^{2+} ATPase
SNRT	Sinus node recovery time
SNS	Sympathetic nervous system
SR	Sarcoplasmic reticulum
SSD	Slow diastolic depolarization
TRPM4	Transient receptor potential melastatin 4 channel
V	Ventricular signal
$V_{0.5}$	Half-maximal activation voltage
VERP	Ventricular effective refractory period
V_m	Membrane voltage
WBP	Wenckebach point
WT	Wild-type

8.2 List of publications

Hennis K, Roetzer R, Rilling J, Wu Y, Thalhammer S, Biel M, Wahl-Schott C, Fenske S: In vivo and ex vivo electrophysiological study of the mouse heart to characterize the cardiac conduction system, including atrial and ventricular vulnerability. ***Nature Protocols*** (*accepted*)

Esfandyari D, Idrissou B, **Hennis K**, Avramopoulos P, Dueck A, El-Battrawy I, Grüter L, Meier M, Näger A, Ramanujam D, Dorn T, Meitinger T, Hagl C, Milting H, Borggrefe M, Fenske S, Biel M, Dendorfer A, Sassi Y, Moretti A, Engelhardt S: MicroRNA-365 regulates human cardiac action potential duration***.*** ***Nature Communications*** (*accepted*)

Hennis K, Roetzer R, Piantoni C, Biel M, Wahl-Schott C, Fenske S: Speeding up the heart? Traditional and new perspectives on HCN4 function. ***Frontiers in Physiology*** (2021)

Hennis K, Biel M, Wahl-Schott C, Fenske S: Beyond pacemaking: HCN channels in sinoatrial node function. ***Progress in Biophysics and Molecular Biology*** (2021)

Roetzer R, Brox V, **Hennis K**, Thalhammer S, Biel M, Wahl-Schott C, Fenske S: Implantation of Combined Telemetric ECG and Blood Pressure Transmitters to Determine Spontaneous Baroreflex Sensitivity in Conscious Mice. ***Journal of Visualized Experiments*** (2021)

Fenske S, **Hennis K***, Roetzer R*, Brox V*, Becirovic E, Scharr A, Gruner C, Ziegler T, Mehlfeld V, Brennan J, Efimov I, Pauza A, Moser M, Wotjak C, Kupatt C, Goenner R, Zhang R, Zhang H, Zong X, Biel M, Wahl-Schott C: cAMP-dependent regulation of HCN4 controls the tonic entrainment process in sinoatrial node pacemaker cells. ***Nature Communications*** (2020), **equal contribution*

Vedovato N, Rorsman O, **Hennis K**, Ashcroft FM, Proks P: Role of the C-terminus of SUR in the differential regulation of β-cell and cardiac K_{ATP} channels by MgADP and metabolism. ***The Journal of Physiology*** (2018)

Vedovato N, Proks P, Rorsman O, **Hennis K**, Ashcroft FM: Differential Metabolic and Nucleotide Sensitivity of Beta-Cell and Cardiac K_{ATP} Channels. ***Biophysical Journal*** (2018), *Conference Abstract*

8.3 Acknowledgements

Zuallererst möchte ich mich ganz herzlich bei Herrn Prof. Dr. Martin Biel für die Aufnahme in den Arbeitskreis, die produktive Zusammenarbeit bei den Publikationen und die schönen Feiern bedanken.

Ein großer Dank gilt außerdem Herrn Prof. Dr. Christian Wahl-Schott für die sehr gute Betreuung, auch über die Distanz nach Hannover hinweg. Christian, es hat viel Spaß gemacht mit dir zusammen dem Nonfiring-Modus auf den Grund zu gehen und im Anschluss auf die gemeinsamen Erfolge anzustoßen.

Genauso herzlich möchte ich mich bei Frau PD Dr. Stefanie Fenske bedanken. Vielen Dank, liebe Steffi, dass du mich schon früh als HiWi mit ins Boot geholt hast. Für die tagtägliche Betreuung im Labor und die gemeinsame erfolgreiche Zeit bin ich dir sehr dankbar.

Ein besonderer Dank gilt auch meinen MitstreiterInnen im Cardio-Team: René, bei dir möchte ich mich ganz besonders bedanken für deine große Hilfsbereitschaft und uneingeschränkte Kollegialität vom ersten Tag an. Verena und Julia, vielen Dank für die nette und lustige Zusammenarbeit und das Durchhaltevermögen am Konfokal und im Studentenlabor.

Außerdem bedanke ich mich sehr herzlich bei allen anderen aktuellen und ehemaligen ArbeitskollegInnen. Danke für die schöne gemeinsame Zeit im Labor, die gegenseitige Unterstützung und das positive Arbeitsklima. Sabrina und Jacqueline, danke für die vielen lustigen Momente, die witzigen Selfies und die Kurzmeetings an der Kaffeemaschine. Ella, vielen Dank für die Grundkurse MTB und RR und die vielen schönen Ausfahrten. Klara und Marc, danke für die lustigen Abende und die kreativen Einlagen. Und auch bei allen nicht namentlich genannten KollegInnen, die mich während der Promotion unterstützt haben, möchte ich mich ganz herzlich bedanken.

Zu guter Letzt möchte ich mich von ganzem Herzen bei meiner Familie und meiner wundervollen Freundin Lena bedanken. Vielen Dank, dass ihr mich immer ertragen, unterstützt und motiviert habt und ich mich immer auf euch verlassen kann.